Aerodynamics of Low Reynolds Number Rigid Flapping Wing Under Hover and Freestream Conditions

by

Patrick Clark Trizila

A dissertation submitted in partial fulfillment
of the requirements for the degree of
Doctor of Philosophy
(Aerospace Engineering)
in The University of Michigan
2011

Doctoral Committee:

Professor Wei Shyy, Chair
Professor Carlos E. Cesnik
Professor Peretz P. Friedmann
Associate Professor Luis P. Bernal
Assistant Professor Samantha H. Daly
Assistant Professor Anouck R. Girard

Dedication

To my family and friends

Acknowledgements

The work supported here has been supported in part by the Air Force Office of Scientific Research's Multidisciplinary University Research Initiative (MURI) grant and by the Michigan/AFRL (Air Force Research Laboratory)/Boeing Collaborative Center in Aeronautical Sciences.

I would like to thank my advisor Prof. Wei Shyy for his patience and guidance and for the atmosphere which he fostered within the group. The open discussion between members on a daily basis, perhaps hourly basis, was infinitely helpful in problem shooting, expanding horizons, and just getting a look from another perspective.

I would like to thank my committee Dr. Bernal, Dr. Cesnik, Dr. Daly, Dr. Friedmann, and Dr. Girard for their role in helping finalize the last step of this journey.

I would like to thank my group members and office mates for the rich interactions on a daily basis. This work was not the contribution of an individual in isolation, but instead greatly benefitted from the, sometimes quite lively, discussions. I would like to thank Chang-kwon Kang and Dr. Hikaru Aono for the close collaborations and constant dynamic feedback that allowed this work to

happen. I would like to thank Dr. Emre Sozer, Dr. Xiangchun Zhang, Dr. Dragos Viieru, Dr. Eric Gustafson, Dr. Amor Menezes, Dr. Erin Farbar, Dr. Nick Bisek, Dr. Chien-Chou Tseng, (soon to be Dr.) Young Chang Cho for the constant barrage of material which always resulted in new fangled knowledge.

I would like to thank the professors and teachers from my earliest days through graduate school. I find myself fortunate to have been able to have been in the right place at the right time to have had such devoted and approachable mentors. I look at where I am today and my previous incarnations are nowhere near as capable in no small part due to the expectations and efforts put forth by these fantastic individuals. I wish I could name everyone but I feel accidentally leaving one out would be an injustice and I will instead thank you personally when we next meet.

I would like to thank Dr. Jeff Wright and Dr. ST Thakur of Streamline Numerics for help with quite possibly the most unintentionally obfuscated CFD code in Loci-STREAM. I had a bad habit of breaking pieces of the code and do not blame you if you do not answer when you see me calling.

I would like to thank AFRL for the invaluable experience of being able to work so closely with the research labs for three consecutive summers and take advantage of their expertise and experience. I would like to thank Dr. Visbal for the enlightening discussions pertaining to higher order numerical methods and their applications to the flapping wing research area. I would also like to thank the

regular conversations with Dr. Don Rizzetta, Dr. Scott Sherer, Dr. Jon Poggie regarding the methodology and applications during my stay.

I would like to thank Dr. Tushar, Dr. Felipe Viana, and Dr. Haftka for their instruction and patience while developing my understanding of surrogate models and how to make use of them.

I would like to thank the support staff in the department for which they perhaps get too little recognition in keeping the wheels turning of this great department. Particularly I would like to thank Denise Phelps, Lisa Szuma, Dave McLean, and Brock Palen for their part in making this degree happen.

Last but not least I would like to thank my family and friends. I have perhaps been a bit scarce the last few years, but will be redoubling my efforts to compensate shortly. Thank you for your continued reassurances and support.

Table of Contents

List of Figures

List of Tables

List of Abbreviations

AoA- angle of attack

AR- aspect ratio

CFD- computational fluid dynamics

k- reduced frequency

LEV- leading edge vortex

MAV- micro air vehicle

NS- Navier-Stokes

PIV- particle image velocimetry

PRS- polynomial response surface

RBNN- radial basis neural network

Re- Reynolds number

SVR- support vector regression

WAS- weighted average surrogate

Abstract

Micro-air-vehicles (MAVs) are constrained by spatial dimensions less than 15cm. Equipped with a camera or sensor, these vehicles could perform surveillance and reconnaissance with low probability of detection, or environmental and bio-chemical sensing at remote or otherwise hazardous locations. Its size makes the MAV easily transported and deployed as well as inexpensive and more expendable than alternatives, e.g. an airplane, a satellite, or a human.

The ability to hover for an MAV is highly desirable in these contexts. The approach taken in this thesis was to numerically simulate the aerodynamics about flapping wings while controlling the kinematic motions and environmental conditions. Two complementary sets of tools were used in the investigations. i) Navier-Stokes solvers were used to obtain detailed fluid physics information, instantaneous force data, and to train the surrogate models. ii) The surrogate models were used to estimate the time-averaged lift and power required over a flapping cycle while also providing information on the sensitivity of the kinematic variables, to identify trends in lift and power required as a function of the kinematic variables, and to construct a Pareto front showing the trade-offs between the competing objectives.

The roles of the unsteady mechanisms are discussed as well as their influence on the forces felt. Findings include i) the competing influences introduced by tip vortices, and it was seen that they could increase lift compared to their analogous 2D cases, counter to classical steady state theory. ii) The highest time averaged lift values were found during kinematics with high angles of attack during advanced rotation as they promoted LEV generation and subsequently took advantage of them during wake capture. iii) Kinematics with synchronized rotation and low angles of attack had similar 2D and low-aspect-ratio force histories. iv) Modest environmental perturbations were shown to increase the instantaneous 2D forces up to 200%, and though the 3D simulations were less sensitive some felt an increase of 50%. v) The surrogate models proved useful in analysis by identifying local/global sensitivities and trends of the kinematic variables as well as zeroing in on regions for further examination. The kinematics yielding highest lift, lowest power, or where 3D effects became most influential were quickly identifiable.

Chapter 1 Introduction

Micro Air Vehicles (MAVs) have the potential to revolutionize our sensing and information gathering capabilities in areas such as environmental monitoring and homeland security. Numerous aspects relating to potential vehicle concepts, including fixed wing, rotary wing, and flapping wing, have been addressed [see summaries by Shyy *et al.* 2010, Platzer *et al.* 2008, Shyy *et al.* 2008a, Ansari *et al.* 2006, Wang 2005, Dalton 2006, Pines and Bohorquez 2006, Ho *et al.* 2003, Mueller and DeLaurier 2003, Rozhdestvensky and Ryzhov 2003, Norberg 2002, Ellington 1999, Shyy *et al* 1999, Spedding and Lissaman 1998]. As the size of a vehicle becomes smaller than a few centimeters, fixed wing designs encounter fundamental challenges in lift generation and flight control. There are merits and challenges associated with rotary and flapping wing designs. Fundamentally, due to the Reynolds number effect, the aerodynamic characteristics such as the lift, drag and thrust of a flight vehicle change considerably between MAVs and conventional manned air vehicles. And, since MAVs are light weight and fly at low speeds, they are sensitive to wind gusts. Because of the common characteristics shared by MAVs and biological flyers, the aerospace and biological science communities are now actively communicating and collaborating. Much can be shared between researchers with different training and

background including biological insight, mathematical models, physical interpretation, experimental techniques, and design concepts.

MAVs are defined by having a maximal dimension of 15 cm or less and a flight speed of 10 m/s, and are interests for both military and civilian applications. Equipped with a video camera or a sensor, these vehicles can perform surveillance and reconnaissance, and environmental and bio-chemical sensing at remote or otherwise hazardous locations. In addition, from the scaling laws [Shyy *et al.* 2008a], a MAV's payload is very limited; sensors, batteries, communications equipment, and means of sustained propulsion will have to compete for precious cargo space only in as much as that they will directly help defined mission statements. Research regarding MAVs is growing as there are still many open challenges in theory and in practice. Tables 1-3 attempt to characterize select references in an easily readable and more palatable form while favoring conciseness over completeness or comprehensiveness.

Overviews in the Literature	Title
Shyy *et al.* (1999)	Flapping and Flexible Wings for Biological and Micro Air Vehicles
Ho *et al.* (2003)	Unsteady Flow Control for Flapping Wing Flyers
Mueller and DeLaurier (2003)	Aerodynamics of Small Vehicles
Rozhdestvensky and Ryzhov (2003)	Aerohydrodynamics of Flapping-Wing Propulsors
Sane (2003)	The Aerodynamics of Insect Flight
Lehmann (2004)	The Mechanisms of Lift Enhancement in Insect Flight
Wang (2005)	Dissecting Insect Flight
Ansari *et al.* (2006)	Aerodynamic Modeling of Insect-like Flapping Vehicles
Pines and Bohorquez (2006)	Challenges Facing Future Micro-Air-Vehicle Development
Platzer *et al.* (2008)	Flapping Wing Aerodynamics: Progress and Challenges
Shyy *et al.* (2008)	Aerodynamics of Low Reynolds Number Flyers
Shyy *et al.* (2010)	Recent progress in flapping wing aerodynamics and aeroelasticity

Table 1. A recommended reading list of overviews of the progress made in flapping wing and MAV flight.

Unsteady Mechanism	Illustrative Papers
Clap and fling	Weis-Fogh (1973) Lehmann *et al.* (2005)
Rapid Pitch Mechanism	Dickinson *et al.* (1999) Sane and Dickinson (2002)
Wake Capture	Dickinson *et al.* (1999) Birch and Dickinson (2003) Wang (2005)
Delayed Stall LEV	Ellington (1996) Sane (2003) Shyy and Liu (2007)
Tip Vortex	Shyy *et al.* (2010) Trizila *et al.* (2010)
Persistent Jet	Freymuth (1990) Shyy *et al.* (2009)

Table 2. Selected references on the dominant unsteady mechanisms experienced in flapping wing flight.

Keywords	Resources	Comment
Bumblebee	Sun and Du (2003)	Computational
	Wu and Sun (2005)	Computational
	Berman and Wang (2007)	Computational
	Zuo *et al.* (2007)	Computational
	Nagai *et al.* (2009)	Computational/Experimental
Dragonfly	Kesel (2000)	Experimental
	Maybury and Lehmann (2004)	Experimental
	Sun and Lan (2004)	Computational
	Wang and Sun (2005)	Computational
	Bergou *et al.* (2007)	Observational
	Lu *et al.* (2007)	Experimental
	Tamai *et al.* (2007)	Experimental
	Wang and Russell (2007)	Observational
	Vargas *et al.* (2008)	Computational
	Lehmann (2009)	Computational
	Zhang and Lu (2009)	Computational
Fruitfly	Sane and Dickinson (2001)	Analytical/ Experimental
	Ramamurti & Sandberg (2002)	Computational
	Sun and Tang (2002)	Computational
	Sun and Du (2003)	Computational
	Sun and Wu (2003)	Computational
	Lu *et al.* (2006)	Experimental
	Bergou *et al.* (2007)	Observational
	Berman and Wang (2007)	Computational
	Ramamurti & Sandberg (2007)	Computational
	Liu and Aono (2009)	Computational
Hawkmoth	Ellington *et al.* (1996)	Experimental/Observational
	Liu and Kawachi (1998)	Computational
	Aono and Liu (2006)	Computational
	Bergou *et al.* (2007)	Observational
	Berman and Wang (2007)	Computational
	Aono *et al.* (2008)	Computational
	Bomphrey *et al.* (2008)	Observational
	Aono *et al.* (2009)	Computational
	Liu and Aono (2009)	Computational
Honeybee	Sun and Du (2003)	Computational
	Altshuler *et al.* (2005)	Experimental
	Liu (2009)	Computational
	Liu and Aono (2009)	Computational

Table 3. Selected references for the keywords chosen.

1.1 Unsteady Flight Mechanisms

The flapping wing variety of MAVs [Shyy *et al.* 2010, Shyy *et al.* 2008, Shyy *et al.* 1999], of interest in the current study, take a cue from nature and attempt to mimic the success achieved by insects, birds, and bats [Fearing *et al* 2000, Lentink *et al.* 2007, Pornsin-Sirirak *et al.* 2000]. The study of flapping wing flyers with all of their intricacies is challenging. However significant progress has been made in both engineering and biological communities. Natural flyers utilize flapping mechanisms to generate lift and thrust. These mechanisms are related to formation and shedding of the vortices into the flow, varied wing shape, and structural flexibility. Therefore, understanding the vortex dynamics, the vortex-wing interaction, and the fluid-structure interaction is important. A brief introduction to some of the key unsteady mechanisms associated with flapping wings which are frequently encountered in the literature is given next.

1.1.1 Clap and fling

The earliest unsteady lift generation mechanism to explain how insects fly, found by Weis-Fogh (1973), was the clap-and-fling motion of a chalcid wasp, Encarsia Formosa. Based on the steady-state approximation, the lift generated by the chalcid wasp was insufficient to stay aloft. To explain this, he observed that a chalcid wasp claps two wings together and then flings them open about the horizontal line of contact to fill the gap with air. During the fling motion, the air around each wing acquires circulation in the correct direction to generate additional lift. A schematic of this procedure is shown in Fig. 1.

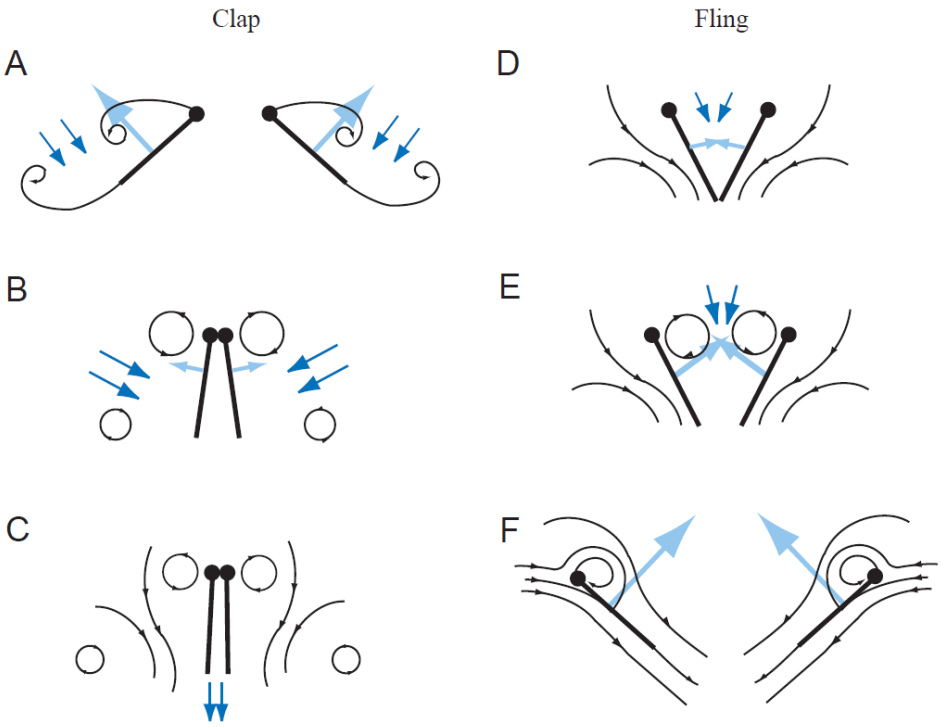

Figure 1. Sectional schematic of wings approaching each other to clap (A-C) and fling apart (D-F) adopted from Sane (2003) and originally described in Weis-Fogh (1973). Black lines show flow lines and dark blue arrows show induced velocity. Light blue arrows show net forces acting on the airfoil. (A-C) Clap. As the wing approach each other dorsally (A), their leading edges touch initially (B), and the wing rotates around the leading edge. As the trailing edges approach each other, vorticity shed from the trailing edge rolls up in the form of stopping vortices (C), which dissipate into the wake. The leading edge vortices also lose strength. The closing gap between the two wings pushes fluid out, giving and additional thrust. (D-F) Fling. The wings fling apart by rotating around the trailing edge (D). The leading edge translates away and fluid rushes in to fill the gap between the two wing sections, giving an initial boost in circulation around the wing system (E). (F) A leading edge vortex forms anew but the trailing edge starting vortices are mutually annihilated as they are of opposite circulation.

Lehmann, Sane, and Dickinson (2005) elucidated this clap-and-fling mechanism with PIV flow visualizations and force measurements using a

dynamically-scaled robotic wing model. Also numerical investigations further demonstrated lift enhancement due to the clap-and-fling mechanisms at low Reynolds numbers [Sun and Yu 2003, Sun and Yu 2006, Miller and Peskin 2004, Miller and Peskin 2005, Liu and Aono 2009]. The relative benefit of clap-and-fling lift enhancement strongly depended on stroke kinematics and could potentially increase the performance by reducing the power requirements [Lehmann and Pick 2007, Lehmann 2009]. The clap-and-fling mechanism is beneficial in producing a mean lift coefficient to keep a low weight flyer aloft: numerous natural flyers, such as hawkmoths, butterflies, fruitflies, wasps, and thrips enhance their aerodynamic force production with the clap-and-fling mechanism [Weis-Fogh 1973, Cooter and Baker 1977, Brodsky 1991, Brachenbury 1990, Srygley and Thomas 2002].

1.1.2 Rapid Pitch Mechanism

At the end of each stroke, flapping wings can experience rapid pitching rotation, which can enhance the aerodynamic force generation [Dickinson *et al.* 1999]. The phase difference between the translation and the rotation can be utilized as a lift controlling parameter: similar to the Magnus effect where the rotating body's no-slip surface will drag surrounding air, accelerating the fluid in the direction of motion on one side and impeding it on the other side of the body thereby creating a pressure difference and sideways force. If the wing flips before the stroke ends, then the wing undergoes rapid pitch-up rotation in the correct translational direction enhancing the lift. This is called the advanced rotation. On

the other hand, in delayed rotations, if a wing rotates back after the stroke reversal, then when the wing starts to accelerate it pitches down resulting in reduced lift [Dickinson *et al.* 1999]. In a follow-up study Sane and Dickinson (2002) related the lift peak at the stroke ends to be proportional to the angular velocity of the wing using the quasi-steady theory. The numerical studies [Shyy *et al*. 2008, Sun and Tang 2002] showed an increase in the vorticity around the wing due to rapid pitch-up rotation of the wing led to augmentation of the lift generation.

1.1.3 Wake Capture

The wake capture mechanism is often observed during a wing-wake interaction. When the wings reverse their translational direction, the wings meet the wake created during the previous stroke, by which the effective flow velocity increases and additional aerodynamic force peak is generated.

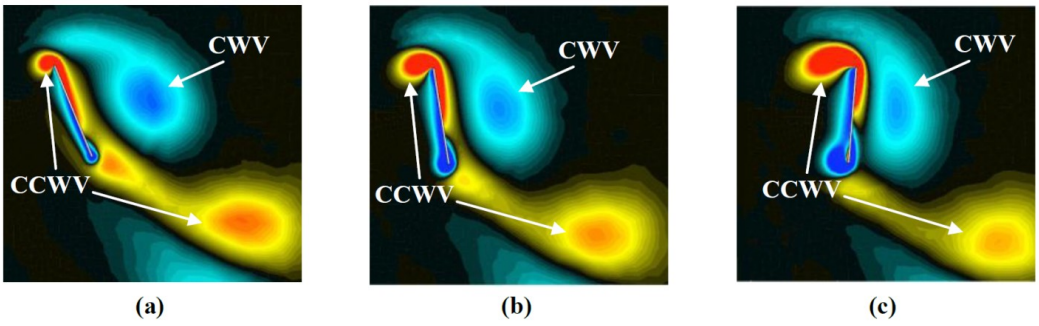

Figure 2. Illustrations of wake capture mechanism [Shyy *et al.* (2008a, 2009)]. (a) Supination,(b) beginning of upstroke, and (c) early upstroke. At the end of the stroke, (a), the wake shed in the previous stroke denoted by CWV is en route of the flat plate. As the flat plate moves into the wake (b-c) the effective flow velocity increases and additional aerodynamic force is generated. The

color of contour indicates spanwise-component of vorticity. CWV and CCWV indicate clock-wise and counter clock-wise vortex.

Lehmann, Sane and Dickinson (2005), Dickinson *et al.* (1999), and Birch and Dickinson (2003) examined the effect of wake capturing of several simplified fruit fly-like wing kinematics using a dynamically-scaled robotic fruit fly wing model at Re= $1.0\text{-}2.0\times10^2$. They compared the force measurement data with the quasi-steady approximation, then isolated the aerodynamic influence of the wake. Results demonstrated that wake capture force represented a truly unsteady phenomenon dependent on temporal changes in the distribution and magnitude of vorticity during stroke reversal. The sequence of the wake capture mechanism is illustrated in Fig. 2. Wang (2005) and Shyy *et al.* (2008, 2009) further elucidated the wake capture mechanism and lift augmentation of the instantaneous lift peak using 2-D numerical simulations. The effectiveness of the wake capture mechanism was a function of wing kinematics and flow structures around the flapping wings [Shyy *et al.* 2008, Lehmann *et al.* 2005, Dickinson *et al.* 1999, Birch and Dickinson 2003]. A different view on the effect of wake capture existed as well. Jardin et al. (2009) used a NACA0012 airfoil under asymmetric flapping wing kinematics such that in the downstroke the interaction of the previously shed wake with the leading edge vortex (LEV) formation was reduced. In most cases they considered this reduced effect of wake capture led to a closely attached downstroke LEVs. Compared to a synchronized wing rotation they saw enhanced downstroke aerodynamic loading.

1.1.4 Delayed Stall of a Leading Edge Vortex (LEV)

Ellington *et al.* [(1996), van den Berg and Ellington (1997a,b), Willmott *et al.* 1997] suggested that the delayed stall of LEV can significantly promote lift associated with a flapping wing. The LEV created a region of lower pressure above the wing and hence it would enhance lift. Multiple follow-up investigations [Liu and Kawachi (1997), Liu *et al.* (1998), Liu (2002, 2005)] were conducted for different insect models, resulting in a better understanding of the role played by the LEV and its implications on lift generation. When a flapping wing travels several chord lengths, the flow separates from the leading and trailing edges, as well as at the wing tip, and forms large organized vortices known as a leading edge vortex (LEV), a trailing edge vortex (TEV), and a tip vortex (TiV). In flapping wing flight, the presence of LEVs is essential to delay stall and to augment aerodynamic force production during the translation of the flapping wings as shown in Fig. 3 [Sane 2003]. Fundamentally, the LEV is generated and sustained from the balance between the pressure-gradient, the centripetal force, and the Coriolis force in the Navier-Stokes (NS) equations. The LEV generates a lower pressure area in its core, which results in an increased suction force on the upper surface. Employing 3-D NS computations, Liu and Aono (2009) and Shyy and Liu (2007) demonstrated that a LEV is a common flow feature in flapping wing aerodynamics at Reynolds numbers O(100) and lower, which correspond to the flight regime of insects and flapping wing MAVs. However, main characteristics and implications of the LEV on the lift generation varied with

changes in the Reynolds number, the reduced frequency, the Strouhal number, the wing flexibility, and flapping wing kinematics.

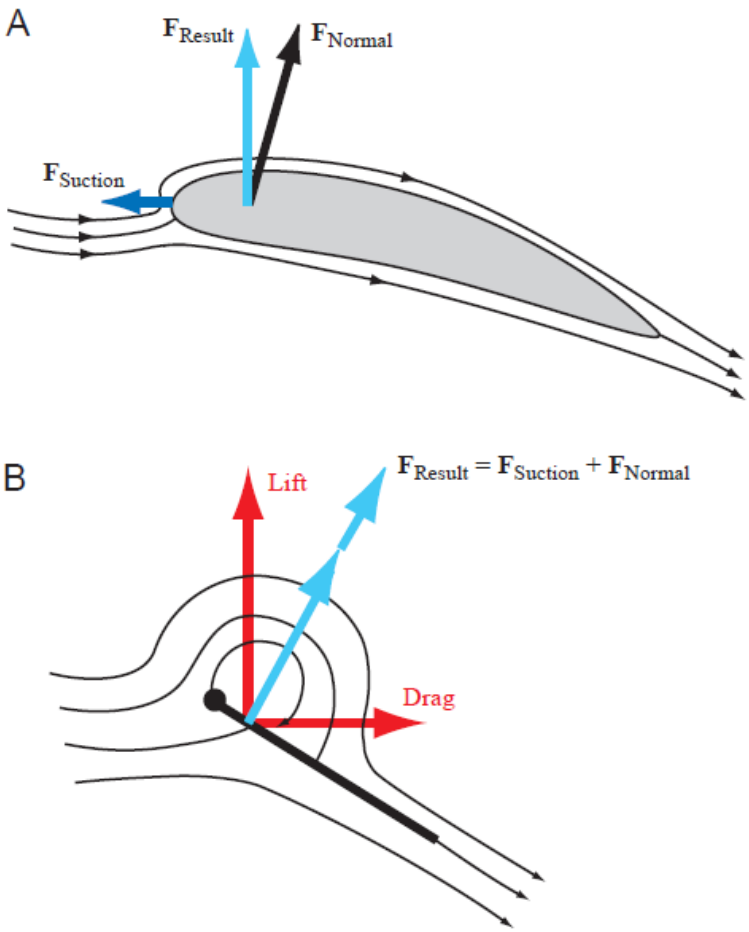

Figure 3. Leading edge suction analogy adopted from Sane (2003). (A) Flow around the blunt wing. The sharp diversion of flow around the leading edge results in a leading edge suction force (dark blue arrow), causing the resultant force vector (light blue arrow) to tilt towards the leading edge and perpendicular to free stream. (B) Flow around a thin airfoil. The presence of a leading edge vortex causes a diversion of flow analogous to the flow around the blunt leading edge in (A) but in a direction normal to the surface of the airfoil. This results in an enhancement of the force normal to the wing section.

Milano and Gharib (2005) measured the forces generated by a pitching rectangular flat plate at approximately Re= $O(10^3)$ and observed the trajectories yielding maximum average lift based on a genetic algorithm. Results showed the optimal flapping produces LEVs of maximum circulation and that a dynamic formation time that described the vortex formation process of about 4 is associated with production of a maximum-circulation vortex [Gharib *et al.* (1998), Dabiri (2009)]. Rival et al. (2009) investigated experimentally the formation process of LEVs associated with several combinations of pitching and plunging SD7003 airfoils in forward flight using PIV at Re= $O(10^4)$. Results suggested that by carefully tuning the airfoil kinematics, thus gradually feeding the LEV over the downstroke, it was to some extent possible to stabilize the LEV without the necessity of a spanwise flow.

Tarascio et al. (2005) and Ramasamy and Leishman (2006) visualized the flow fields around a biologically-inspired flapping wing at Re= $O(10^4)$ by a mineral oil fog strobed with a laser sheet and PIV. They presented the presence of a shed dynamic stall vortex that spans across most of the wing span and multiple shedding LEVs on the top surface of the wing during each wing stroke. Also they provided several observations related to the role of turbulence at low Reynolds numbers. Poelma et al. (2006) measured the time-dependent 3-D velocity field around a flapping wing at Re= $O(10^4)$ based on maximum chord. A dynamically-scaled fruitfly wing in mineral oil with hovering kinematics extracted from real insect movements was used. They presented refined 3-D structures of LEVs and

suggested including the counter-rotating TEVs to get a complete picture for production of circulation. Lu and Shen (2008) highlighted the detailed structures of LEVs for a flapping wing in hover at Re = $O(10^3)$. They used phase-lock based multi-slice digital stereoscopic PIV to show that the spanwise variation along the LEV was time-dependent. Their results demonstrated that the observed LEV systems were a collection of four vortical elements: one primary vortex and three minor vortices, instead of a single conical or tube-like vortex as reported or hypothesized in previous studies [Dickinson *et al.* (1999), Ellington *et al.* (1996)]. Recently, Pick and Lehmann (2009) used 3-D three-components Multiple-Color-Plane Stereo PIV techniques to obtain a 3-D velocity field around a flapping wing. The need for 3-D PIV is evident since the critical flow features in understanding flapping wing aerodynamics, such as LEVs and unsteady wakes behind an insect body, are inherently 3-D in nature. Compared to the previous findings, they reported similar structure of the LEV but stronger outward axial flow inside the LEV of up to 80% of the maximum in-plane velocity. On the other hand, Liang et al. (2010) presented results based on direct numerical simulation to investigate wake structures of hummingbird hovering flight and associated aerodynamic performance. They reported that the amount of lift produced during downstroke is about 2.95 times of that produced in upstroke. Two parallel vortex rings were formed at the end of the upstrokes. There is no obvious leading edge vortex that can be observed at the beginning of the upstroke. Although only rigid wing structures were considered, the results were claimed to be in good

agreement with PIV measurements of Warrick et al. (2005) and Altshuler et al. (2009).

1.1.5 Tip vortex

Tip vortices (TiVs) associated with fixed finite wings are seen to decrease lift and induce drag [Anderson (2006)]. However, in unsteady flows, TiVs have been seen to influence the total force exerted on the wing in three ways: i) creating a low pressure area near the wing tip [Shyy *et al.* (2009), Aono *et al.* (2008, 2009), Ramamurti and Sandberg (2007), Ringuette *et al.* (2007)], ii) an interaction between the LEV and the TiV [Shyy *et al.* (2009), Aono *et al.* (2008, 2009), Ramamurti and Sandberg (2007), Ringuette *et al.* (2007)], and iii) constructing wake structures by interactions from the downward and radial influence of the root vortex and TiV [Ramasamy and Leishmann (2006)]. The first two mechanisms ((i) and (ii)) also were observed for impulsively started flat plates normal to the motion with low aspect ratios: Riguette et al. (2007) presented experimentally that the TiVs contributed substantially to the overall plate force by interacting with the LEVs at Re = $O(10^3)$. Taira and Colonius (2009) utilized the immersed boundary method (IBM) to highlight the 3-D separated flow and vortex dynamics for a number of low aspect ratio flat plates at different angles of attacks at Re of $O(10^2)$. They showed that the TiVs could stabilize the flow and exhibited nonlinear interaction with the shed vortices. Stronger influence of downwash from the TiVs resulted in reduced lift for lower aspect ratio plates.

For flapping motion in hover, however, depending on the specific kinematics, the TiVs could either promote or make little impact on the aerodynamics of a low aspect ratio flapping wing. Shyy et al. [55] demonstrated that for a flat plate with AR = 4 at Re = 64 with delayed rotation kinematics, the TiV anchored the vortex shed from the leading edge increasing the lift compared to a 2-D computation under the same kinematics. On the other hand, under different kinematics with small angle of attack and synchronized rotation, the generation of TiVs was small and the aerodynamic loading was well approximated by the analogous 2-D computation. They concluded that the TiVs could either promote or make little impact on the aerodynamics of a low aspect ratio flapping wing by varying the kinematic motions [Shyy *et al.* 2009].

1.1.6 Induced Jet

As a high aspect ratio wing repeats a periodic hovering motion, the shed vortices may sustain a pocket of downward momentum initiated by the wing as it pitches and plunges, illustrated in Fig. 4. This has been seen experimentally by Freymuth (1990) and numerically by Trizila *et al.* (2008a,b). Figure 5 illustrates a representative vertical velocity and vorticity field and unpublished results will be shown in the appendix as to the magnitude of impact it can have on the flowfield and force histories. The wing encounters the persistent jet which accelerates the flow along its underside. This decreases the lift of the wing and can introduce or accentuate asymmetries in the force history, despite symmetric kinematics, as the jet evolves a bias either behind or in front of the center of stroke position.

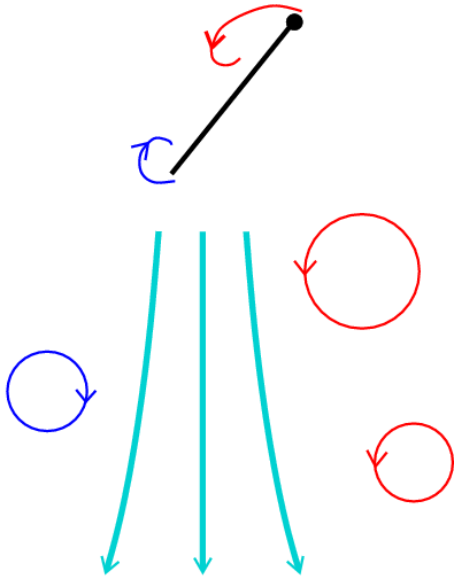

Figure 4. Illustration of the shed vortices reinforcing the downward momentum created as the wing flaps.

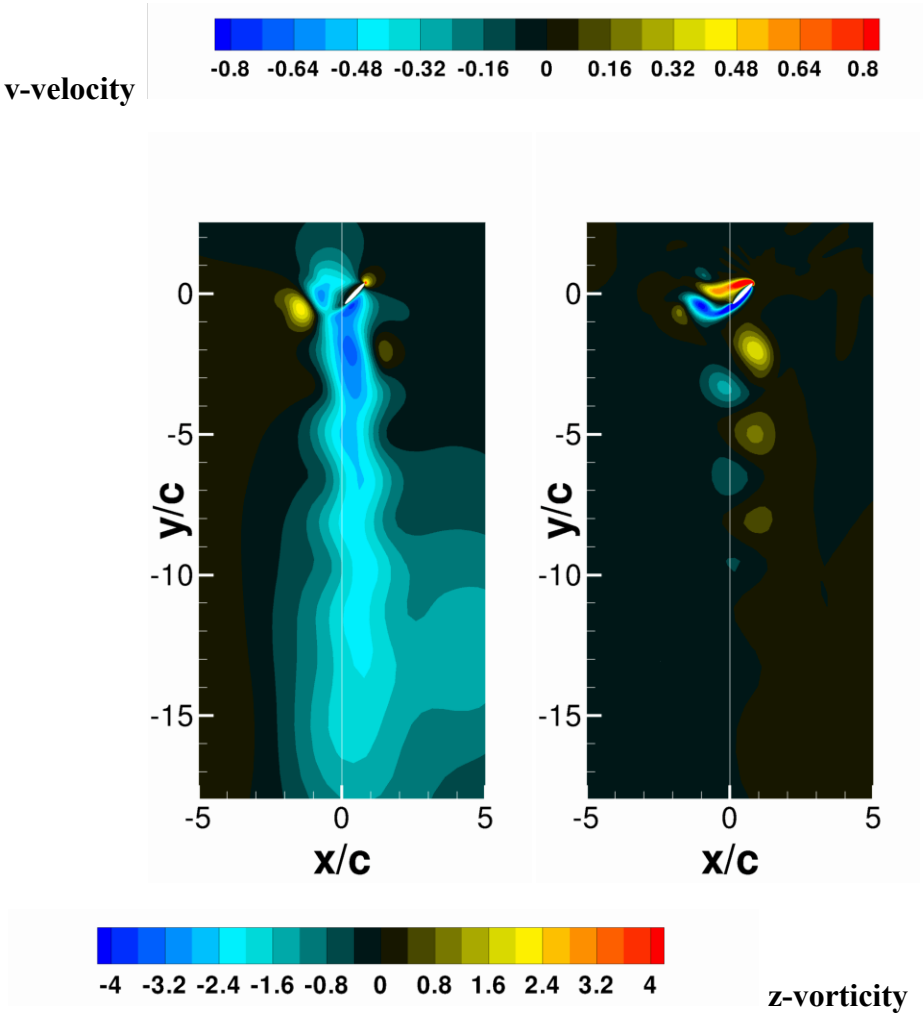

Figure 5. Vertical velocity (left) and vorticity (right) contours of a two-dimensional case at Re=100 hovering case governed by $2h_a/c=3.0$, $\alpha_a= 45°$, $\phi=90$. The persistent jet is expressed as the darker blue region in the v-velocity plots.

1.1.7 Passive Pitching Mechanism

Wing torsional flexibility can allow for a passive pitching motion due to the inertial forces during wing rotation at stroke reversals [Ennos (1987, 1988a, 1988b, 1999), Ishihara *et al.* (2009)]. There were three modes of passive pitching motions which were similar to those suggested by rigid robotic wing model experiments [Dickinson *et al.* (1999)]; 1) delayed pitching, 2) synchronized

pitching, and 3) advanced pitching. It was found that the ratio of flapping frequency and the natural frequency of the wing were important to determine the modes of passive pitching motions of the wing [Ishihara *et al.* (2009), Vanella *et al.* (2009)]. If the flapping frequency was less than the natural frequency of the wing, then the wing experienced an advanced pitching motion, which led to lift enhancement by intercepting the stronger wake generated during the previous stroke [Vanella *et al.* (2009)]. Moreover, it was shown for 2-D flows, the LEVs produced by the airfoil motion with passive pitching seemed to attach longer on the flexible airfoil than on a rigid airfoil [Ishihara *et al.* (2009)].

1.1.8 Vortex Dynamics

The above discussion show that vortex dynamics play an important role in the force generation during flapping wing flight. The act of quantifying the vortex dynamics is an area of study unto itself. A common way of illustrating vortex dynamics, and used extensively in the present document, is through vorticity, the curl of velocity [Anderson (2006)]:

$$\nabla \times \boldsymbol{u} \tag{1}$$

In certain circumstances vorticity in and of itself, while useful, is not conclusive. Particularly in regions of sheer flow vorticity may be significant but streamline curvature negligible. Another quantity used in the present document is the second invariant of the velocity gradient tensor referred to as the Q criterion [Hunt *et al.* (1988)]:

$$Q = -\frac{1}{2}\frac{\partial u_i}{\partial x_j}\frac{\partial u_j}{\partial x_i} = -\frac{1}{2}\left(S_{ij}S_{ij} - \frac{1}{2}\omega_i\omega_i\right) \quad (2)$$

Here **S** is the rate of strain tensor, and **ω** is the vorticity vector, both in indicial notation. One advantage of using this criterion over the vorticity is that the shear and rotational components are separated, e.g. a boundary layer will exhibit high vorticity but lacks coherent vortices. This in turn allows for additional possibilities in following the vortex dynamics as a vortex can be better quantified.

Another popular approach in fluid dynamics for studying time dependent flows is through the calculation of Lagrangian Coherent Structures (LCS). One strength is the ability to discern transport properties not immediately evident in the Eulerian frame. One potential drawback is that the computational cost can be significant as either many points or a method for surface tracking which is advected in time must be resolved. This technique is not used in the current study, but the interested reader is referred to Shadden *et al.* (2005), Green *et al.* (2007), Lipinski and Mohseni (2009), and Wilson *et al. (2009)* for theoretical formulation, numerical implementation, and practical applications.

1.2 Kinematics, Geometry, Flexibility, and Re Effects in Flapping Wing Aerodynamics

This section presents a literature survey on flapping wing aerodynamics using experimental, theoretical, and computational approaches.

Experimentally, numerous previous efforts on flow visualization around biological flyers have been made, including smoke visualizations [Brodsky

(1991), Srygley and Thomas (2002), Willmott *et al.*(1997), Thomas *et al.* (2004), Bomphrey *et al.* (2009)] and PIV measurements [Warrick *et al.* (2005,2009), Altshuler *et al.* (2009), Hubel *et al.* (2009), Tobalske *et al.* (2009), Videler *et al.* (2004), Bomphrey *et al.* (2005), Bomphrey (2006), Hedenstrom *et al.* (2007, 2009), Muijres *et al.* (2008)]. The advance of such technologies has enabled researchers to obtain not only 2-D but also 3-D flow structures around biological flyers [Hubel *et al.* (2009), Warrick *et al.* (2009), Hedenstrom *et al.* (2007, 2009), Muijres *et al.* (2008)] and/or scaled models [Poelma *et al.* (2006), Lu and Shen (2008), Pick and Lehmann (2009)] with reasonable resolution in space. At the same time, measurements of wing and body kinematics have been conducted using high-speed cameras [Wakeling and Ellington (1997), Willmott and Ellington (1997a,b), Fry *et al.* (2003), Tian *et al.*(2006), Riskin *et al.* (2008), Wallance *et al.* (2006), Hedrick (2008), Ristroph *et al.* (2009)], laser techniques (a scanning projected line method [Zeng *et al.* (2000)], a reflection beam method [Zeng *et al.* (2001)], a fringe shadow method [Zeng *et al.* (1996)], and a projected comb fringe method [Song *et al.* (2001)]), and a combination of high-speed cameras and a projected comb-fringe technique with the Landmarks procedure [Wang *et al.* (2003)]. Advancement in measurement techniques also enabled quantification of flapping wing and body kinematics along with the 3-D deformation of the flapping wing. Recently, data on the instantaneous wing kinematics involving camber along the span, twisting, and flapping motion have been reported (a hovering honeybee [Zhang *et al.* (2008)]; a hovering hover fly

and a tethered locust [Walker *et al.* (2008, 2009)], a free-flying hawkmoth [Wu and Zeng (2009)]). These efforts help in establishing more complex and useful computational models [Zheng *et al.* (2009), Young *et al.* (2009)]. Furthermore, the in-vivo measurement of aerodynamic forces generated by biological flyers in free-flight is a challenging research topic.

Various models have been developed in an effort to understand flapping wing phenomena where the variables and ambient conditions are known, controllable, and repeatable. Detailed discussion regarding the experimental and numerical methodologies utilized to examine flapping wing related studies is beyond the scope of the current effort. Suffice it to say, numerous computational techniques based on moving meshes [Shyy *et al.* (2006), Tezduyar *et al.* (1992), Lesoinne and Farhat (1996)] or stationary meshes (cut cell or immersed boundary) [Shyy (1994), Mittal *et al.* (2005)] have been developed. The physical models include NS as well as simplified treatments [Katz and Plotkin (2001), Ansari *et al.* (2006)]. Some of the experimental methods employed are introduced in the paragraph above.

In the following section recent progress regarding rigid flapping wing aerodynamics is presented. First, studies for forward flight will be described. Then studies for hovering flight will be presented. Explorations on the implications of wing kinematics and wing shape will be touched upon after that. This will be followed by a highlight focusing on the unsteady aerodynamics of 2-

D and 3-D hovering flat plates, Re = $O(10^2)$, based on a surrogate modeling approach. Finally, the fluid dynamics related to the LEV, the TEV, and the TiV will be presented, including the authors' computational efforts to highlight the vortex dynamics of a hovering hawkmoth at Re = $O(10^3)$ and the effect of Reynolds number (size of flyers) on the LEV structures and spanwise flow.

1.2.1 Single Wing in Forward Flight Conditions

Von Ellenrieder et al. (2003) studied the impact of variation of Strouhal number ($0.2< St< 0.4$), pitch amplitude ($0° < \alpha_a < 10°$), and phase angle ($65° < \phi < 120°$) between pitching and plunging motion on 3-D flow structures behind a plunging/pitching finite-span NACA0012 wing using dye flow visualization at Re= O(100). The results demonstrated that the variation of these parameters had observable effects on the wake structure. However, they observed a representative pattern of the most commonly seen flow structures and proposed a 3-D model of the vortex structure behind a plunging/pitching wing in forward flight. Godoy-Diana et al. (2009) investigated the vortex dynamics associated with a pitching 2-D teardrop shaped airfoil ($2.2°< \alpha_a < 16.9°$, $0.1< St< 0.5$) in forward flight at Re = $O(10^3)$ using PIV measurements. Their results illustrated the transition from the von Kármán vortex streets to the reverse von Kármán vortex streets that characterize propulsive wakes. Furthermore, the symmetry breaking of this reverse von Kármán vortex pattern gave rise to an asymmetric wake which was intimately related to the time-averaged aerodynamic force production. Lee et al. (2008) numerically investigated aerodynamic characteristics of unsteady force

generation by a 2-D pitching and plunging 5% thick elliptic airfoil with inclined stroke plane at Re= O(100). They showed that the thrust was generated due to correct alignment of the vortices at the end of the upstroke and there was a monotonic decrease in thrust as the rotational center of the pitching motion was moved from the leading edge towards the trailing edge ($0.1 < X < 0.5$).

Anderson et al. (1998) considered harmonically oscillating NACA0012 airfoils in a water tunnel to measure the thrust. After a parametric study ($0° < \alpha_a < 60°$, $0.25 < h_a/c < 1.0$, $30° < \phi < 110°$) to find the optimum flow condition for the thrust generation ($\alpha_a = 30°$, $h_a/c = 0.75$, $\phi = 75°$) at Re= $O(10^4)$ and St= 0.05-0.6, they proceeded to show the presence of a reverse von Kármán vortex street formed by the vortices shed from the leading and trailing edges for St in the range of 0.3 and 0.4 at Re= $O(10^3)$. Triantafyllou and co-workers [Read *et al.* (2003), Hover *et al.* (2004), Schouveiler *et al.* (2005)] performed parametric investigations using experiments on the performance of a pitching/plunging NACA0012 airfoil in forward flight at Re $O(10^4)$, and St between 0.1 and 0.45. Systematic measurements of the fluid loading showed a unique peak efficiency of more than 70% for optimal combinations of the parameters (e.g. $h_a/c = 0.75$, $\alpha_a = 15°$, and $\phi = 90°$ at St = 0.25 gives an efficiency of 73%) and observed that higher thrust can be expected when increasing the Strouhal number and/or the maximum of the angle of attack. Then a parametric range where the efficiency and high thrust conditions were achieved together would fall in the parameter domain they considered. Lai and Platzer (1999) used LDV and dye injection techniques to

visualize the velocity field and the wake structures of an oscillating NACA0012 airfoil in water at Re $O(10^2)$ to $O(10^4)$. The transition from drag to thrust was seen to depend on the non-dimensional plunge velocity (kh_a which is proportional to St), i.e. for $kh_a>0.4$ the considered airfoil was thrust-producing. Cleaver et al. (2010) performed force and supporting PIV measurements on a plunging NACA0012 airfoil at a Reynolds number of $O(10^4)$, at pre-stall, stall, and post-stall angles of attack. The lift coefficient for pre-stall and stall angles of attack at larger plunge amplitudes showed abrupt bifurcations with the branch determined by initial conditions. With the frequency gradually increasing, high positive lift coefficients were observed, this was termed mode A. At the same frequency with the airfoil impulsively started, negative lift coefficients were observed, this was termed mode B. The mode A flow field is associated with trailing edge vortex pairing near the bottom of the plunging motion causing an upwards deflected jet, and a resultant strong upper surface leading edge vortex. The mode B flow field is associated with trailing edge vortex pairing near the top of the plunging motion causing a downwards deflected jet, and a resultant weak upper surface leading edge vortex. The bifurcation was not observed for plunge small amplitudes due to insufficient trailing edge vortex strength, nor at post-stall angles of attack due to greater asymmetry in the strength of the trailing-edge vortices, which creates a natural preference for a downward deflected mode B wake.

Lewin and Haj-Hariri (2003) conducted 2-D numerical investigations for fluid dynamics associated with elliptic-like plunging airfoils at Re $O(10^2)$ and

compared and contrasted the findings with ideal flow theories. They mentioned that for high-frequency plunging, the vorticity was shed primarily from the trailing edge, and therefore better matched the inviscid models. However, for high kh_a the LEV and its secondary vortices were occasionally shed into the wake, which would differentiate the physics from those found in inviscid models. The monotonic trend found in ideal fluid models of efficiency decreasing as reduced frequency increases, was not seen in the numerical models where the maximum efficiency was found for an intermediate range of reduced frequencies. Lua et al. (2007) experimentally examined the wake structure formation of a 2-D elliptic airfoil undergoing a sinusoidal plunging motion at $Re = O(10^3)$ and $k = 0.1$ to 2.0. The results showed the type of wake structure produced depends on not only the reduced frequency, but also on the normalized stroke amplitude. Bohl and Koochesfahani (2009) focused on quantifying, via MTV, the vortical structures in the wakes of a sinusoidally pitching NACA0012 airfoil with low pitching amplitude, $\alpha_a = 2°$, at $Re = O(10^4)$. The reduced frequency was set to a relatively high range, between 4.1 and 11.5, to generate thrust. They found that the transverse alignment of the vortices switched at $k = 5.7$, i.e. the vortices of positive circulation switched from below to above the vortices of negative circulation. The mean streamwise velocity profile herewith changed from velocity deficit (wake) to velocity excess (jet). However this switch from the vortex array orientation could not be used to determine the crossover from drag to thrust. Von Ellenrieder and Pothos (2008) conducted PIV measurements behind a 2-D

plunging NACA0012 airfoil, operating at St between 0.17-0.78 and Re= $O(10^4)$. Their results showed that for Strouhal numbers larger than 0.43, the wake became deflected such that the average velocity profile was asymmetric about the mean heave position of the airfoil. Jones and Babinsky (2010) studied the fluid dynamics associated with a three-dimensional 2.5% thick waving flat plate. The spanwise velocity gradient and wing starting and stopping acceleration that exist on an insect-like flapping wing are generated by rotational motion of a finite span wing. The flow development around a waving wing at Re = $O(10^4)$ was studied using high speed PIV to capture the unsteady velocity field. Vorticity field computations and a vortex identification scheme reveal the structure of the 3-D flow-field, characterized by strong leading edge and tip vortices. A transient high lift peak approximately 1.5 times the quasi-steady value occurred in the first chord-length of travel, caused by the formation of a strong attached leading edge vortex. This vortex then separated from the leading edge, resulting in a sharp drop in lift. As weaker leading edge vortices continued to form and shed, lift values recovered to an intermediate value. They also reported that the wing kinematics had only a small effect on the aerodynamic forces produced by the waving wing if the acceleration is sufficiently high. Calderon et al. (2010) presented an experimental study on a plunging rectangular wing with aspect ratio of 4, at low Re $O(10^4)$. Time-averaged force measurements were presented as a function of non-dimensional frequency, alongside PIV measurements at the mid-span plane. In particular, they focused on the effect of oscillations at low amplitudes and

various angles of attack. The presence of multiple peaks in lift was identified for this 3-D wing, thought to be related to the natural shedding frequency of the stationary wing. Wing/vortex and vortex/vortex interactions were identified which may also contribute to the selection of optimal frequencies. Lift enhancement was observed to become more notable with increasing plunging amplitude, to lower reduced frequencies, with increasing angle of attack. Despite the highly 3-D nature of the flow, lift enhancements up to 180% were possible.

Under the Research and Technology Organization (RTO) arrangement of the North Atlantic Treaty Organization (NATO) there was a community-wide effort organized, which offered a wide range of experimental and computational data for both the SD7003 airfoil and flat plate, with kinematics promoting different degrees of flow separation. The detailed information can be found in [Ol *et al.* (2009a)]. Here we present samples of the information collected in this group endeavor. Ol et al. (2009b) compared PIV flow field measurements of a pitching and plunging SD7003 airfoil at Re = $O(10^4)$, k = 0.25, and St = 0.08 with computed results by Kang et al. (2009). They considered two kinematic motions, a shallow-stall case and a deep-stall case where the maximum effective angle of attack was larger than the former case. In the shallow-stall case where the flow was moderately attached overall, the computed result was able to approximate the flow field measured using PIV well. For the deep-stall case the flow separated just before the middle of the downstroke (i.e. maximum effective angle of attack). The numerical solution showed vortical structures similar to the PIV, but at a later

phase of motion. However, the instantaneous lift over a motion cycle obtained from both methods compared well, indicating that the differences in details of the flow structures do not necessarily lead to large differences in the forces integrated over the airfoil, as long as the large scale flow structures remain similar.

For Re (10^4) and higher, turbulence influences the development of the flow structures and forces. Ol *et al.* (2009a), Baik *et al.* (2009) investigated the fluid physics at Re = O(10^4) of a pitching and plunging SD7003 airfoil and flat plate, experimentally using PIV focusing on the second order turbulence statistics. They observed laminar boundary layer and laminar-to-turbulence transition. In a companion paper Kang et al. (2009) used RANS computations with the SST turbulence model [Menter (1993)] to simulate the same cases [146] to investigate the implications of the turbulence modeling. By limiting the production of turbulence kinetic energy they observed that leading edge separation was dependent on the level of eddy viscosity for the SD7003 airfoil, and hence turbulence, in the flow. Regarding the computed lift, they concluded that the large scale vortical structures in the flow were the contributing factors. Baik et al. (2010) conducted an experimental study of a pitching and plunging flat plate at Re = O(10^4) constrained to motions enforcing a pure sinusoidal effective angle of attack. The effect of non-dimensional parameters governing pitching and plunging motion including Strouhal number (St), reduced frequency (k), and the plunge amplitude (h_a) was investigated for the same effective angle of attack kinematics. The formation phase of the LEV was found to be dependent on k: the LEV

formation is delayed for higher k value. It was found that for cases with the same k the velocity profiles normal to the airfoil surface closely follow each other in all cases independent of pitch rate and pivot point effect. Of course, even though the flow structures with constant k seemed little affected by Strouhal number and plunging amplitude, the time history of forces along the horizontal (thrust) and normal (lift) directions can be substantially altered because the geometric angle-of-attack, viewed from the ground.

Visbal *et al.* (2009) computed the unsteady transitional flow over a plunging 2-D and 3-D SD7003 airfoil with high reduced frequency (k= 3.93) and low plunge amplitude (h_a/c= 0.05) using implicit Large Eddy Simulations at Re = $O(10^4)$. The results showed that the generation of dynamic-stall-like vortices near the leading edge was promoted due to motion-induced high angles of attack and 3-D effects in vortex formation around the wing. Radespiel et al. (2007) compared the flow field over a SD7003 airfoil with and without plunging motion at Re= 6.0×10^4. Using a NS solver along with the linear stability analysis to predict transition from laminar-to-turbulent flow, they concluded that transition and turbulence can play an important role in the unsteady fluid dynamics of flapping airfoils and wings at the investigated Reynolds numbers.

1.2.2 Single Wing in Hovering Flight Conditions

Ellington and co-workers [Ellington *et al.* (1996), van den Berg *et al.* (1997a,b), Willmott *et al.* (1997), Liu *et al.* (1998), Willmott and Ellington

(1997a,b)] did pioneering research on flapping wing aerodynamics at Re= $O(10^3)$. They built a scaled-up robotic hawkmoth wing model and visualized the flow field of hovering hawkmoth wing movements [Ellington *et al.* (1996), van den Berg *et al.* (1997a,b), Willmott *et al.* (1997), Liu *et al.* (1998), Willmott and Ellington (1997a,b)] using smoke visualization techniques. They observed that the presence of the LEV at high angle of attack during the downstroke, and suggested that 'delayed stall' of the LEV was responsible for high lift production by hovering hawkmoths. Dickinson and co-workers [Dickinson (1994, 2005, 2006), Lehmann *et al.* (2005), Dickinson *et al.* (1999), Sane and Dickinson (2001, 2002), Poelma *et al.* (2006), Birch and Dickinson (2001, 2004), Dickson and Dickinson (2004), Fry *et al.* (2005), Altshuler *et al.* (2005)] made original contributions to the understanding of the flapping wing aerodynamics at lower Reynolds number regimes (Re= $O(10^2)$ – $O(10^3)$). They utilized a dynamically-scaled robotic fruit fly model wing in an oil tank and conducted systematic experiments to relate the prescribed simplified fly-like kinematics to the resulting aerodynamic forces. They categorized the aerodynamic loading into three parts: forces due to i) translation (delayed stall of the LEV [Dickinson *et al.* (1999), Poelma *et al.* (2006), Sane and Dickinson (2001), Birch and Dickinson (2001), Birch *et al.* (2004)], ii) rotation [Dickinson *et al.* (1999), Sane and Dickinson (2002), Dickinson (1994), Dickson and Dickinson (2004)], and iii) interaction with the wakes (wake capture [Dickinson *et al.* (1999), Shyy *et al.* (2009)]). Furthermore, Fry *et al.* (2005) investigated the aerodynamics of hovering/tethered fruit flies

using a dynamically-scaled robotic fruit fly wing model at Re =O(10^2). Altshuler *et al.* (2005) studied the aerodynamics of a hovering honeybee using a dynamically-scaled robotic honeybee wing model at Re = O(10^3). Their results showed that aerodynamic force enhancement due to wake capturing and rotational forces were important in both fruit fly and honeybee hovering. Sunada *et al.* (2002) measured fluid dynamic forces generated by a bristled wing model with four different wing kinematics using scaled-up robotic wings at Re = O(10). The results demonstrated that fluid dynamic forces acting on the bristled wing were a little smaller than those on the solid wings.

Nagai *et al.* (2009) used a mechanical bumblebee wing model and measured the resulting forces with strain gauges and flow structures using PIV for a hovering and forward flight at Re= O(10^3). The comparison between the experimental results and the numerical solutions, computed using a 3-D NS code, showed good agreement quantitatively in forces and qualitatively in flow structures. For the forward flight the relevance of the delayed stall mechanism depended on the advance ratio. They observed that the LEV hardly appeared during upstroke at high advance ratios (over 0.5).

Comparisons of 2-D computational simulations of an elliptic airfoil in hover against 3-D experimental data of the fruit fly model [Dickinson *et al.* (1999)] were performed by Wang *et al.* (2004). They concluded that 2-D computed aerodynamic forces were good approximations of 3-D experiments for

the advanced and symmetrical rotation cases considered in their study. Lua *et al.* (2008) experimentally investigated the aerodynamics of a plunging 2-D elliptic airfoil at Re between $O(10^2)$ and $O(10^3)$. The results showed that the fluid inertia and the LEVs played dominant roles in the aerodynamic force generation, and time-resolved force coefficients during plunging motion were found to be more sensitive to changes in pitching angular amplitude than to Reynolds number. Wang [(2000a,b), (2004)] carried out 2-D numerical investigations on the vortex dynamics associated with a plunging/pitching elliptic airfoil at Re= $O(10^2)$ – $O(10^4)$. The result showed a downward jet of counter rotating vortices which were formed from LEVs and TEVs. Bos *et al.* (2008) performed 2-D computational studies examining different hovering kinematics: simple harmonic, experimental model [Dickinson *et al.* (1999)], realistic fruit fly [Fry *et al.* (2005)], and modified fruit fly. The results showed that the realistic fruit fly kinematics lead to the optimal mean lift-to-drag ratio compared to other kinematics. Also they concluded that in the case of realistic fruit fly wing kinematics, the angle of attack variation increases the aerodynamic performance, whereas the deviation levels the forces over the flapping cycle. Kurtulus *et al.* (2008) obtained a flow field over a pitching/plunging NACA0012 airfoil in hover at Re = $O(10^3)$ experimentally and numerically. A 2-D computation was compared to a pitching and plunging airfoil in a water tank. They found that the more energetic vortices, which were the most influential flow features on the resulting forces, were visible.

Hong and Altman [Hong and Altman (2007, 2008)] investigated experimentally the lift generation from spanwise flow associated with a simple flapping wing at Re between O(10^3) and O(10^4). The results suggested that the presence of streamwise vorticity in the vicinity of the wing tip contributed to the lift on a thin flat plate flapping with zero pitching angle in quiescent air. Isaac *et al.* (2008) used both experimental and numerical methods to investigate the unsteady flow features of a flapping wing at Re between O(10^2) and O(10^3). They showed a feasible application of the water treading kinematics for hovering using insect/bird like cambered wings.

1.2.3 Tandem Wings in Forward/Hovering Flight Conditions

Aerodynamics associated with dragonflies differs from other two-winged insects because forewing and hindwing interactions generate distinct flow features [Azuma (2006)]. Sun and Lan (2004) studied the lift requirements for a hovering dragonfly using a 3-D NS solver with overset grid methods. They showed that the interaction between the two wings was not strong and reduced the lift compared to single wing configuration, however it was large enough to stay aloft. Yamamoto and Isogai (2005) conducted a study on the aerodynamics of a hovering dragonfly using a mechanical flapping apparatus with a tandem wing configuration and compared the time history of forces obtained from a 3-D NS solver. The force comparison showed a good agreement and the results suggested that the phase difference between the flapping motions of the fore- and hind-wings only had a small influence on the time averaged forces.

Lehmann (2009) and Maybury and Lehmann (2004) investigated the effect of changing the fore- and hindwing stroke-phase relationship in hover on the aerodynamic performance of each flapping wing by using a dynamically scaled electromechanical insect wing model at Re of $O(10^2)$. They measured the aerodynamic forces generated by the wings and visualized flow fields around the wings using PIV. Their results showed that wing phasing determined both mean force production and power expenditures for flight, in particular, hindwing lift production might be varied by a factor of two due to LEV destruction and changes in the strength and the orientation of the local flow vector. Lu *et al.* (2007) showed physical images revealing the flow structures, their evolution, and their interactions during dragonfly hovering using an electromechanical model in water based on the dye flow visualization. Their results showed a delayed development of the LEV in the translational motion of the wing. Furthermore, in most cases, forewing-hindwing interactions were detrimental to the LEVs and were weakened with increase of the wing-root spacing. For a dragonfly in forward flight, the conclusions from Wang and Sun (2005) were similar in that the forewing-hindwing interaction was detrimental for the lift, but sufficient to support its weight. They suggested that the downward induced velocity from each wing would decrease the lift on other wings.

Dong and Liang (2010) modeled dragonfly in slow flight by varying the phase difference between the forewing and hindwing and investigated the changes of aerodynamic performance of hindwings. They found that the performance of

forewings is not affected by the existence of hindwings; however, hindwings have obvious thrust enhancement and lift reduction due to the existence of forewings. For slow flight, by decreasing the phase angle difference, hindwings will have larger thrust production, slight reduction of lift production, and larger oscillation of force production. Independently, Warkentin and DeLaurier (2007) did a series of wind-tunnel tests on an ornithopter configuration consisting of two sets of symmetrically flapping wings of batten-stiffened membrane structures, located one behind the other in tandem. It was discovered that the tandem arrangement can give thrust and efficiency increases over a single set of flapping wings for certain relative phase angles and longitudinal spacing between the wing sets. In particular, close spacing on the order of 1 chord length is generally best, and phase angles of approximately 0 +/- 50 deg give the highest thrusts and propulsive efficiencies. Again, referring to other reported studies involving rigid and flexible wings, the aerodynamics and aeroelasticity associated with wing-wing interactions need to be further studied. In another study, Broering *et al.* (2010) numerically studied the aerodynamics of two flapping airfoils in tandem configuration in forward flight at a Reynolds number of $O(10^4)$. The relationship between the phase angle and force production was studied over a range of Strouhal numbers and three different phase angles, 0, 90 and 180 degrees. In general, they found that the lift, thrust and resultant force of the forewing increased compared to those of the single wing. The lift and resultant force of the hindwing was decreased, while the thrust was increased for the 0 phase hindwing

and decreased for the 90 and 180 phase hindwings. The lift, thrust and resultant force of the combined fore and hindwings was also compared to the case of two isolated single wings. In general, the 0 phase case did not noticeably change the magnitude of the resultant force, but it inclined the resultant forward due to the decreased lift and increased thrust. The 90 and 180 phase cases significantly decreased the resultant force as well as the lift and thrust. Clearly, more work is needed to help unify our understanding of the wing-wing interactions as a function of the individual and relative kinematics and dimensionless flow and structure parameters.

Wang and Russell (2007) investigated the role of phase lag between the forewing and the hindwing further by filming a tethered dragonfly and computing the aerodynamic forces and power. They found that the out-of-phase motion in hovering uses almost minimal power to generate sufficient lift to stay aloft and the in-phase motion produce additional force to accelerate in takeoffs. Young *et al.* (2008) investigated aerodynamics of the flapping hindwing of the Aeschana juncea dragonfly using 3-D computations at Re between $O(10^2)$ to $O(10^4)$. The flapping amplitude observed, 34.5°, for the dragonfly maximized the ratio of mean vertical force produced to power required. Zhang and Lu (2009) studied a dragonfly gliding and asserted that the forewing-hindwing interaction improved the aerodynamic performance for Re= $O(10^2) – O(10^3)$.

1.2.4 Implications of Wing Geometry

Lentink and Gerritsma (2003) considered different airfoil shapes numerically to investigate the role of shapes in forward flight on the aerodynamic performance. They computed flow around plunging airfoils at Re of $O(10^2)$ and concluded that the thin airfoil with aft camber outperformed other airfoils including the more conventional airfoil shapes with thick and blunt leading edges. One exception was the plunging N0010 which due to its highest frontal area had good performance. Usherwood and Ellington (2002a) examined experimentally the effect of detailed shapes of a revolving wing with planform based on hawkmoth wings at Re $O(10^3)$. The results showed that detailed leading edge shapes, twist, and camber did not have substantial influence on the aerodynamic performance. In a companion paper Usherwood and Ellington (2002b) examined experimentally the effect of aspect ratio of a revolving wing with the same hawkmoth planform [(2002a)] adjusted to aspect ratios ranging from 4.53 to 15.84 with corresponding Re $O(10^3)$ to $O(10^4)$. The results showed that the influence of the aspect ratio was relatively minor, especially at angle of attack below 50°. Luo and Sun (2005) investigated numerically the effects of corrugation and wing planform (shape and aspect ratio) on the aerodynamic force production of model insect wings in sweeping motion at Re $O(10^2)$ and $O(10^3)$ at angle of attack of 40°. The results showed that the variation of the wing shape almost unaffected the force generation and the effect of aspect ratio was also remarkably small. Moreover, the effects of corrugated wing sections in forward

flight were studied in numerical simulations [Vargas *et al.* (2008), Kim *et al.* (2009)] and a numerical-experimental approach [Levy and Seifert (2009)]. The results demonstrated that the pleated airfoil produced comparable and at times higher lift than the profiled airfoil, with a drag comparable to that of its profiled counterpart [Vargas *et al.* (2008)].

Altshuler *et al.* (2004) tested experimentally the effect of wing shape (i.e. with sharpened leading edges and with substantial camber) of a revolving wing at Re between $O(10^3)$ and $O(10^4)$. Their results demonstrated that lift tended to increase as wing models become more realistic, as did the lift-to-drag ratios. Ansari *et al.* (2008) used an inviscid model for hovering flapping wings to show that increasing the aspect ratio, wing length, and wing area enhances lift. Furthermore, they suggested that for a flapping wing MAV, the best design configuration would have high aspect ratio, straight leading edge, and large wing area outboard. The pitching axis would then be located near the center of the area in the chordwise direction to provide the best compromise for shedding vortices from the leading and trailing edges during the stroke reversal. Green and Smith (2008) examined experimentally the effect of aspect ratio and pitching amplitude of a pitching flat plate in forward flight at Re between $O(10^3)$ and $O(10^4)$ and aspect ratios of 0.54 and 2.25. They measured unsteady pressure distributions on the wing, and compared to the PIV measurements of the same setup [Buchholzand Smits (2008)]. They concluded that the 3-D effects increased with decreasing aspect ratio, or when the pitching amplitude increased.

Kang *et al.* (2009) investigated the airfoil shape effect at Re = $O(10^4)$ by comparing the flow field around pitching and plunging SD7003 airfoil and flat plate using PIV [Baik *et al.* 2009], and CFD in forward flight. It was observed that for the flat plate the flow was not able to turn around the sharper leading edge of the flat plate and eventually separated at all phases of motion. The flow separation led to larger vortical structures on the suction side of the flat plate hence increasing the area of lower pressure distribution on the flat plate surface. From the time history of lift, available for the CFD, it was seen that for the flat plate these vortical structures increased the lift generation compared to the SD7003 which had a blunter leading edge.

1.2.5 Implications of Wing Kinematics

A primary driver of the unsteady aerodynamics in flapping wing flight is the wing motions. Yates (1985) suggested that the choice of the position of the pitching axis may enhance performance and control of rapid maneuvers and thus enable the organism to cope more adeptly with turbulent environmental conditions, to avoid danger, or to more easily capture food. The instantaneous fluid forces, torques, and rate of work done by the propulsive appendages were computed using 2-D unsteady aerodynamic theories. For a prescribed motion in forward flight, the moment and power were further analyzed to find the axes, for which the mean square moment was minimal, the mean power to maintain the moment was zero, the mean square power to maintain moment was a minimum, and the mean square power to maintain lift equaled the mean square power. Sane

and Dickinson (2002) investigated the effect of location of pitching axis on force generation of the flapping fruit fly-like wing in the first stroke using a scaled-up robotic wing model. They estimated the rotational forces based on the quasi-steady treatment and blade element theory. The results showed that rotational forces decrease uniformly as the axis of rotation moves from the leading edge towards the trailing edge and change sign at approximately three-fourths of a chord length from the leading edge of the wing [Dickinson *et al.* (1999)].

Ansari *et al.* (2008) studied the effects of wing kinematics on the aerodynamic performances of insect-like flapping wings in hover based on non-linear unsteady aerodynamic models. They found that the lift and the drag increased with increasing flapping frequency, stroke amplitude, and advanced wing rotation. However, such increases were limited by practical considerations. Furthermore, the authors mentioned that variations in wing kinematics were more difficult to implement mechanically than variations in wing planform. Hsieh *et al.* (2009) investigated the aerodynamics associated with the advanced, delayed, and symmetric rotation and decomposed the lift coefficients in terms of the lift caused by vorticity, wing velocity, and wing acceleration. The results suggested that while the symmetric rotation had the most lift due to vorticity on the surface of the wing and in the flow, the maximum total lift is found with advanced rotation. Oyama *et al.* (2009) optimized for the mean lift, mean drag, and mean required power generated by a pitching/plunging NACA0012 airfoil in forward flight using a 2-D NS solver at Re = $O(10^3)$. The multi-objective evolutionary algorithm was

used to find the pareto front of the objective functions (i.e. by considering the reduced frequency, plunge amplitude, pitch amplitude, pitch offset, and phase shift as the design variables). They found that the pitching angle amplitude (between 35 and 45 degrees) was optimum for high performance flapping motion and a phase angle between pitch and plunge of about 90 degrees. In addition, the reduced frequency was a tradeoff parameter between minimization of required power and maximization of lift or thrust where smaller frequency leads to smaller required power.

1.2.6 Reynolds Number Effects

The Reynolds number dictates the trade-off between the inertial and viscous forces. This balance has a significant impact on the vortex activity. As discussed previously, the lift enhancement due to the delayed stall of the LEV is important in flapping wing flight [Shyy *et al.* (2008), Dickinson *et al.* (1999), Ellington *et al.* (1996)]. The formation of the LEV depends on the wing kinematics, the details of wing geometry, and the Reynolds number [Shyy *et al.* (2007, 2008, 2010), Liu & Aono (2009), Birch *et al.* (2001), and Liu (2009)].

Liu & Aono (2009) investigated the interaction between LEV, TiV and vortex ring structures. Tang *et al.* (2008) investigated numerically the effects of Reynolds number on 2-D hovering airfoil aerodynamics at Re $O(10^1)$ to $O(10^3)$. They showed that in low Reynolds number regimes, $O(10^2)$, the viscosity dissipated the vortex structures quickly and led to essentially symmetric flow

structures and aerodynamic forces between the forward and backward stroke while at higher Reynolds numbers, the history effect was influential, resulting in distinctly asymmetric phenomena between strokes. In order to examine the Re effect on LEV structures and spanwise flow for realistic wing body configurations with appropriate kinematic motions, a numerical investigation was done by Liu & Aono (2009). Realistic models of a hawkmoth ($Re = 6.3\times10^3$, k= 0.30), honeybee ($Re = 1.1\times10^3$, k= 0.24), fruitfly ($Re = 1.3\times10^2$, k= 0.21), and thrips ($Re = 1.2\times10^1$, k= 0.25) in hover considering different representative kinematic parameters (flap amplitude, flap frequency, and type of prescribed actuation) and dimensionless numbers (Reynolds number, reduced frequency) in each case. The higher Re cases created stronger LEV, but the lower Re cases kept the feature attached to the wing surface longer. To illustrate the Reynolds number effect, ceteris paribus, numerical results were obtained for a single wing-body geometry and kinematics combination [Shyy & Liu (2007)]. Qualitatively similar flow structures around the flyer were observed, but it was implied that the Reynolds number was one of the dominant parameters in dictating the LEV structure.

Kang *et al.* (2009a,b) carried out turbulent Navier-Stokes simulations complementing experimental PIV studies of a pitching and plunging wing in forward flight conditions at Re $O(10^4)$. They saw significant qualitative differences in the fluid physics experienced during the pitching and plunging motions of the SD7003 airfoil between the lower end of the Re spectrum studied and the higher end. This difference was driven by the large flow separation at Re

~$1x10^4$ whereas the flow at Re > $3x10^4$ was largely attached. The pure plunging case, which was meant to elicit deep stall, saw separation at all Re with the main difference being whether or not the flow would be able to reattach. It was able to for cases Re > $1x10^4$. The flatplate was much less sensitive to the Re due to the fact that the flow separation dominated the fluid physics. They also found Theodorson's (1935) theory applicable despite the large separation regions experienced in their studies.

1.2.7 Wing Flexibility and Aerodynamic Consequences

While the content of the original work documented in this thesis focuses exclusively on rigid wing aerodynamics, natural flyers will have some degree of flexibility in their wings. Some animals, like bats, have a membrane wing that is predominantly flexible and the fluid-structure interactions become tightly interdependent. The consequences of aeroelasticity in flapping wings is actively being studied, but a full picture of aeroelastic impact is still not clear. Selected studies from the literature are highlighted below to illustrate the potential for manipulating the aerodynamic response.

Analytical investigations by Daniel and Combes (2002) suggested that aerodynamic loads were relatively unimportant in determining the bending patterns in oscillating wings. Subsequently, experimental investigations by Combes (2002) and Combes and Daniel (2003a) found that the overall bending patterns of a Hawkmoth wing were quite similar when flapped (single degree-of-

freedom flap rotation) in air and helium, despite a 85% reduction in fluid density in the latter, suggesting that the contribution of aerodynamic forces was relatively small compared to the contribution of inertial-elastic forces doing flapping motion. However, they mentioned that realistic wing kinematics might include rapid rotation at the stroke reversal that may lead to increased aerodynamic forces due to unsteady aerodynamic mechanisms. Furthermore, static bending tests by Combes and Daniel (2003b,c) showed anisotropy of wing structures in a variety of insect species. More recently, Mountcastle and Daniel (2009) investigated the influence of wing compliance on the mean advective flows (indicative of induced flow velocity) using PIV techniques. Their results demonstrated that flexible wings yield mean advective flows with substantially greater magnitudes and orientations more beneficial to lift than those of stiff wings.

Vanella *et al.* (2009) conducted numerical investigations on a similar structure found that the best performance (up to approximately 30% increase in lift) was realized when the wing was excited by a non-linear resonance at 1/3rd of its natural frequency. For all Reynolds numbers considered, the wake capture mechanism was enhanced due to a stronger flow around the wing at stroke reversal, resulting from a stronger vortex at the trailing edge. Heathcote *et al.* (2004) investigated the effect of chordwise flexibility on aerodynamic performance of an airfoil in pure plunge under hovering conditions. Because the trailing edge was a major source of shedding of vorticity at zero freestream velocity, they showed that the amplitude and phase angle of the motion of the

trailing edge affected the strength and spacing of the vortices, and the time averaged velocity of the induced jet. Direct force measurements confirmed that at high plunge frequencies, the thrust coefficient of the airfoil with intermediate stiffness was highest, although the least stiff airfoil can generate larger thrust at low frequencies. It was suggested that there was an optimum airfoil stiffness for a given plunge frequency and amplitude. Similar conclusions were made in another study [Michelin & Smith (2009)], wherein the influence of resonance on the performance of a chordwise flexible airfoil prescribed with pure plunge motion at its leading edge was studied. It was shown that while the mean thrust could increase with an increase in flexibility, below a certain threshold the wing is too flexible to communicate momentum to the flow. On the other hand, too much flexibility led to a net drag and hence, only a suitable amount of flexibility was desirable for thrust generation.

Du and Sun (2008) numerically investigated the effect of prescribed time-varying twist and chordwise deformation on the aerodynamic force production of a fruitfly in hover. The results showed that aerodynamic forces on the flapping wing were not affected much by the twist, but by the camber deformation. The effect of combined camber and twist deformation was found to be similar to that of camber deformation alone. With a deformation of 6% camber and 20° twist (typical values observed for wings of many insects), the lift increased by 10% - 20% compared to the case of a rigid flat plate wing. It was therefore shown that

chordwise deformation could increase the maximum lift coefficient of a fruit fly wing model and reduce its power requirement for flight.

While most of the recent computational and experimental studies explored the role of wing flexibility in augmenting aerodynamic performance while focusing on single wings at relatively higher Reynolds numbers, Miller and Peskin (2009) numerically investigated the effect of wing flexibility on the forces produced during clap and fling/peel motion [Ellington (1984)] of a small insect (Re ≈ 10) focusing on wing-wing interactions. They prescribed both clap and fling kinematics separately to a rigid and a chordwise flexible wing and showed that while lift coefficients produced during the rigid and flexible clap strokes were comparable, the peak lift forces in the flexible cases were higher than in the corresponding rigid cases. This was due to the peel motion which delayed the formation of the trailing edge vortices, thereby maintaining vortical asymmetry and augmenting lift for longer periods.

Hui *et al.* (2009) examined various flexible wing structures to evaluate their implications on flapping wing aerodynamics. They showed that the flexible membrane wings were found to have better overall aerodynamic performance (i.e., lift-to-drag ratio) over the rigid wing for soaring flight, especially for high speed soaring flight or at relatively high angle of attack. The rigid wing was found to have better lift production performance for flapping flight in general. The latex wing, which was the most flexible among the three tested wings, was found to

have the best thrust generation performance for flapping flight. The less flexible nylon wing, which has the best overall aerodynamic performance for soaring flight, was found to be the worst for flapping flight applications. Shkarayev *et al.* (2010) investigated the aerodynamics of cambered membrane flapping wings. Specifically, a cambered airfoil was introduced into the wing by shaping metal ribs attached to the membrane skin of the 25 cm-wing-span model. The thrust force generated by a 9% camber wing was found to be 30% higher than that of the same size flat wing. Adding a dihedral angle to the wings and keeping the flapping amplitude constant improved the cambered wing's performance even further.

Kim *et al.* (2009) developed a biomimetic flexible flapping wing using micro-fiber composite actuators and experimentally investigated the aerodynamic performance of the wing under flapping and non-flapping motion in a wind tunnel. Results showed that the camber due to wing flexibility could produce positive effects (i.e. stall delay, drag reduction, and stabilization of the LEV) on flapping wing aerodynamics in quasi-steady and unsteady region. Mueller et al. (2009) presented a new versatile experimental test for measuring the thrust and lift of a flapping wing MAV. They showed increase in average thrust due to increased wing compliance and detrimental influence of excessive compliance on drag forces during high frequency operation. Also they observed the useful effect of compliance on the generation of extra thrust at the beginning and end of flapping motions.

Hamamoto *et al.* (2007) conducted a fluid-structure interaction analysis on a deformable dragonfly wing in hover and examined the advantages and disadvantages of flexibility. They tested three types of flapping flight: a flexible wing driven by dragonfly flapping motion, a rigid wing (stiffened version of the original flexible dragonfly wing) driven by dragonfly flapping motion, and a rigid wing driven by modified flapping based on tip motion of the flexible wing. They found that the flexible wing, with nearly the same average energy consumption, generated almost the same amount of lift force as the rigid wing with modified flapping motion, which realized the same angle of attack at the aerodynamically dominant sections of the wing. However, the rigid wing required 19% more peak torque and 34% more peak power, indicating the usefulness of wing flexibility. Aono *et al.* (2010) reported a combined computational and experimental study of a flapping wing structure. An aluminum wing was prescribed with single degree-of-freedom flapping at 10 Hz frequency and ±21º amplitude. Flow velocities and deformation were measured using digital image correlation and digital PIV techniques, respectively. In the most flexible flapping wing case, the elastic twisting of the wing was shown to produce substantially larger mean and instantaneous thrust due to shape deformation-induced changes in effective angle of attack. Relevant fluid physics were documented including the counter-rotating vortices at the leading and the trailing edge which interacted with the tip vortex during the wing motion.

Agrawal and Agrawal (2009) investigated the benefits of insect wing flexibility on flapping wing aerodynamics based on experiments and numerical simulations. They compared the performance of two synthetic wings: (i) a flexible wing based on a bio-inspired design of the hawkmoth (Manduca Sexta) wing and (ii) a rigid wing of similar geometry. The results demonstrated that more thrust was generated by the bio-inspired flexible wing compared to the rigid wing in all wing kinematic patterns considered. They emphasized that the results provided motivation for exploring the advantages of passive deformation through wing flexibility and that coupled fluid-structure simulations of flexible flapping wings were required to gain a fundamental understanding of the physics and to guide optimal flapping wing MAV designs.

As summarized in Shyy *et al.* (2010), it seems like the spanwise flexibility increases aerodynamic forces by creating higher effective angles of attack via spanwise deformation. However, apart from affecting the overall aerodynamic force generation, the chordwise flexibility can redistribute lift versus thrust by changing the angle of the wing with respect to the freestream or the camber of the wing itself. Overall, an understanding of the structural response and its interplay with the unsteady aerodynamics has the potential to exceed rigid wing performance in the context of flapping wing flight. Optimizing the process of assigning the material properties of the wing based off their impact on the unsteady flight mechanisms, and thus performance, is still an open area of research.

1.2.8 Reduced Order Models

Before the advent of readily available computational resources and the methods to utilize them, researchers had to rely on combinations of empirical data and analytical models. These methods find use today as they have the potential to provide insight as the governing equations are modified and/or simplified, and as a quick estimate to be used in a design tool for which on-demand Navier-Stokes solutions are too computationally expensive or unrealistic.

One approach used in flapping wing aerodynamics are variations of quasi-steady theories. Flapping wing movements inherently have a time-dependent nature to them; what quasi-steady theory does is to assume the solution is instantaneously steady-state and that equivalent forces are felt for a wing with the same velocity and angle of attack. One of the strengths is having an analytical solution which is ideal in terms of computational expense. Theodorsen (1935) and Osborne (1951) modified the blade-element theory of Drzewiecki for flapping flight applications. While Jensen (1956) saw promise when applying the principles to tethered locusts, Cloupeau *et al.* (1979) showed that the forces felt by the tethered locust were in clear excess of those predicted by quasi-steady theory. Ellington (1984) found the validity of applying quasi-steady theory to flapping wing applications ambiguous. Dudley and Ellington (1990) showed that the fast forward flight of bumblebees was incompatible with quasi-steady

aerodynamics. Sane and Dickinson (2002) made further modifications and found that quasi-steady theory could meaningfully approximate lift and drag values away from the wake-capture region. Because the models they built did not include this time history effect they were able to show how much of an impact wake-capture had on the force history which could be quite significant. Kang *et al.* (2009a), as discussed above in section 1.2.6, found applicability in quasi-steady models for forward flight conditions at Re $O(10^4)$ despite large regions of separated flow. The applicability of such models would appear to be highly context dependent.

Another approach being adopted is numerical in nature, but significantly less expensive than solving the Navier-Stokes equations. This branch of investigations is based of inviscid theory and vortex-lattice methods [Anderson (2006)]. Modifications to the classical theory have been made to allow for the moving boundary and the shedding of vortices from the leading edge in addition to the trailing edge. Gogulapati *et al.* (2008, 2010) showed promising results in hovering and forward flight conditions for rigid and flexible wings capturing the overall trends in the force histories for the cases studied and in some situations closely approximating the instantaneous forces quite closely.

This thesis aims to 1) explore and illuminate the relevant fluid physics in flapping wing flight as a function of kinematic wing motions 2) provide a method

for quickly and accurately predicting the aerodynamic performance in such a way to be potentially useful for control algorithm implementation.

In regard to point 1, some influences are well documented, e.g. the LEV. Its role is examined as function of the kinematic motions, and in concert with the literature is found to be a dominant lift enhancing mechanism at Re = 100. Other phenomena are recognized but not well documented in the flapping wing community. The tip vortices found in steady state aerodynamic theory are sources of performance penalties. It is shown that certain kinematic motions in flapping wing flight can utilize these tip vortices as a lift enhancement mechanism which departs from the behavior expressed by the steady state theories. Another phenomena examined in the following work is the downward jet, which was observed to exist experimentally, but whose impact was otherwise entirely ignored. This is work examines the impact on the aerodynamic loading when the downward jet is present.

The fluid physics exploration used a combination of CFD simulations of the Navier-Stokes equations and relevant to point 2, a computationally cheap reduced order model. To be addressed in the following chapter is the reduced order model technique employed in the current studies, surrogate models. These need to be trained, e.g. from experimental data or computational simulations, but then offer predictions at some combination of variables away from the training data and can be used in a variety of ways to probe the desired phenomena.

Chapter 2 Approach and Methods

Due to the complexity of the aerodynamics associated with bio-mimicking kinematics, building a description of the fundamental factors involved can benefit from simplified models. As previously addressed, the aerodynamics associated with flapping wing flight during hover can be dominated by the interactions between the wing and generated vortices and these interactions can make it difficult for approximate models to correctly predict quantities of interest. To capture the appropriate phenomena, solutions to the full governing equations are solved. This takes the form of computational fluid dynamics simulations (CFD) that numerically solve the Navier-Stokes equations. From a vehicle development perspective, since 3D Navier-Stokes simulations are expensive to generate, if 2D simplifications or other approximations can adequately reproduce the main aerodynamic features of 3D flapping wing, then the needed data can be generated much more economically. The simplified models in this study are surrogate modeling tools that are used in a complementary fashion to systematically examine the design space while linking the instantaneous force histories and fluid physics from the Navier-Stokes solutions to the general trends in performance as kinematic variables are varied.

2.1 CFD Modeling

The governing equations are the laminar, unsteady, Navier-Stokes equations with constant density and transport properties; the incompressible versions are shown in Eqs. (1) and (2) written in indicial form.

$$\frac{\partial}{\partial x_j}(u_j) = 0 \tag{3}$$

$$\frac{\partial}{\partial t}(u_i) + \frac{\partial}{\partial x_j}(u_j u_i) = -\frac{1}{\rho}\frac{\partial p}{\partial x_i} + \nu \frac{\partial}{\partial x_j}\left(\frac{\partial u_i}{\partial x_j}\right) \tag{4}$$

Here u_i is the velocity vector, x_i is the Cartesian position vector, t is time, ρ is the density of the fluid, p is the pressure, and ν is the kinematic viscosity of the fluid. Even during the solution of identical equations, the numerical methods employed can have implications on the stability and accuracy of the solution. Two codes with vastly different methodologies are used in this study, Loci-STREAM and FDL3DI and are briefly discussed below.

A rule-based software (see Luke and George 2005), Loci-STREAM (see Kamakoti et al. 2006) is used to calculate the solutions. Loci-STREAM is a three-dimensional, unstructured, pressure based finite volume solver. The present calculations use implicit first or second order time stepping (the first order technique is adopted in this study). The convection terms are treated using the second order upwind scheme (see Shyy 1985; Shyy 1994) while pressure and viscous terms are treated using second order schemes. The system of equations resulting from the linearized momentum equations are fast to converge (see Shyy

1994) and are handled with the symmetric Gauss-Seidel (see Blazek 2001) solver which has relatively low memory requirements. The pressure equation (see Kamakoti et al. 2006; Thakur and Wright 2005) is slower to converge, and is handled by the PETSc Krylov (see Blazek 2001) solvers with Jacobi preconditioning. The Loci framework is by design highly parallelizable and can take advantage of many processors.

The FDL3DI code is a higher order finite difference solver. It uses a density based formulation. Numerical instabilities associated with the higher order methodology are handled with the use of high order filtering techniques. These serve to selectively address the high frequency oscillations encountered and thus stabilize the solution while maintaining high fidelity solutions. FDL3DI is also parallel. For further discussion the reader is referred to Visbal and Gaitonde (1999 and 2002).

While the combination of pitching and translation (versus flapping about a pivot point) of the entire wing are not found in a biological flyer, the motions used provide a basis for more complex analysis and are feasible mechanical designs. The translational and rotational airfoil/grid motions are defined as Eqs. (5) and (6).

$$h(t) = h_a \sin(2\pi f t) \tag{5}$$

$$\alpha(t) = \alpha_0 - \alpha_a \sin(2\pi f t + \phi) \tag{6}$$

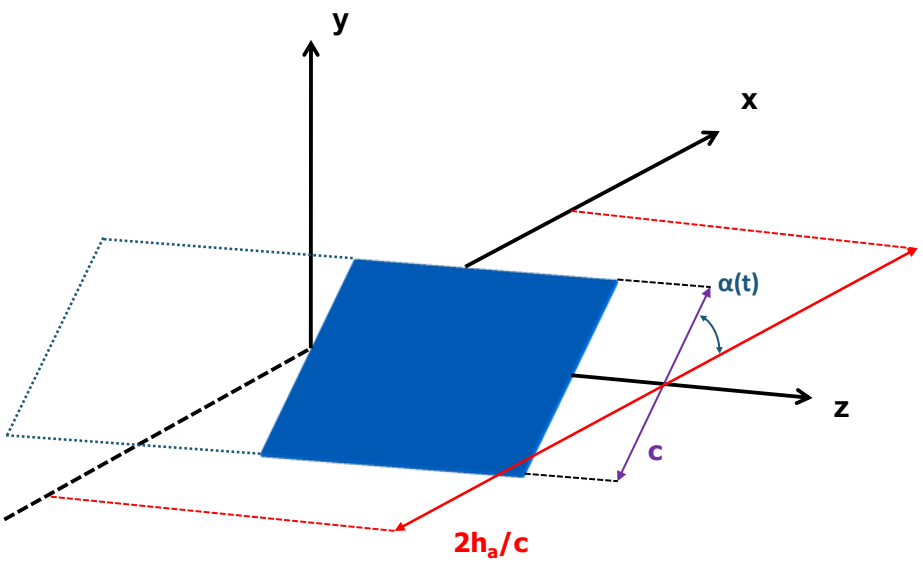

Figure 6. Illustration of the kinematic parameters for normal hovering.

Here *h(t)* and h_a are the dimensional translational position and plunging amplitude respectively. The angular orientation, time-averaged angle, and angular amplitude are $\alpha(t)$, α_0, and α_a respectively, see Fig. 6. The pitching is about the center of the rigid airfoil; the airfoil is a rectangular flat plate with 2% thickness and aspect ratio of 4 for all cases under consideration unless otherwise specified. The phase lag between the two motions is ϕ, and the motion frequency is denoted *f* whereas the time is again *t*. While there are a few choices in how to accommodate these kinematics computationally, the current implementation forces the grid to rotate and translate with the airfoil rigidly. The geometric conservation law (GCL) (see Thomas and Lombard 1978), a necessary consideration in domains with moving boundaries, is satisfied (see Kamakoti and Shyy 2004). The three quantities h_a, α_a, and ϕ can be varied independently.

Due to the kinematic constraints there are only two relevant non-dimensional groups in the incompressible case. The plunging amplitude to chord ratio, $2h_a/c$, and the Reynolds number:

$$Re = \frac{U_{ref} L_{ref}}{\nu} = \frac{(2\pi f h_a)c}{\nu} \tag{7}$$

The reference velocity (U_{ref}) in this case is the maximum translational velocity, defined by the flapping frequency, f, and the plunging amplitude, h_a. Since Re is being held constant, h_a and f are not independent. Note that the reduced frequency, k, is not emphasized here as, in the absence of a freestream, it contains the same information as the plunging amplitude ratio whereas if U_{ref} is instead set equal to zero the reduced frequency is always infinite.

$$k_{hovering} = \frac{2\pi L_{ref}}{2U_{ref}} = \frac{2\pi f c}{2(2\pi f h_a)} = \frac{c}{2h_a} \tag{8}$$

Figure 7 shows the grid distribution near the flat plate, and the applied boundary conditions over the computational domain. The thickness of the flat plate is 0.02c, and the flat plate is rectangular, i.e. there is no variation in spanwise direction (z-axis). The half-span length from the symmetry plane to the wingtip is 2c, the leading, and trailing edges are rounded using a half circular shape, while the wingtip is flat. The outer boundary is located at 25c away from the flat plate, and the outer boundary plane opposite to the symmetry plane at 15c.

At all non-symmetry plane outer boundaries, inlet conditions with zero velocity conditions are imposed.

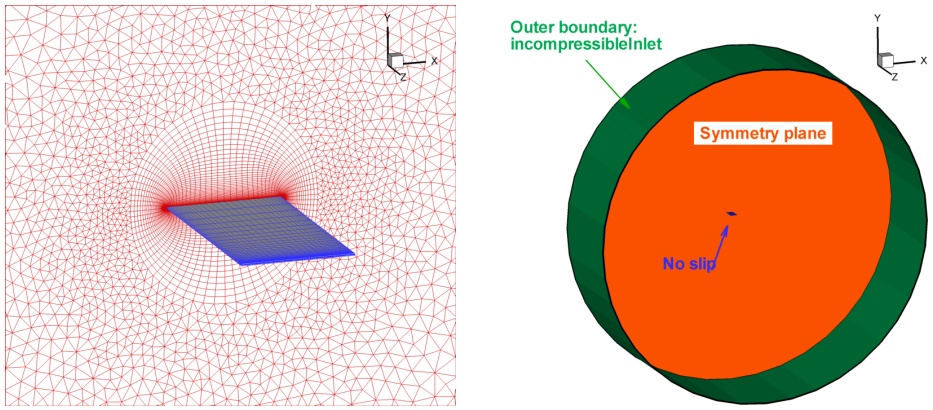

Figure 7. (Left) : Grid distribution on the flat plate, and on the symmetry plane. (Right): Boundary conditions assigned on the computational domain. The outer boundary plane opposite to the symmetry plane has not been shown due to visibility and also has the incompressibleInlet boundary condition.

The two-dimensional surrogate modeling cases use a 2% thick flat plate while the three-dimensional cases use a 2% thick flat plate with an AR=4. Grid and temporal sensitivity studies are shown in Trizila *et al.* (2008a,b). Furthermore, to maintain consistency of grid system, the grid of the symmetry plane in the three-dimensional flat plate was used as the computational domain of the two-dimensional cases. Due to the difficulties in performing experiments and obtaining data at Re O(100), a cross-comparison exercise was done between the two codes. Figure 8 shows the resulting force history after grid and temporal sensitivity studies were performed and the consistency leads to confidence that the simulations are being modeled properly. Remember that the numerical

methods involved are very different and any error or inconsistency in methodology in one would be hard to reproduce in the other framework.

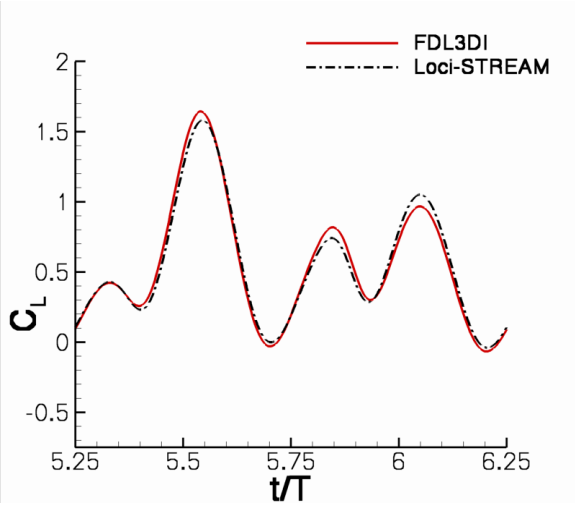

Figure 8. Cross-validation of Loci-Stream and FDL3DI for a two-dimensional ellipse with 15% thickness during normal hovering computation with for Re = 100, $2h_a/c = 3.0$, $\alpha a = 45°$, $\varphi = 90°$.

2.2 Surrogate Modeling

The motivation behind surrogate models is to replace costly objective function evaluations, a quantity of interest such as time averaged lift obtained via detailed CFD solutions or substantial experimental setups, with inexpensive approximations of sufficient fidelity. Overview of surrogate modeling techniques and selected applications can be found in reference Queipo et al. (2005) and is illustrated in Fig. 9. The process starts with choosing number and locations of training points in the "design space" (here meaning the three-dimensional space encompassing the three kinematic parameters); this is known as constructing the

design of experiment (DOE). Once the training points are chosen, the objective functions must be evaluated; depending on the context this can be done computationally, analytically, and/or experimentally. After the objective functions have been obtained for the selected training points, the surrogate models can be built. Popular models are polynomial response surfaces (PRS) [Myers and Montgomery (2002)], Kriging [Sacks, Schiller, and Welch (1989)], radial basis neural networks (RBNN) [Cheng and Titterington (1994)], support vector regression (SVR) models [Smola and Scholkopf (2004)] and various combinations thereof. After the models are constructed, appropriate error measures can be adopted to construct a weighted average surrogate (WAS) [Goel *et al.* (2007), Viana *et al.* (2008)]. Based on the surrogate approximation, the global sensitivity evaluations can be performed to evaluate the individual and collective influence of the kinematic parameters (design variables) and to order their relative importance in determining the aerodynamic outcome.

*Note: In the following surrogate modeling sections the variable "**x**" is not used to refer to spatial dimensions, but rather the design variables; in the current studies this would be the plunging amplitude, angular amplitude, or phase lag.*

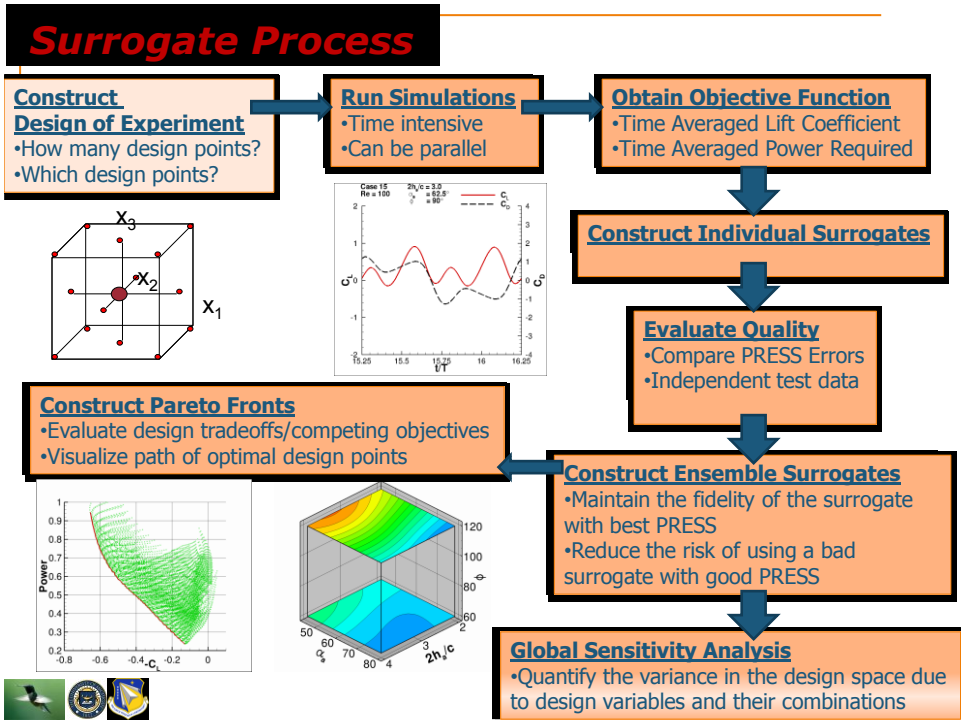

Figure 9. Outline of the surrogate process.

2.2.1 Design Space

The range of variables, see table 4, was chosen after considering the length and time scales observed in nature and compiled in Weis-Fogh (1972), Weis-Fogh (1973), and Ellington (1984), see table 5. Tabulated measurements of angular amplitudes and phase lags for a variety of species are not as forthcoming, however the comments in those references would indicate that bounds chosen are reasonable. As a first attempt, we focus on the Reynolds number of 100 under hovering conditions for which representative values have been calculated, see table 2. For the three-dimensional cases, the aspect ratio of 4 was chosen as to elicit three-dimensional flow features without completely overwhelming the fluid physics over the entire wing.

Parameter	Minimum	Maximum
$2h_a/c$	2.0	4.0
α_a	45˚	80˚
φ	60˚	120˚

Table 4. Minimum and maximum values of the plunging amplitude ratio, angular amplitude, and phase lag that were evaluated.

	c (cm)	*f(Hz)*	$2h_a/c$	$Re_{hovering}$
Fruit Fly: ***Drosophila virilis***	0.15	240	3.5	250
Honey Bee: ***Apis mellifica***	0.43	240	2.8	1900
Bumble Bee: ***Bombus terrestris***	0.73	156	2.8	4800
Hummingbird: ***Archilochus colubris***	1.5	52	3.6	6400
Hawkmoth: ***Manduca Sexta***	2.5	27.3	2.6	6700
Hummingbird: ***Patagona gigas***	4.3	15	3.6	15000

Table 5. Selected data (see Weis-Fogh 1972 and 1973) on time and length scales encountered in nature. The examples listed do not capture the upper or lower bounds of any category listed, but do provide a window within which many of the animals and insects capable of hovering flight are within. The Reynolds numbers are appropriate for hovering flight and are calculated from the wing chord, flapping frequency, and angle through which the wing moves during a stroke as measured about the pivot point.

2.2.2 Design of Experiments

The number and the efficient distribution of the training points to populate the design space is considered thoroughly in the DOE. The DOE used a face centered cubic design (FCCD) [Shyy *et al.* (2001)] and then Latin hypercube sampling (LHS) [Quiepo *et al.* (2005)] to appropriately fill in the remainder of the design space. The reasoning behind this is that a 2nd order polynomial response surface construction has (N+1)(N+2)/2 coefficients, N being the number of variables, and in general, one wants twice this many data points for an initial

curve fit which would try and reconcile the computational cost (fewer training points desired) with the resulting fidelity (more training points desired). A FCCD design provides 2^N+2N+1 points: 2^N corner points, 2N face points, and one center point. Thus for three design variables, FCCD provides 15 of the 20 points required. The LHS then provides a method for efficiently choosing the rest of the points by maximizing the distance between the added points. A tabulation of the two-dimensional and three-dimensional simulations run and their respective outcomes, as well as quantitative measures of merit for the surrogate models, are found in Trizila *et al.* (2008a).

2.2.3 Prediction Error Sum of Squares (PRESS)

PRESS is one of the quantities used to evaluate the quality of a surrogate model after it has been constructed, i.e. it is not known *a priori*. It should be emphasized that a good PRESS value (low) is not a guarantee of a good surrogate fit, but that a bad PRESS value (high) is an indication that the surrogate model does not accurately predict the training data. The idea behind PRESS is to use the training data to evaluate the quality of the surrogate. Creating surrogates is inexpensive compared to the time needed for full Navier-Stokes solutions. While data independent of the training data is needed for validation purposes these are expensive and minimized. PRESS takes the N training points and uses N-1 to create the surrogate model. The error is then calculated between the surrogate and the training point left out. This process is repeated for all N training points (there

are variations of this where every permutation is not tried if N is large, but for this study the entire surrogate process took < 5 minutes).

2.2.4 Polynomial Response Surface (PRS)

The polynomial response surface (see Myers and Montgomery 2002) is based on regression analysis. The true objective, y, is broken up into the predicted response,$\hat{y}$, which takes the form of a polynomial approximation, and the error ϵ as shown in the equation below. The error is assumed to be independent and though two points may be close, their associated errors need not be.

$$y(\boldsymbol{x}) = \hat{y}(\boldsymbol{x}) + \epsilon \tag{9}$$

For the current study a 2nd order polynomial is used and the predicted response takes the form:

$$\hat{y} = \beta_0 + \sum_{i}^{N_{DV}} \beta_i x_i + \sum_{i}^{N_{DV}} \sum_{j=1,i<j}^{N_{DV}} \beta_{ij} x_i x_j + \sum_{i}^{N_{DV}} \beta_{ii} x_i^2 \tag{10}$$

One will have an instance of the above equation for each of the N_{TP} training points. The coefficients β can be obtained by using the method of least squares. If the system of equations is written in matrix form,

$$\hat{\boldsymbol{y}} = \boldsymbol{X}\boldsymbol{\beta} \tag{11}$$

$$\boldsymbol{X} = \begin{bmatrix} 1 & x_1^{(1)1} & \cdots & x_3^{(1)2} \\ \vdots & \vdots & \ddots & \vdots \\ 1 & x_1^{(N_{TP})1} & \cdots & x_3^{(N_{TP})2} \end{bmatrix} \tag{12}$$

where $x_C^{(A)B}$ is the C design variable, raised to the B power, at the A training point. Then the matrix β can be solved as follows:

$$\boldsymbol{\beta} = (\boldsymbol{X}^T\boldsymbol{X})^{-1}\boldsymbol{X}^T\hat{\boldsymbol{y}} \tag{13}$$

2.2.5 Kriging

The Kriging (see Sacks *et al.* 1989) methodology predicts the objective function as the sum of a polynomial trend, f(**x**), and a systematic departure, Z(**x**) as expressed below.

$$\hat{y}(\boldsymbol{x}) = f(\boldsymbol{x}) + Z(\boldsymbol{x}) \tag{14}$$

The polynomial trend, usually a polynomial of degree 0,1,or 2, accounts for the low frequency general response of the objective function(s) where the systematic departure is relatively localized and catches the higher frequency variation from the trend line but also has a zero mean. Whereas the PRS models assume independent error, Kriging models are built with the assumption the errors are correlated. The Gaussian correlation structure used (see Sacks *et al.* 1989) takes the form of

$$\text{Covariance}\left(Z(\boldsymbol{x}^i), Z(\boldsymbol{x}^j)\right) = \sigma^2 \exp\left(-\sum_{k=1}^{N_{DV}} \theta_k \left(x_k^i - x_k^j\right)^2\right) \tag{15}$$

One cycles through and evaluates the k^{th} design variable x at the i^{th} and j^{th} training points. The standard deviation of the design space is denoted by σ, and θ_k is a fitting parameter measuring the degree of correlation in the k direction. Thus, given N_{TP} training points, f(**x**), σ, and θ_k, are chosen such that the likelihood function is maximized (see Sacks *et al.* 1989). As two points move closer, $(\|x_k^i - x_k^j\|) \rightarrow 0$, and the correlation function reaches a maximum. Note that at the

training points $\hat{y}(\mathbf{x})$ = y($\mathbf{x}$), and the predicted response matches that of the true response used to train the models.

2.2.6 Radial Basis Neural Network (RBNN)

Like the Kriging models, the radial basis neural networks use localized correlation functions. However, unlike Kriging, RBNN do not use a global approximation term. The predicted response at the design point x is given below. The weighting factors are denoted w_i, and response of the ith radial basis function is a_i which depends on the distance between two design points. The influence of all N_{RBF} are summed to get the total response. A popular choice for the basis function is a Gaussian correlation. The parameter b is the bias and inversely related to an input parameter that controls the spread, or radius of influence for the neurons. A spread constant, usually between 0 and 1, that is higher will cause a smoother transition between neurons' regions of influence and result in a more non-linear response. Too large a spread constant will diffuse the neurons' sensitivity, and thus a balance must be met.

$$\hat{y}(\boldsymbol{x}) = \sum_{i=1}^{N_{RBF}} w_i a_i(\boldsymbol{x}) \tag{16}$$

$$a_i = \phi_{RBF}^{(i)}(\|\boldsymbol{x} - \boldsymbol{x}^{(i)}\| b) \tag{17}$$

$$\phi_{RBF}(\eta) = e^{-\eta^2} \tag{18}$$

Neurons are added one at a time until a user specified tolerance is achieved. A tolerance that is arbitrarily low is not desirable as this may lead to over-fitting and responses which are not accurate away from the training points. Five percent of

the mean data is a common goal tolerance. The number of radial basis functions and their associated weights are solved in a "leave one out" procedure similar to that used in PRESS where parameter combinations are tested until meeting the desired tolerance. Each point is systematically left out and the models constructed, and the fitting parameters resulting in the minimum error as summed from the predicted response to the left out points determine the model used.

2.2.7 Weighted Average Surrogate Models (WAS)

Surrogate models may fit the training data well, however this does not guarantee a decent fit throughout the design space. Different weighting strategies are employed to minimize the risk of including one of these surrogates, which based on certain error measures may seem acceptable, but in reality gives bad predictions in other parts of the design space. The weighted average surrogates currently employed use constant weights, meaning that a certain surrogate will have the same importance throughout the design space. Equation (19) expresses that the (WAS) is a function of the M candidate surrogates, i.e. those with acceptable PRESS values. (Bad PRESS values = bad surrogate models, good PRESS values do NOT guarantee good surrogate models)

$$\hat{y}_{WAS} = \sum_{i=1}^{M} w_i \hat{y}_i \tag{19}$$

The method proposed by Viana et al.(2008), minimizes the least square error over the domain where w_i is the weighting vector, e_{WAS} is the error associated with the prediction of the WAS model, and the elements of **C**, c_{ij} are given as functions of

the error of the i^{th} and j^{th} surrogate models. The weights can then be solved for as shown.

$$MSE_{WAS} = \frac{1}{V}\int_V e_{WAS}^2(\boldsymbol{x})dx = w^T \boldsymbol{C} w \tag{20}$$

$$c_{ij} = \frac{1}{V}\int_v e_i(x)e_j(x)dx \tag{21}$$

$$w = \frac{\boldsymbol{C}^{-1}\mathbf{1}}{\mathbf{1}^T\boldsymbol{C}^{-1}\mathbf{1}} \tag{22}$$

The method proposed by Goel *et al.* (2007), instead uses two parameters to control the weighting strategy α_w (recommended value of 0.05) and β_w (recommended value of -1) used to control the influence of the average, e_{avg}, and the individual PRESS errors, e_i, respectively.

$$w_i^* = \left(e_i + \alpha_w e_{avg}\right)^{\beta_w};\ \alpha_w < 1, \beta_w < 0 \tag{23}$$

$$w_i = w_i^* / \sum_i w_i^* \tag{24}$$

$$e_{avg} = \sum_{i=1}^{N_{SM}} e_i / N_{SM} \tag{25}$$

2.2.8 Global Sensitivity Analysis (GSA)

The global sensitivity analysis (GSA) is in general useful for: (i) determining if a variable is particularly influential in the design space, if not perhaps the variable can be fixed and the degrees of freedom and complexity of the problem reduced; (ii) ranking the importance of the design variables; (iii) quantifying the degree of coupling between design variables. For example, is the

influence on the design space mostly an individual effort, or is there an effect caused by the interaction of variables?

Sobol's method (see Quiepo *et al.* 2005) is used for the global sensitivity evaluations. The surrogate model can be written as:

$$f(x) = f_0 + \sum_i f_i(x_i) + \sum_{i<j} f_{ij}(x_i, x_j) + \cdots \tag{26}$$

Once this decomposition has been calculated the total variance,

$$D = \int f(\boldsymbol{x})^2 d\boldsymbol{x} - f_0^2 \tag{27}$$

and partial variances, e.g.,

$$D_1 = \int f_1(\boldsymbol{x}) dx_1 dx_2 dx_3 \tag{28}$$

can be calculated. In this fashion, individual contributions, such as D_1/D, or combinations of variables, e.g., D_{12}/D, can be quantified, effectively capturing the sensitivity of the variable(s) under consideration.

Chapter 3 Hovering Aerodynamics of a Rigid Flat Plate

In this section, we use the surrogate modeling technique, utilizing the weight-averaged surrogate model [Viana *et al.* 2008, Goel *et al.* 2007] to establish the relationship between lift generated and power required as the three flapping kinematic parameters vary. The purpose is to gain a global perspective of a multi-dimensional design space and this is done by combining the detailed fluid physics and force histories from the Navier-Stokes solutions and combining it with surrogate modeling trends.

3.1 Interpreting Force Histories and Flow Features

To better understand the implications and limitations of the surrogate modeling results an example is presented of a representative normal hovering case of a two-dimensional flat plate at a Re of 100, see figure 10. In the flapping wing aerodynamics the unsteady mechanisms such as wake capturing and delayed stall have been established in the literature (see section 1.1).

The discussion following is generally applicable to the synchronized hovering cases, where phase lag $\phi = 90°$. For cases where the phase lag dictates advanced rotation ($\phi > 90°$) or delayed rotation ($\phi < 90°$), the same ideas can be extended though as the parameter suggests, the translation and rotation will be out

of phase. Since the kinematics are governed by the sinusoidal function, for any cycle X, the ends of translation will be found at the non-dimensional times t/T of (X + 0.25) and t/T of(X+ 0.75). The backstroke starts at t/T of (X + 0.25) and finishes at t/T of (X + 0.75). The following forward stroke starts at (X + 0.75) and ends at (X + 1.25). The flapping cycle can be broken up into overlapping regions defined by the unsteady mechanisms present.

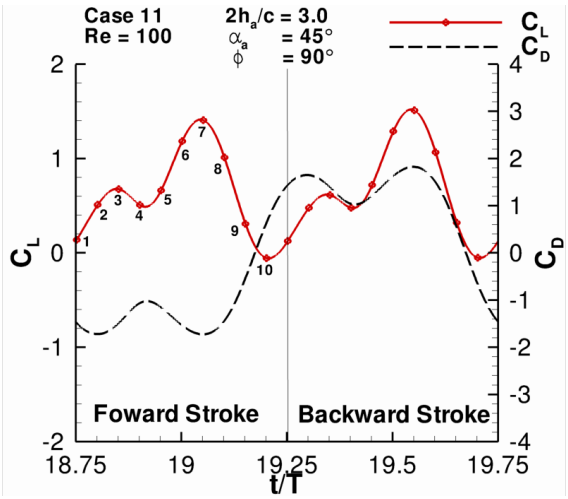

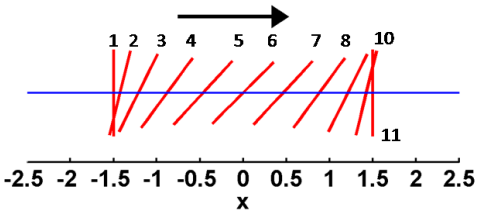

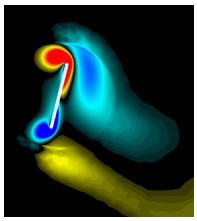

Point 2) Vorticity Contours
Wake Capturing

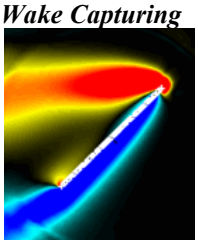

Point 6) Vorticity Contours
Delayed Stall

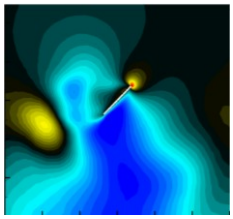

Point 6) Vertical Velocity
Jet Interaction

Figure 10. Illustration of the lift and drag coefficients for a two-dimensional ellipse normal hovering case with $2h_a/c = 3.0$, $\alpha_a = 45°$, and $\phi=90°$ and the corresponding airfoil positions. Three flowfield shots illustrating the unsteady aerodynamics are emphasized.

The first region starts at point 1 (see figure 10) which is near a local minimum in the lift. As the angle of attack of the airfoil is 90°, one would

generally expect zero lift. As time continues the airfoil turns back into its previous wake which is the well-known wake capturing, points 1, 2, and 3. The peak seen at point 3 will be referred to as the wake capturing peak.

The second unsteady mechanism is due to the angular velocity and the change in circulation about the flat plate, i.e. the Kramer effect. In the literature (see 1.1.2), one version of this is referred to as rapid pitch-up. In the present study it is seen to both aid and take away from the lift production. When $\phi = 90°$, as in the example, the maximum angular velocities are found at the ends of translation. In two-dimensional case this negative angular velocity at the start of the stroke is one of the reasons, the other is a contribution of the persistent jet interaction that degrades the lift as the flow is accelerated on the bottom of the flat plate. Depending on the kinematic parameters, this unsteady mechanism may interact with any or all of the other unsteady mechanisms.

The third and fourth unsteady flow features overlap significantly. The most commonly known is the delayed stall phenomena here resulting from a LEV at mid-stroke (see figure 10). Specifically, a vortex forms behind the leading edge of the flat plate producing a low pressure region and enhancing lift. Note that in the case illustrated, higher lift is achieved at angles of attack of 45°, an angle well beyond the steady state stall. In cases with higher angular amplitudes, and therefore lower angles of attack, the peak at points 7 and 8 can be reduced significantly because the orientation of the airfoil is not able to promote LEV

formation. The fourth unsteady feature is the persistent jet which will be discussed in detail next.

3.1.1 Impact of a Persistent Jet in 2D Hovering

Despite the fact that the specified kinematics are similar during forward and backstrokes, a substantial asymmetry can sometimes be seen in the resulting force history. This phenomenon can occur in part due to the formation of a persistent jet seen to develop as a result of a reverse Karman vortex street interacting with the downward momentum created by the wing as it translates (see figure 4). As the wing passes the jet, vortices are shed with an orientation which reinforces the downward momentum previously created by the wing. These vortices sustain the downward momentum, and further entrain surrounding fluid, as to create a flow feature which the wing then interacts with during subsequent stroke. The details in the initiation of the jet may present a slight bias serving to off-center the jet. The consequence is that during a forward stroke, the wing will encounter the jet earlier/later than during the backstroke.

The impact of the jet interaction is more influential in two-dimensional fluid dynamics. A brief study of wing startup conditions reveals that the evolution of the jet can impact the aerodynamic loading significantly.

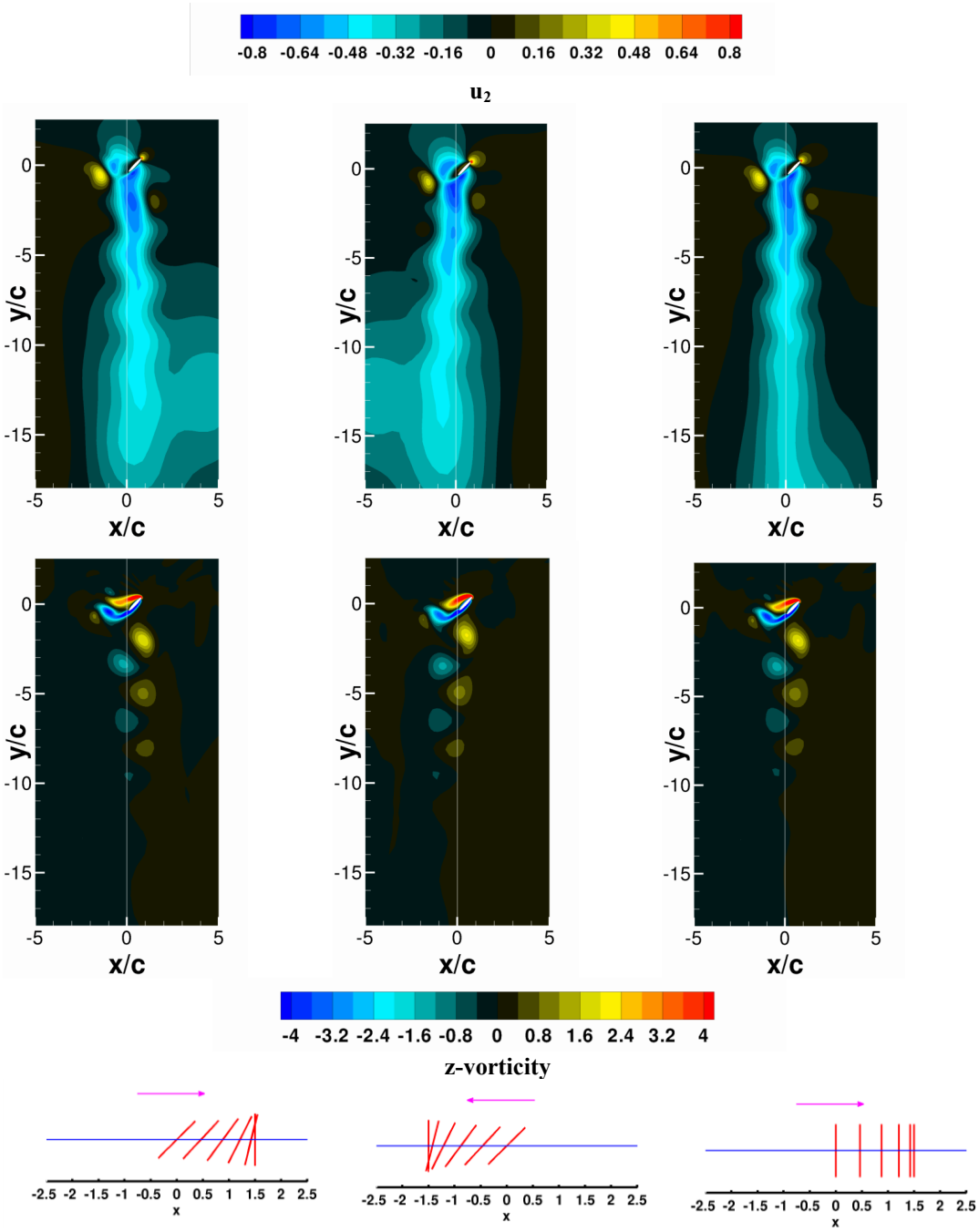

Figure 11. Vertical velocity (top) and vorticity (bottom) contours of the normal, reverse, and delay starting conditions after 25 periods for a two-dimensional case at Re=100 hovering case governed by $2h_a/c=3.0$, $\alpha_a= 45°$, $\phi=90$. The persistent jet, expressed as a blue region in the u_2 velocity plots, exhibits a slight preference to the left and right for the *normal* and *reverse* cases respectively, whereas the *delay* case is roughly centered about the mid-stroke.

Three startup conditions were evaluated. *Normal*: start the computation with the appropriate angle of attack at mid-stroke. *Reverse*: start the computation in the opposite direction with the appropriate angle of attack at mid-stroke. *Delay*: start the simulation at mid-stroke with the wing vertical and do not start rotating until after the first end of translation. The resulting vertical velocity and vorticity contours as well as their respective kinematics are shown after 25 cycles, see figure 11. The magnitude of the velocity found within the jet reaches 80% of the maximum translational velocity at a time when the airfoil is at the end of translation and as far from the jet as possible.

It is also worth noting that the persistent jet was not a phenomena encountered for all kinematic motions. Not all kinematic combinations yield a jet in the two-dimensional simulations. The conditions which tend to suppress the jet formation are a combination of low angles of attack (higher angular amplitudes), coupled with synchronized rotation. The lower angles of attack cause a smaller pocket of downward momentum to start with, and coupled with the weaker/nonexistent vortices due to the flow no longer separating, leads to a situation which is not able to sustain a persistent downward jet. One consequence of this is symmetric force histories during the forward and back strokes.

The lift coefficients experienced by the various starting conditions, see figure 12, further serve to illustrate the consequence of the jet interaction. Note: force histories are compared when the airfoil is in the same position, i.e. the phase

of the reverse case is shifted by half a period. When the wing encounters the jet, the flow on the underside of the wing is accelerated, decreasing the pressure on the underside and therefore the lift. The end result is that lift is decreased during the start of one (forward or backward) stroke, affecting the wake-capture peak and into the wake valley, and the end of the other (backward or forward) stroke, influencing the wake valley and delayed stall peak. Some combinations of kinematic parameters even yield negative lift values during the local minimum we refer to as the wake valley.

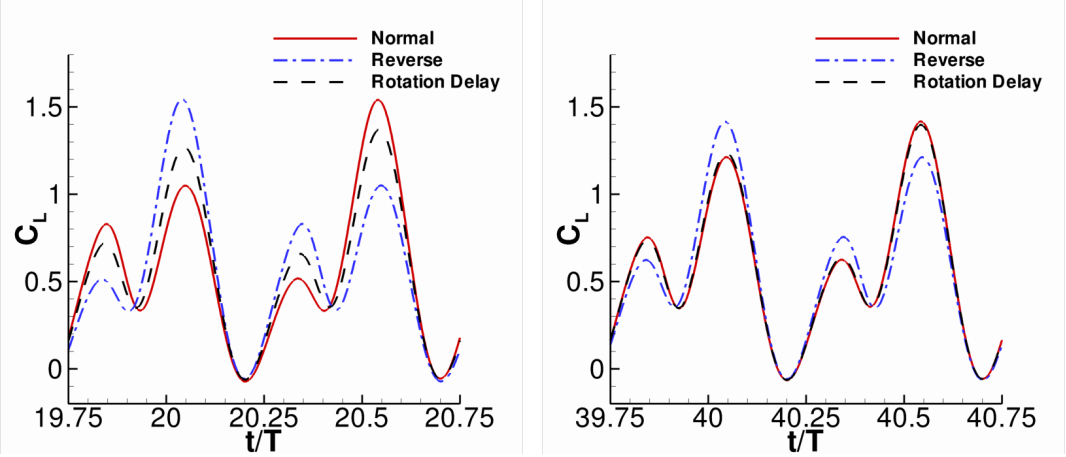

Figure 12. The lift coefficients of two-dimensional computation at Re=100 for the three starting conditions after 25 periods (left) and 40 periods (right). The centered jet created by the delay case moves to a stable configuration to one side. For the cases studied the eventual preference was dictated by the initial direction of motion of the wing. After 40 periods the *normal* and *delay* cases overlap completely while still differing from the *reverse* case noticeably.

Also shown in figure 12 is the force history after 40 periods. At this point the *delay* case has assumed the same lift coefficient magnitude as the *normal* case. The jet, appearing roughly centered for the early cycles of the *delay* case, evolves until reaching a more stable configuration off centered slightly to one side. While

the time averaged lift is not very sensitive to the choice of starting conditions, the two-dimensional instantaneous lift can be. In the finite aspect ratio cases, the vortices dissipate quicker and the jet effect is not as pronounced. One difficulty in quantifying the direct impact of the jet is the fact that other unsteady mechanisms are generally at play, however the response over time helps delineate the impact as the consequence of the rapid pitch down is felt identically for all cycles.

3.1.2 Instantaneous Lift and Drag as Design Variables are Varied

In this section one design variable will be varied at a time to illustrate the competition of effects on the force histories between the unsteady flight mechanisms. Not all of the conclusions can be generalized as being indicative of what would happen elsewhere in the design space as the variables are perturbed, but some generalizations can be made after combining the knowledge of the individual cases with the surrogate modeling results of the subsequent sections.

Figure 13 and 14 show the instantaneous 2D/3D lift and drag respectively for selected cases. Row (a) in both figures shows the force history as the plunging amplitude is varied. Because the Re is fixed, the plunging amplitude is inversely proportional to the flapping frequency. Therefore, a shorter plunging amplitude also implies a shorter period. A shorter period would give the wake less time to dissipate between strokes (though there is no implied statement of those wake strengths being equal).

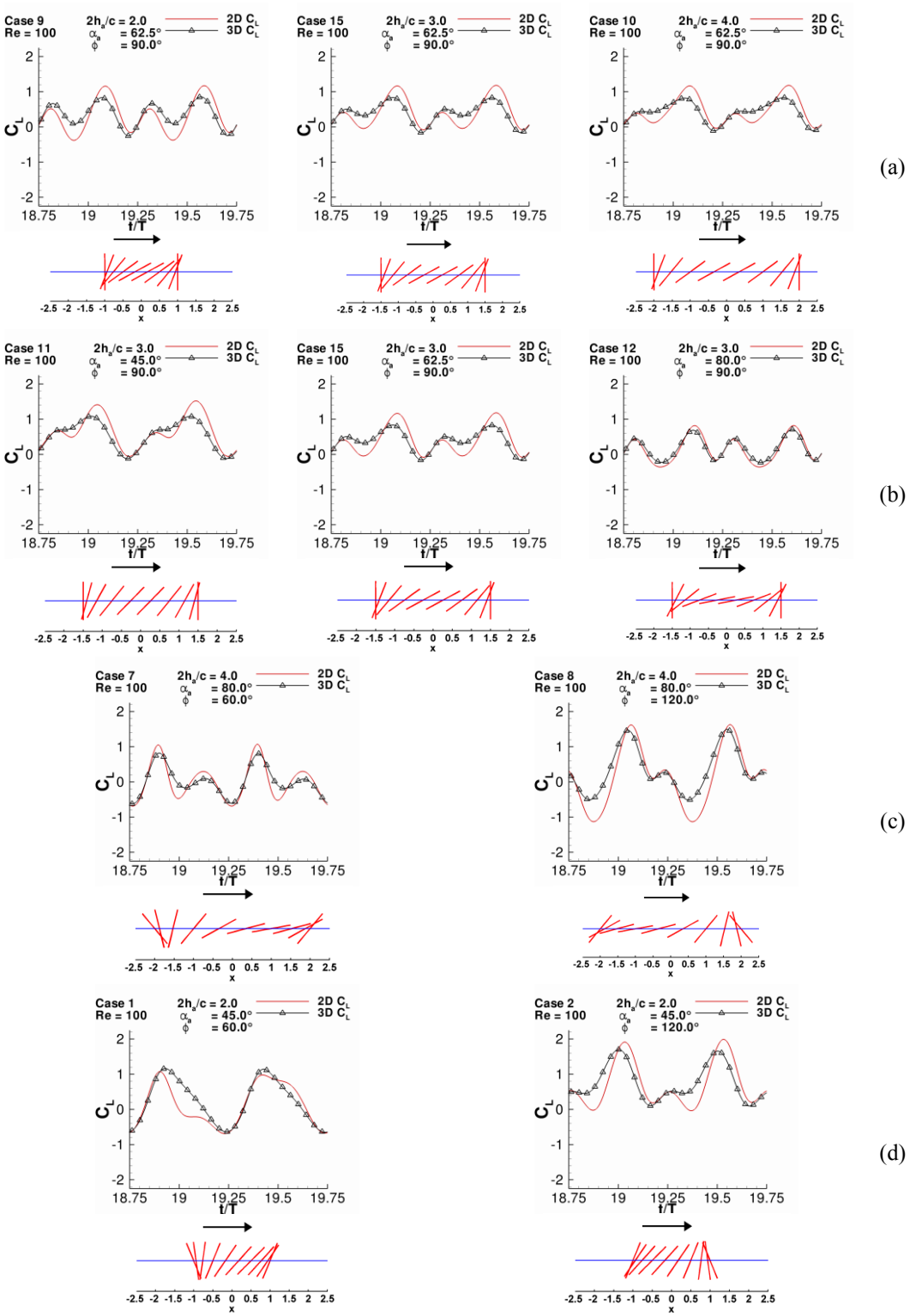

Figure 13. Time histories of the lift coefficients for selected cases (a) as $2h_a/c$ is increases from 2.0 (left) to 4.0 (right) holding α_a= 62.5° and ϕ=90° (b) as

α_a is increased from 45° (left) to 80° (right) while holding $2h_a/c$ =3.0 and ϕ=90° (c) examining delayed rotation ϕ=60° (left) and advanced rotation ϕ=120° (right) while holding $2h_a/c$ =4.0 α_a= 80° (d) examining delayed rotation ϕ=60° (left) and andvanced rotation ϕ=120° (right) while holding $2h_a/c$ =2.0 α_a= 45°.

We see two effects on the 2D lift. The first is a minor but noticeable decrease in the wake-capture peak, the first/third local maxima in figure 13, as the plunging amplitude is decreased. The second is a less sensitive wake valley. Both of these observations are in line with weaker wake-capture mechanisms, weaker rotational circulation, and weaker persistent jet interactions as the plunging amplitude increases. There is not a big effect on the LEV peak however. The differences between 2D and 3D will be looked at later, but suffice it to say despite the noticeable differences in 2D and 3D lift, the drag (see figure 14) is fairly insensitive to the availability of an extra special dimension. The drag also responds to the plunging amplitude, most noticeably again at the end of strokes where the wing is vertical. The shorter plunging amplitude experiencing higher frequencies and higher instantaneous peaks in drag.

Row (b) in figures 13 and 14 illustrates the force histories as the angular amplitude is varied. Note that higher angular amplitudes signify lower AoA. This time the change in the wake-capture peak is not as noticeable. What does change appreciably is the 2D wake-valley and the magnitude of the LEV peak. As the angular amplitude increases the angular velocities increase. At the start of the stroke this larger downward motion in turn leads to larger dips in lift. The LEV peak on the other hand suffers as the angular amplitude is increased because the

AoA is decreased which serves to suppress the LEV growth. The weaker LEV then leads to a less substantial LEV peak. While the higher AoA leads to more lift, the wing also accrues more drag (see figure 14) as the AoA increases.

Rows (c) and (d) in figures 13 and 14, illustrate two instances as the phase lag changes as the influence is slightly more complex. The delayed rotation cases both start off with negative lift, as the kinematic illustration points out the wing is flying upside-down at this point. After that however (c) shows a secondary lift peak as the larger angular amplitude now serves in a pitch up fashion to increase the lift. Row (d) on the other hand shows a highly asymmetric force history whose kinematics will be focused on later. There is a price to pay on the drag side however; as the wing is near vertical as it accelerates horizontally, this results in the largest instantaneous peak drag values of the cases studied.

On the advanced rotation side of the spectrum, again figure 13 and 14 rows (c) and (d), there are a few noticeable phenomena as well. One of the first things that should be noted is the higher LEV lift peaks associated with the advanced rotation. These kinematics benefit from increasing angles of attack during maximum translational velocity. This moves the timing of the pitch down motion and is also responsible for the exaggerated wake valleys experienced for these same kinematics.

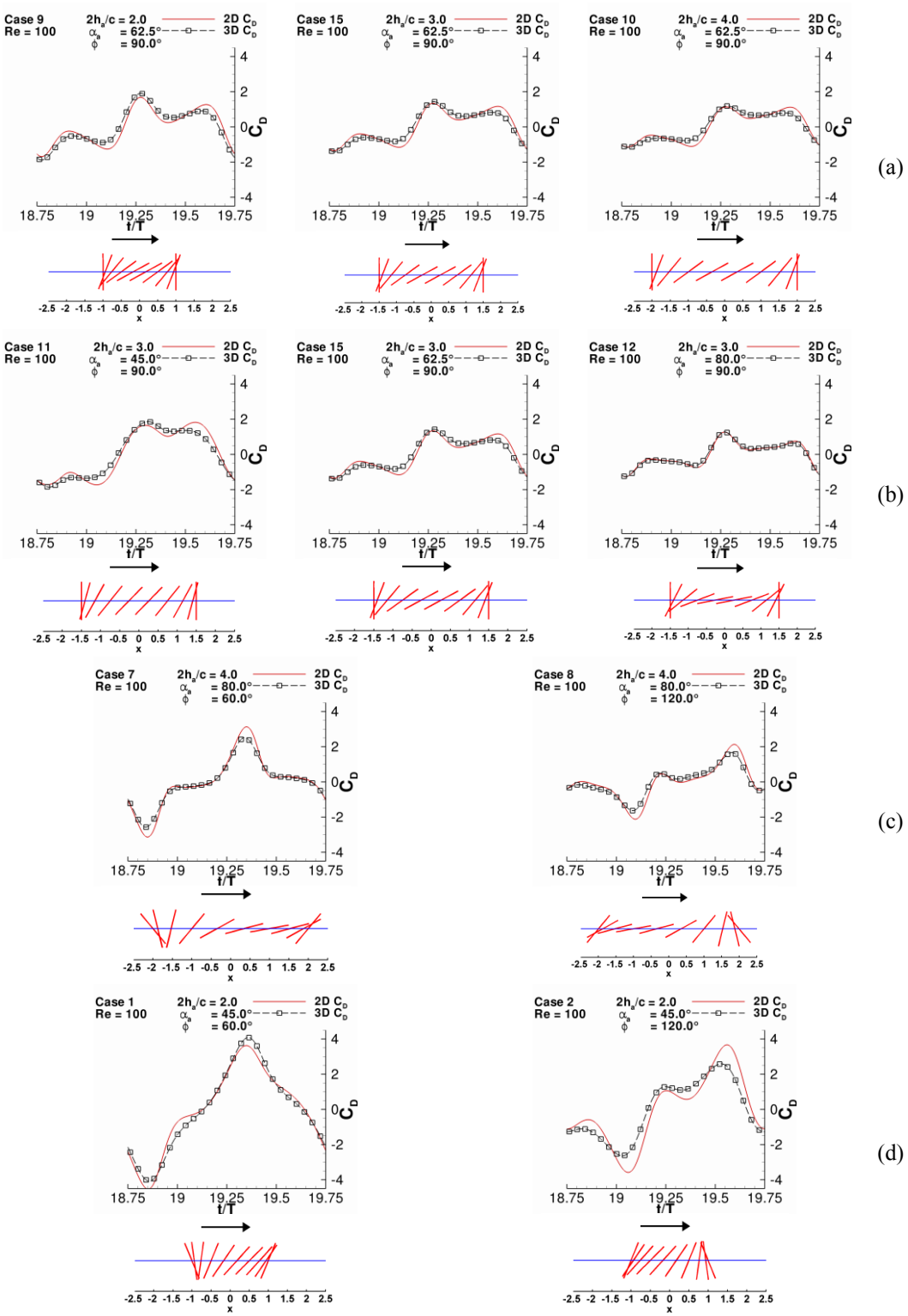

Figure 14. Time histories of the drag coefficients for selected cases (a) as $2h_a/c$ is increases from 2.0 (left) to 4.0 (right) holding α_a= 62.5° and ϕ=90°

(b) as α_a is increased from 45° (left) to 80° (right) while holding $2h_a/c$ =3.0 and ϕ=90° (c) examining delayed rotation ϕ=60° (left) and advanced rotation ϕ=120° (right) while holding $2h_a/c$ =4.0 α_a= 80° (d) examining delayed rotation ϕ=60° (left) and andvanced rotation ϕ=120° (right) while holding $2h_a/c$ =2.0 α_a= 45°

One point it is worth emphasizing here is that it would appear possible to keep most of the desirable flow features while minimizing the less desirable ones, e.g. the deep wake valley, by confining the downward rotation to the end of stroke and then finding a balance between the desire for high AoA and increasing AoA. Looking at the drag illustrations in rows (c) and (d) of figures 13 and 14 it is seen that, while the maximum LEV lift peak values are similar, the same cannot be said for the drag maxima. Once again the higher AoA as the airfoil is decelerating causes higher drag values. The competition of effects is important to keep in mind as one wants to extend the application of the context presented here, e.g. not confining oneself to sinusoidal motions.

While specific examples have been chosen to illustrate key concepts, what kind of general trends can be extracted from the data?

3.2 Time-Averaged Lift

Figure 15 shows the surrogate models of the time-averaged lift, including those based on the two-dimensional and three-dimensional results, as well as their differences. Each axis corresponds to one of the design variables while the color contours illustrate the objective function of interest (e.g. time averaged lift or power). Qualitatively, the general trends found in two- and three-dimensional cases are consistent. As the angular amplitude is increased, a lower angle of attack

results, causing a decrease of the lift. The general trend for plunging amplitude is also largely consistent between two- and three-dimensional cases. Alter the plunging amplitude and the resulting lift does not change significantly for much of the design space. There are regions in the design space where the time averaged lift shows clear differences between two- and three-dimensional cases. A closer inspection of the quantitative relationship between the lift and the kinematic parameters reveals that these differences can be substantial (illustrated in figure 15). These will be highlighted shortly.

To show the global impact of the kinematic variables in the entire design space Figure 16 illustrates the total variances due to the respective design variables. Immediately apparent is the change in the hierarchy of design variables. In two dimensions, the time-averaged lift was the most sensitive to the angular amplitude, significantly less sensitive to the phase lag, and even less still to the plunging amplitude. While the plunging amplitude was not a negligible influence, such an analysis cannot only rank the relative importance but also illuminate variables which do have negligible influence. A finding of this nature can reduce the dimensionality of the design space, greatly reducing the time it takes for refinement iterations, because that variable can effectively be treated as a constant. In this study the plunging amplitude has been kept as a design variable for completeness.

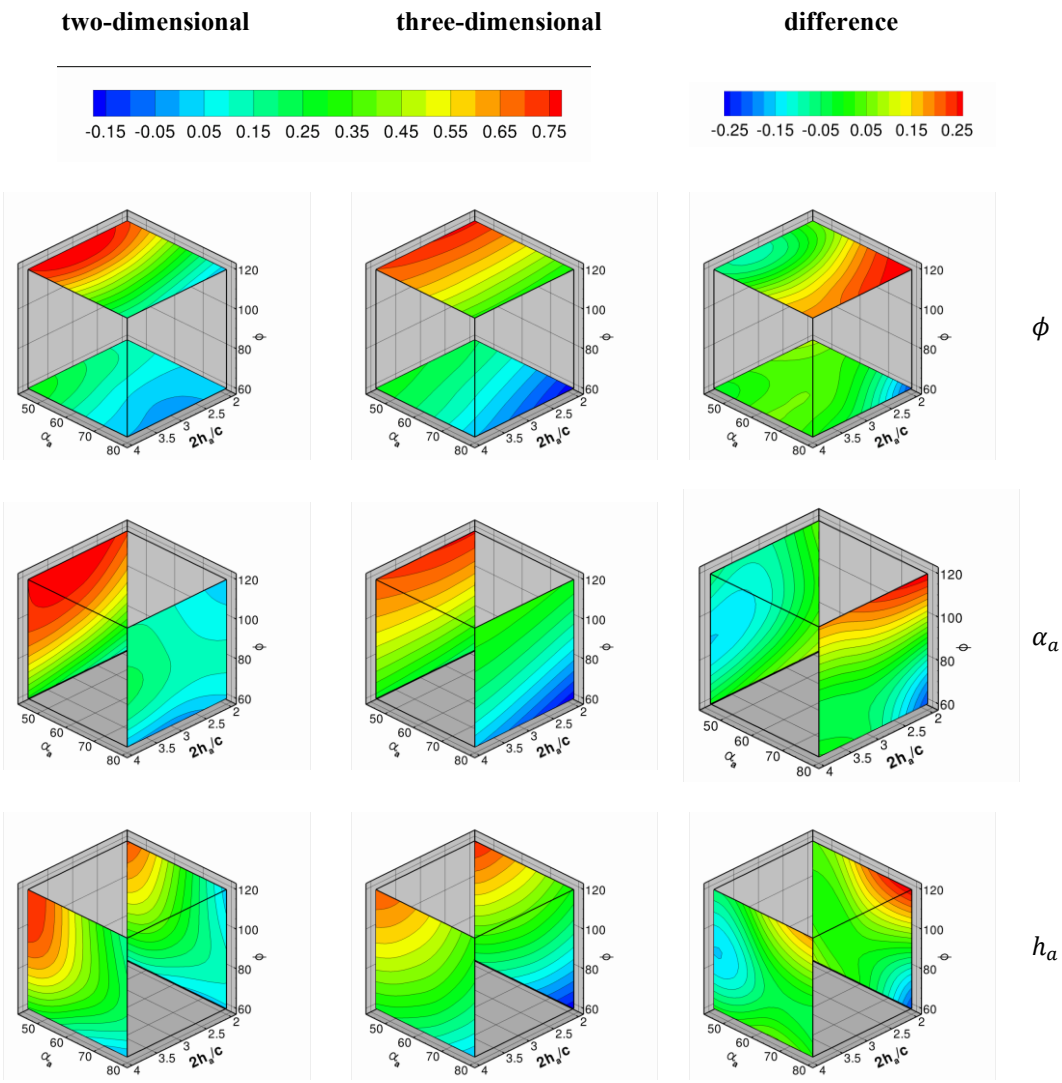

Figure 15. Surrogate modeling results for lift. Left: two-dimensional, Middle: three-dimensional, Right: three-dimensional minus the two-dimensional time averaged lift.

In the three-dimensional case, figure 16 reveals both the plunging amplitude and the phase lag have substantially increased importance relative to the average lift produced compared to the two-dimensional case. So much so that the hierarchy of sensitivity changes from: 1) α_a 2) ϕ 3) h_a in two-dimensional, to three-dimensional where the order is 1) ϕ 2) α_a 3) h_a. In the present context the

main and total variances are close enough not to warrant separate plots. This in turn implies a relatively small degree of coupling between the design variables and their resulting effect on the integrated lift.

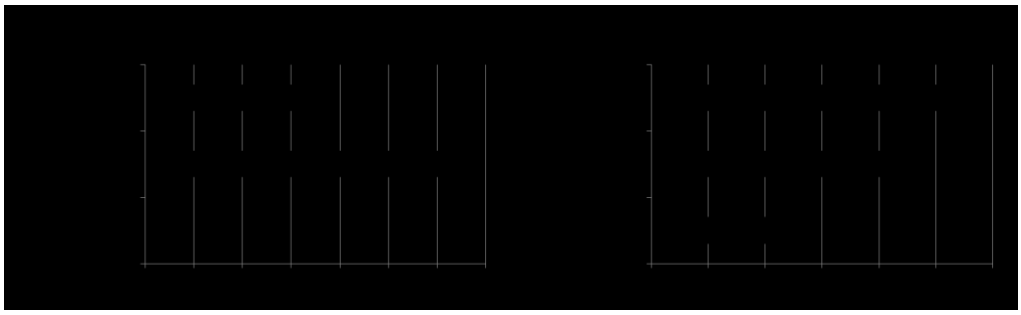

Figure 16. Global sensitivity analysis (GSA) of lift for two-dimensional and three-dimensional hovering kinematics.

To identify where in the design space 3D effects become important, iso-surfaces of the absolute difference between the two and three-dimensional lift coefficients are shown in figure 17. The green regions in the design space correspond to the kinematic parameters with the difference in time-averaged lift coefficient larger than 0.1 due to three-dimensionality. Four coherent regions are identified: region 1, characterized by synchronized hovering and low angular amplitude; region 2, with advanced rotation and high angular amplitude; region 3,with delayed rotation, low angular amplitude, and small plunging amplitude; and region 4, delayed rotation, high angular amplitude, and low plunge amplitude. Everywhere else the differences between the two- and three- dimensional lift is below the 0.1 threshold. The similarities in this catch-all region are defined by the

likeness of their time averaged values, but in some instances, as will be shown, stronger statements may be appropriate.

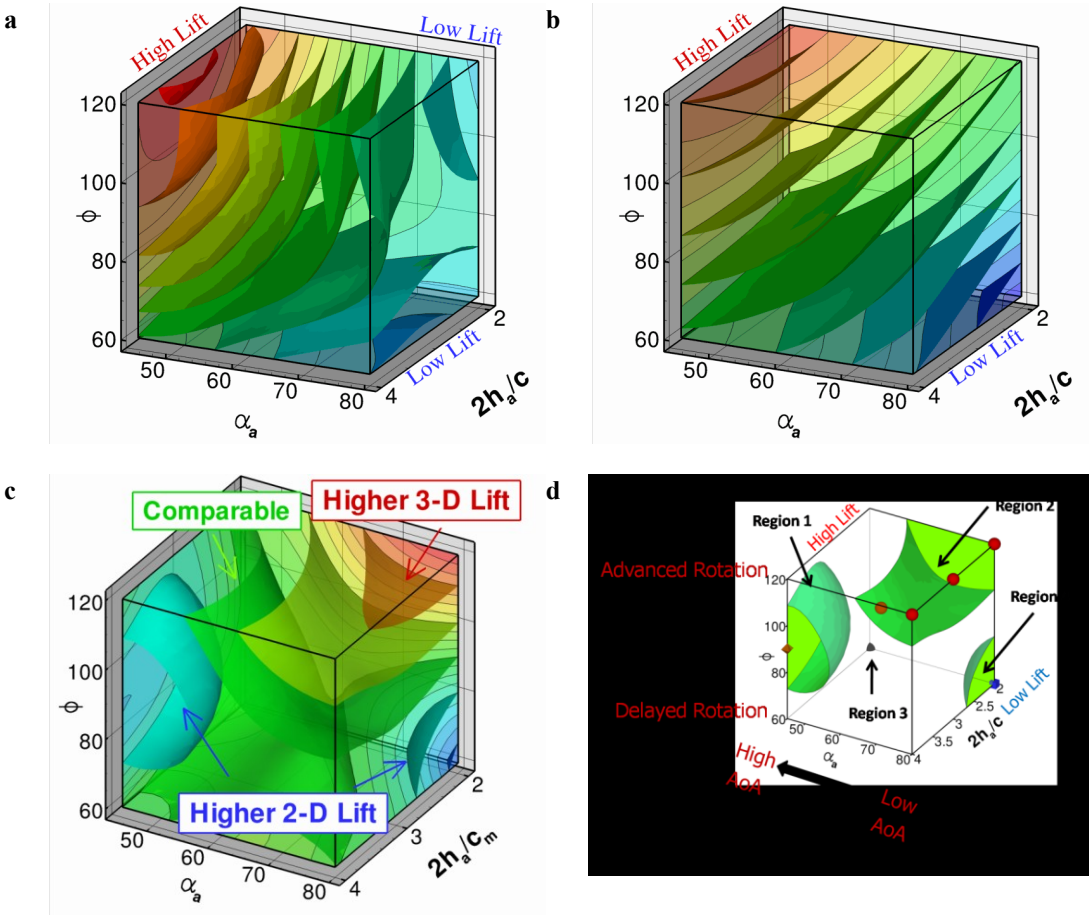

Figure 17. Iso-sufaces of 2D lift (a), 3D lift (b), 3D minus 2D lift (c), and (d) where the absolute difference between the 2D and 3D lift equals 0.10. The symbols denote training points in those regions for which detailed force histories and flow field quantities are available; brown octahedra (region 1), circles (region 2), black quarter sphere (region 3), and a blue cube (region 4).

3.3 Region 1; Synchronized Hovering, High AoA

Region 1 is defined by kinematics that are close to synchronized hovering (i.e. including cases with slight delayed or advanced rotation), low angular

amplitude (high AoA), and larger plunging amplitudes. The time history of lift, see figure 18, shows two local maxima per stroke in 2D. The first peak is associated with the wake capture at the beginning of the stroke at t/T = 0.8. Between the two peaks is a local minimum referred to as a wake valley which is caused by a combination of decreasing angle of attack and interaction with a pocket of downward momentum. For this region of the 2D kinematic design space, this pocket of downward momentum takes the form of a persistent jet. As reported during the experimental studies of Freymuth (1990) and numerically by Trizila *et al.* (2008a,b), the jet develops as a result of a reverse Karman vortex street interacting with the downward momentum created by the wing as it translates. As the wing passes the jet, vortices are shed with an orientation that reinforces the downward momentum previously created by the wing. These vortices sustain the downward momentum, and further entrain surrounding fluid, as to create a flow feature which the wing then interacts with during subsequent stroke.

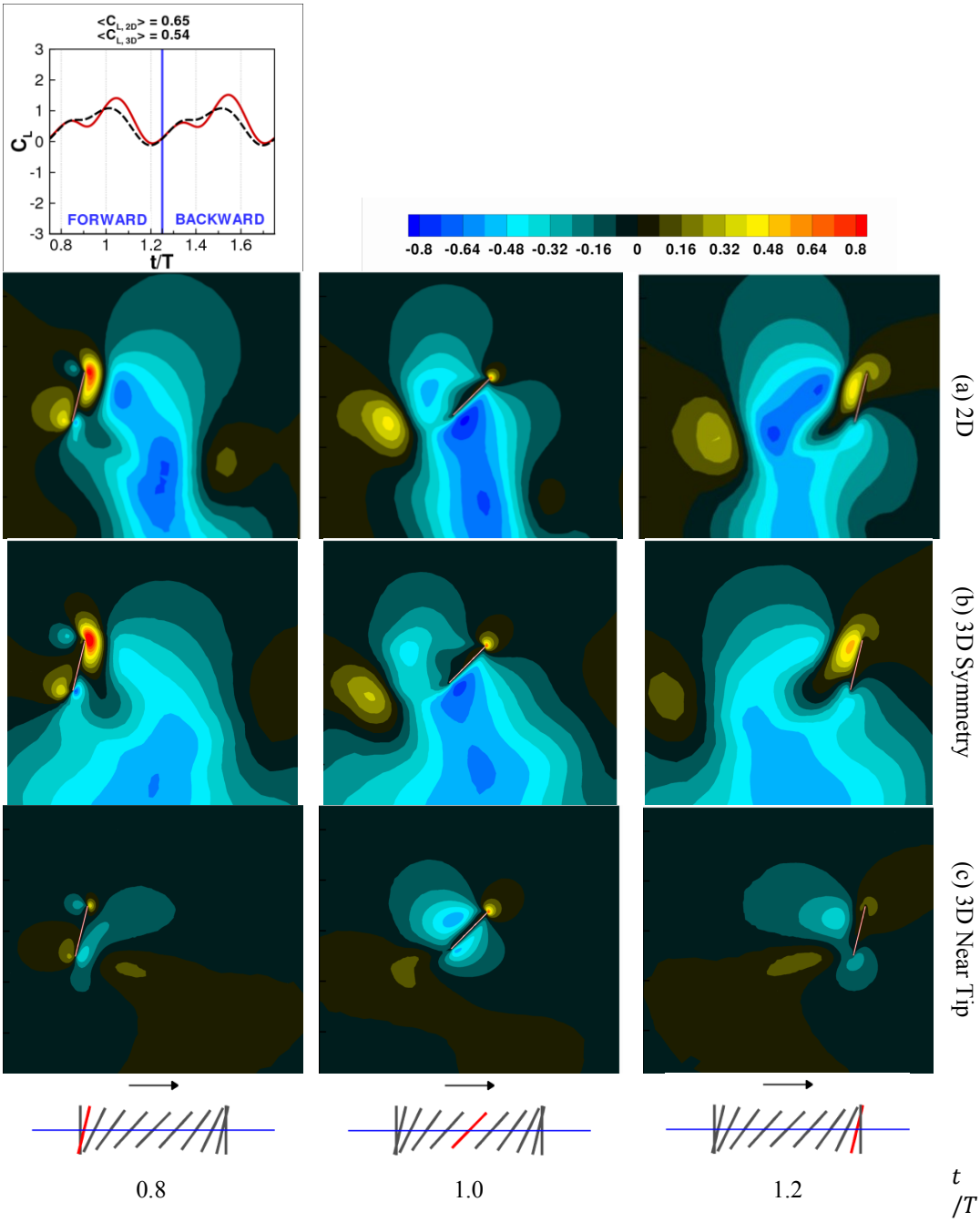

Figure 18. Instantaneous force history (2D: red, 3D: black) and vertical velocity contour plots at three time instants in the forward stroke for the case 11 (h_a=3.0,α_a=45°,ϕ=90°): (a) from two-dimensional computation; (b) in the symmetry plane of three-dimensional computation; (c) near the wingtip (z/c = 1.8).

In general the tip vortices are found to have four prominent competing effects: TE1) Enhancement of lift due to the proximity of the associated low pressure region of the tip vortex next to the airfoil, TE2) Induced downwash acting to reduce the effective angle of attack along the span weakening the LEV hence reducing the instantaneous lift, TE3) Interaction with the vortices shed from the leading and trailing edges anchoring them from shedding near the wing tips enhancing the lift (region 3), TE4) Due to the tip vortices pulling fluid from the underside of the wing to the upper side, the wing leaves behind a weaker pocket of downward momentum in the flow. Upon interaction with this downward momentum, a loss in lift is seen and so weaker wake-valley means higher lift.

The overall impact for this case is that the two-dimensional lift, $<C_{L,2D}>=$ 0.65, is better than the three-dimensional counterpart, $<C_{L,3D}>=$ 0.54. More generally, cases with kinematics in region 1 have larger lift in 2D.

3.4 Region 2; Advanced Rotation, Low AoA

In region 2 the kinematics are characterized by advanced rotation, and high angular amplitude. Figure 19 shows the time histories of lift and the associated flow features from case 8 ($2h_a/c = 4.0$, $\alpha_a = 80°$, and $\phi = 120°$) which is representative for the other cases in region 2.

Right after the stroke reversal, the flat plate moves into the wake generated in the previous stroke. Due to the downwash in this wake, see figure 19C1, and low and decreasing angle of attack (figure 19B), lift drops. Note: the

pocket of downward momentum encountered for these kinematics is not a persistent jet. The three-dimensional case does not suffer the same drop in lift as the two-dimensional case.

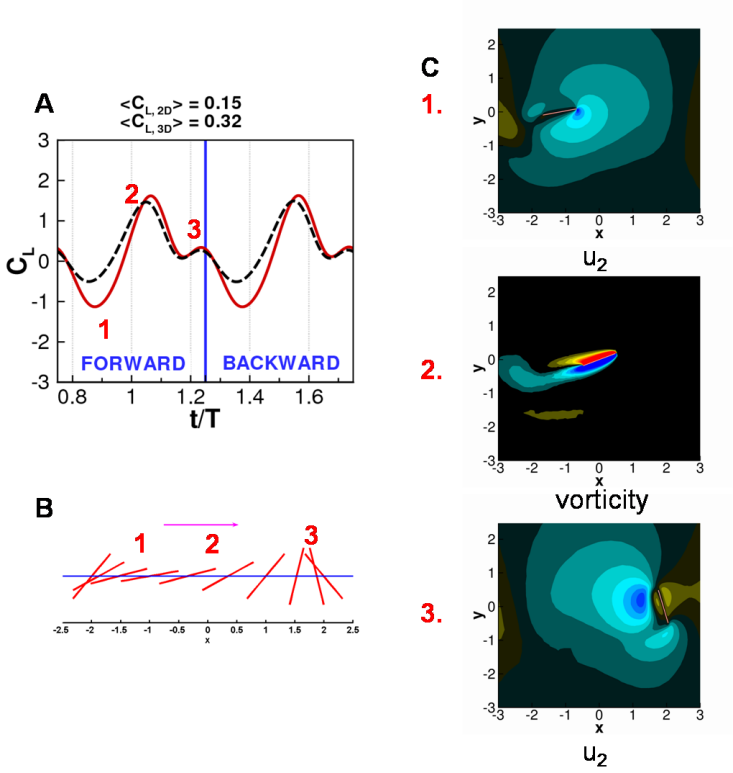

Figure 19 Time history of lift coefficients in a representative case in region 1, $2h_a/c = 4.0$, $\alpha_a = 80°$, and $\phi = 120°$, with the associated flow features. (A) Lift, (C_L), during a motion cycle. Red-solid, two-dimensional computation; black-dashed, three-dimensional computation. (B) kinematic schema of the flat plate motion. (C) Representative flow features at 1) t/T = 0.9, u_2 contours; 2) t/T = 1.0, vorticity contours; 3) t/T=1.2, u_2 contours.

3.5 Region 3; Delayed Rotation, High AoA, Low Plunging Amplitude

In classical steady state theory the presence of wing tip vortices is attributed to a loss of lift and increase in drag when comparing the two-

dimensional wing to its finite three-dimensional counterpart [Anderson (2006)]. What is seen, in the current study, are instances in which low aspect ratio, unsteady aerodynamics are producing tip vortices which can enhance lift while negligibly influencing the drag (highlighted in section 3.7).

Region 3 is defined by kinematics with delayed rotation, low angular amplitude (high AoA), and shorter plunging amplitudes. This region shows a significant impact from the tip vortices. Figure 20 presents a delayed rotation case with $2h_a/c=2.0$, $\alpha_a=45°$, $\phi=60°$. The difference in the flow physics encountered due to three-dimensional phenomena is noticeable. The main characteristics of the vortices, including sizes, strengths and movement are distinctly different between two- and three-dimensional results. Not only is there a strong spanwise variation in the three-dimensional flow, but also there is little resemblance between the symmetry plane of the three-dimensional computations and the two-dimensional computations.

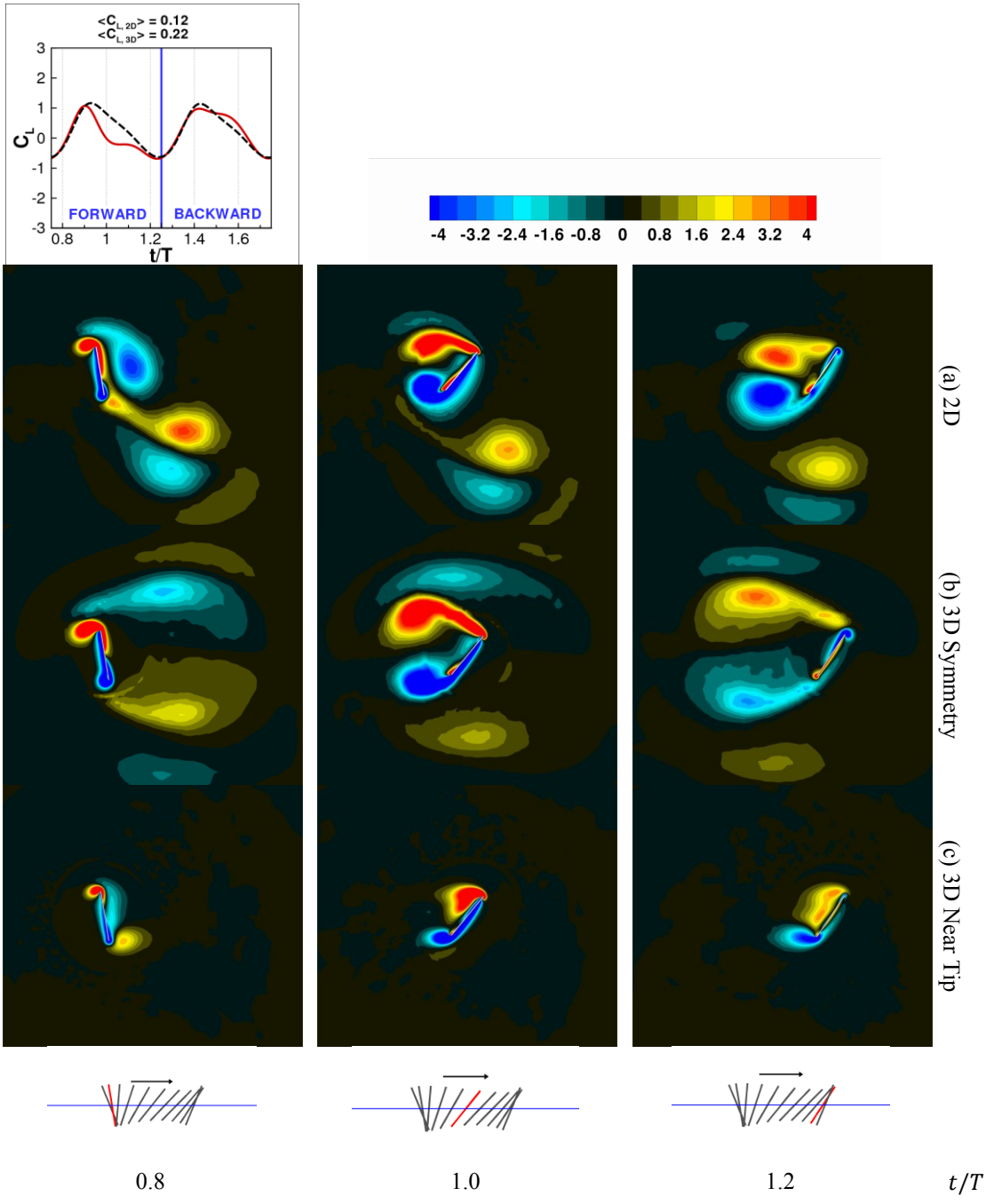

Figure 20 **Force history (2D: red, 3D: black) for a flapping cycle and z-vorticity contour plots at three time instants in the forward stroke for the case 1 ($h_a = 2.0, \alpha_a = 45°, \phi = 60°$): (a) from two-dimensional computation; (b) in the symmetry plane of three-dimensional computation; (c) near the wingtip (z/c = 1.8).**

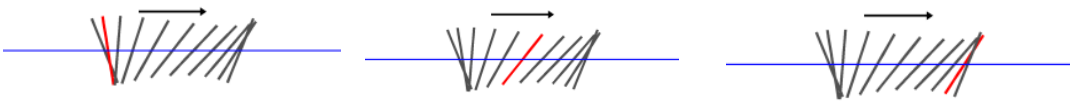

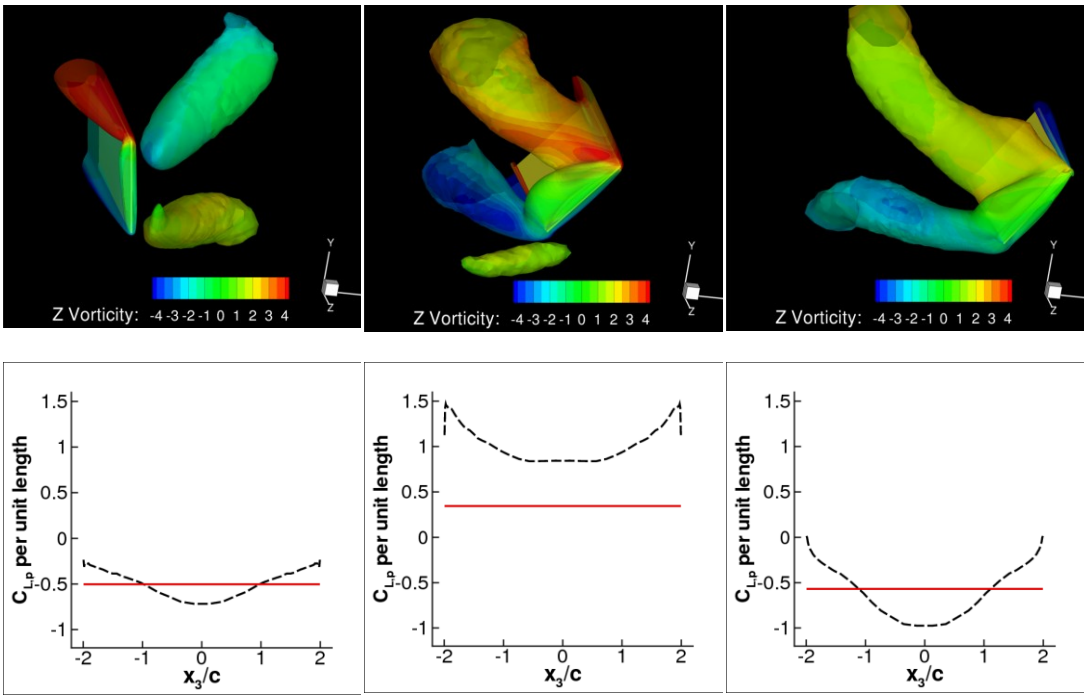

t/T = 0.8 t/T = 1.0 t/T = 1.2

Figure 21. The lift per unit span and iso-Q surfaces (Q=0.75) colored by z-vorticity over half of the wing using the kinematic parameters $2h_a/c$ =2.0,α_a=45°,ϕ=60° (case 1) at Re = 100 at t/T= 0.8, 1.0, 1.2. The spanwise variation in forces is examined with the two-dimensional equivalent marked for reference. Time averaged lift coefficient for i) two-dimensional: 0.13, ii) three-dimensional: 0.22.

In two-dimensional flow, the pair of the large scale vortices are noticeably closer to each other and to the airfoil than that in the three-dimensional flow. The instantaneous lift coefficient for the two cases examined is illustrated in figure 21, depicting noticeable differences in that the three-dimensional lift coefficient is generally higher than its two-dimensional counterpart. With these kinematics patterns the tip vortices can interact with the LEV to form a lift enhancement mechanism. This aspect will be discussed next.

Figure 21 shows an iso-Q [Hunt *et al.* (1988)] contour colored by ω_3, the spanwise-vorticity. In this fashion we can separate the rotation from the shear, via Q,which can be used as a measure of rotation, and then get directional information with vorticity. The vortices shed from the leading and trailing edges are identified by red and blue colors respectively, while the tip vortex is left green. The role of the tip vortex in the hovering cases studied is particularly interesting. For the case presented in figure 21 (delayed rotation), the Q iso-surface colored with ω_3, along with the spanwise distribution of C_L, due to pressure, the effects of the tip vortices become apparent. Firstly, there is a low pressure region at the wing tip favorably influencing the lift (TE1). Furthermore, the tip vortex anchors the large scale vortex pair near the tip (TE3). At midspan, however, the vortex pair has separated from the wing. This in turn drives the spanwise variation seen in the flow structures and force history.

Compared to an infinite wing, the tip vortices caused additional mass flux across the span of a low aspect-ratio wing, which helps push the shed vortex pair, from the leading and trailing edges, at mid-span away from one another. Furthermore, there is a spanwise variation in effective angle of attack induced by the downwash (TE2), stronger near the tip. Overall, the tip vortices allowed the vortex pair in the neighborhood of the tip to be anchored near the wing surface, which promotes a low pressure region and enhances lift. The end result is an integrated lift value that considerably departs from the two-dimensional value.

It is clear that the kinematic motions have a significant impact on tip vortex formation and the leading/trailing edge vortex dynamics. Interestingly, for many of the kinematic motions examined, the tip vortex force enhancement could be confined to lift benefits, i.e. the resulting drag did not increase proportionally!

3.6 Region 4; Delayed Rotation, Low AoA, Low Plunging Amplitude

Region 4 is defined by kinematics with delayed rotation, large angular amplitude (or low AoA), and shorter plunging amplitudes. Figure 22 shows the time histories of lift from the two-dimensional, and the three-dimensional computations along with a schema for the kinematics: $2h_a/c = 2.0$, $\alpha_a = 80°$, and $\phi = 60°$ as a representative case for this region. The largest discrepancy between two-dimensional and three-dimensional cases is seen around $t/T = 0.9$. Because the rotation is delayed, after the stroke reversal at $t/T = 0.75$ the flat plate creates rotational starting vortices to increase the lift, with its first peaks around $t/T = 0.9$. However, as shown in figure 22, in the two-dimensional case, the TEV shed in the previous stroke interacts with the flat plate after the stroke reversal enhancing the lift by the wake-capture mechanism ($t/T=0.9$).

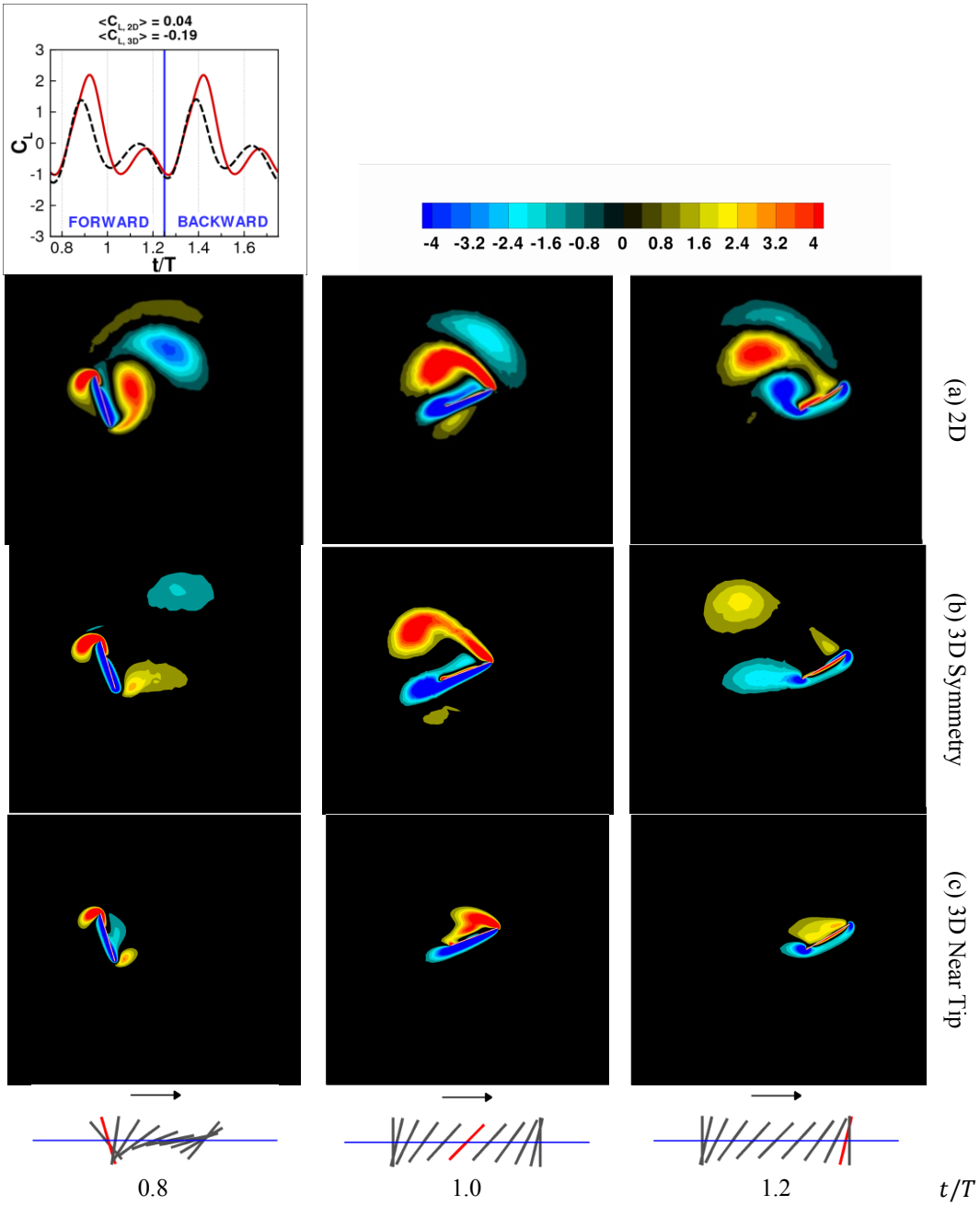

Figure 22. Force history (2D: red, 3D: black) for a flapping cycle and z-vorticity contour plots at three time instants in the forward stroke for the case 3 (h_a=2.0,α_a=80°,ϕ=60°): (a) from 2D computation; (b) in the symmetry plane of 3D computation; (c) near the wingtip (z/c = 1.8) plane.

On the other hand, for the three-dimensional case, the shed LEV and the TEV repel from each other and the path of the flat plate, such that after the stroke reversal, the wake-capturing is absent. The first lift peak in the time history in figure 22 is then only due to the rotational effects. So the diverging behavior of the vortices, observed for all delayed rotation cases, and the interaction of the vortices from the LE, and TE with the wing tip vortex, play a central role as important three-dimensional effects as described in Region 3.

3.7 Region of similarity

For other kinematic combinations, the integrated forces over time match reasonably, i.e. the difference between the two-dimensional, and the three-dimensional time averaged lift is less than 0.1. For some cases even the instantaneous forces agree closely: a synchronized rotation case with low angles of attack is remarkably similar when examining two-dimensional and three-dimensional force histories, see figure 23.

Figure 23 shows the flow fields corresponding to the parameters: $2h_a/c$ =3.0, α_a=80°,ϕ=90°. The variation along the spanwise direction is modest, making the two-dimensional and three-dimensional simulations substantially similar. The two-dimensional flow field and the corresponding three-dimensional flow on the symmetry plane are strikingly consistent.

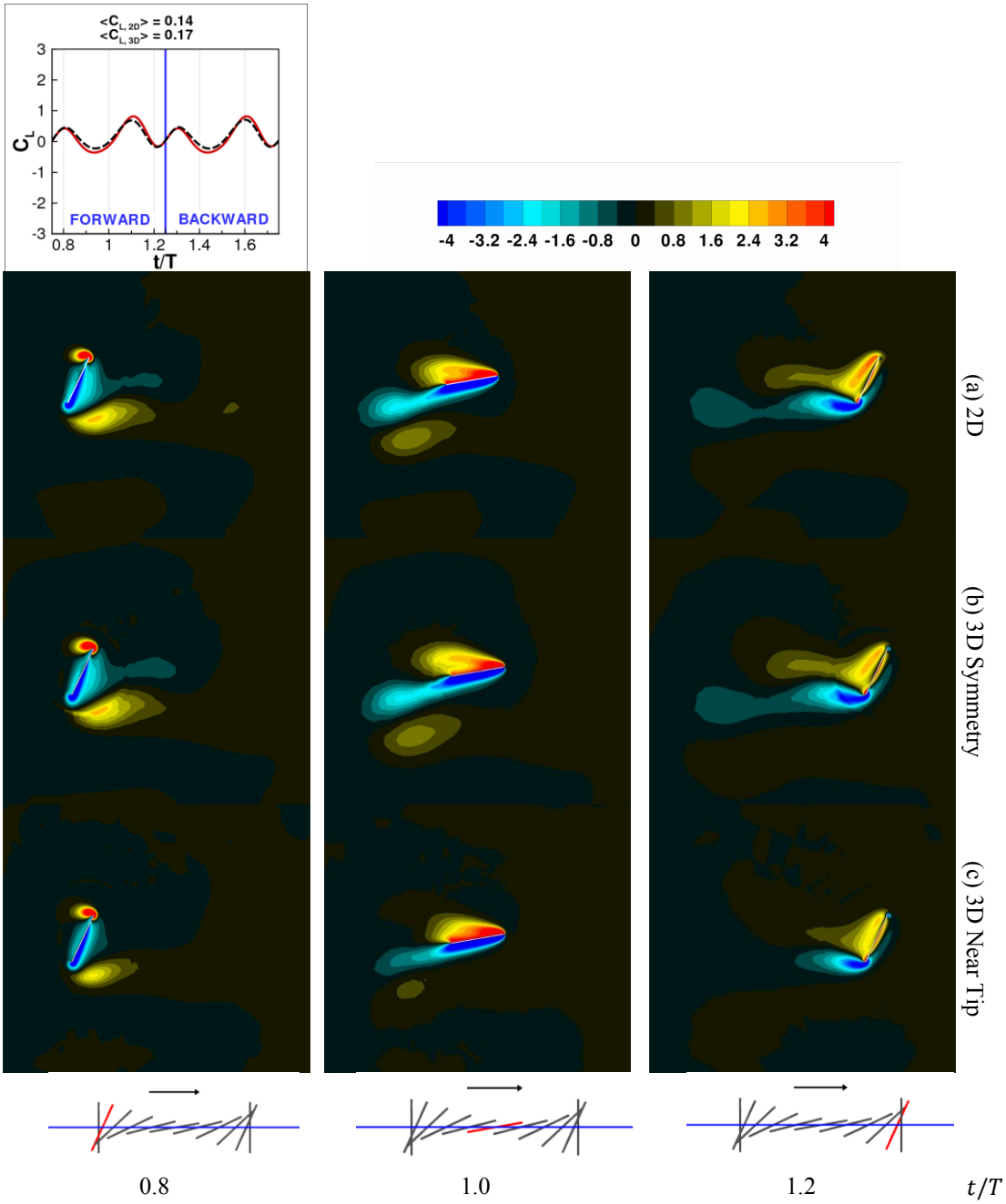

Figure 23. Force history over a flapping cycle (solid red=2D, dashed black=3D) and z-vorticity contour plots at three time instants in the forward stroke for case 12 ($2h_a/c=3.0, \alpha\_a=80°, \phi=90°$): (a) from 2D computation; (b) in the symmetry plane of 3D computation; (c) near the wingtip (z/c = 1.8) plane.

The high angular amplitudes lead to low angles of attack, and coupled with the timing of the rotation, lead to a flow that does not experience delayed stall as the formation of the LEV is not promoted. The timing of the rotation for this example puts the flat plate at its minimum angle of attack, approximately 10°, at maximum translational velocity, while the translational velocity is zero when the flat plate is vertical. It is seen from the flowfield that the tip vortex as well as the leading and trailing edge vortex formation is largely suppressed. The net effect is a fairly uniform spanwise lift distribution closely resembling the two-dimensional case with the same kinematics.

Neither the two-dimensional or three-dimensional results in this case promote downward induced jet formation. As summarized in figure 23, the two-dimensional and three-dimensional lift coefficients of this case are similar in the instantaneous as well as the time averaged sense. One implication illustrated is the usefulness of two-dimensional simulations for quantitative data on a three-dimensional counterpart. However, not all cases in this region display this similar instantaneous behavior, and the time-averaged lift comparison is due to integrating effects which partially cancel out. For instance, the LEV strength may diminish, however the lift valley during the downward rotation may not be as severe in three dimensions.

3.8 Power Requirements

Figure 24 displays the two-dimensional and three-dimensional surrogate responses of the power required, estimated by multiplying the pressure force by the instantaneous translational velocity and integrating over a cycle, as well as their differences.

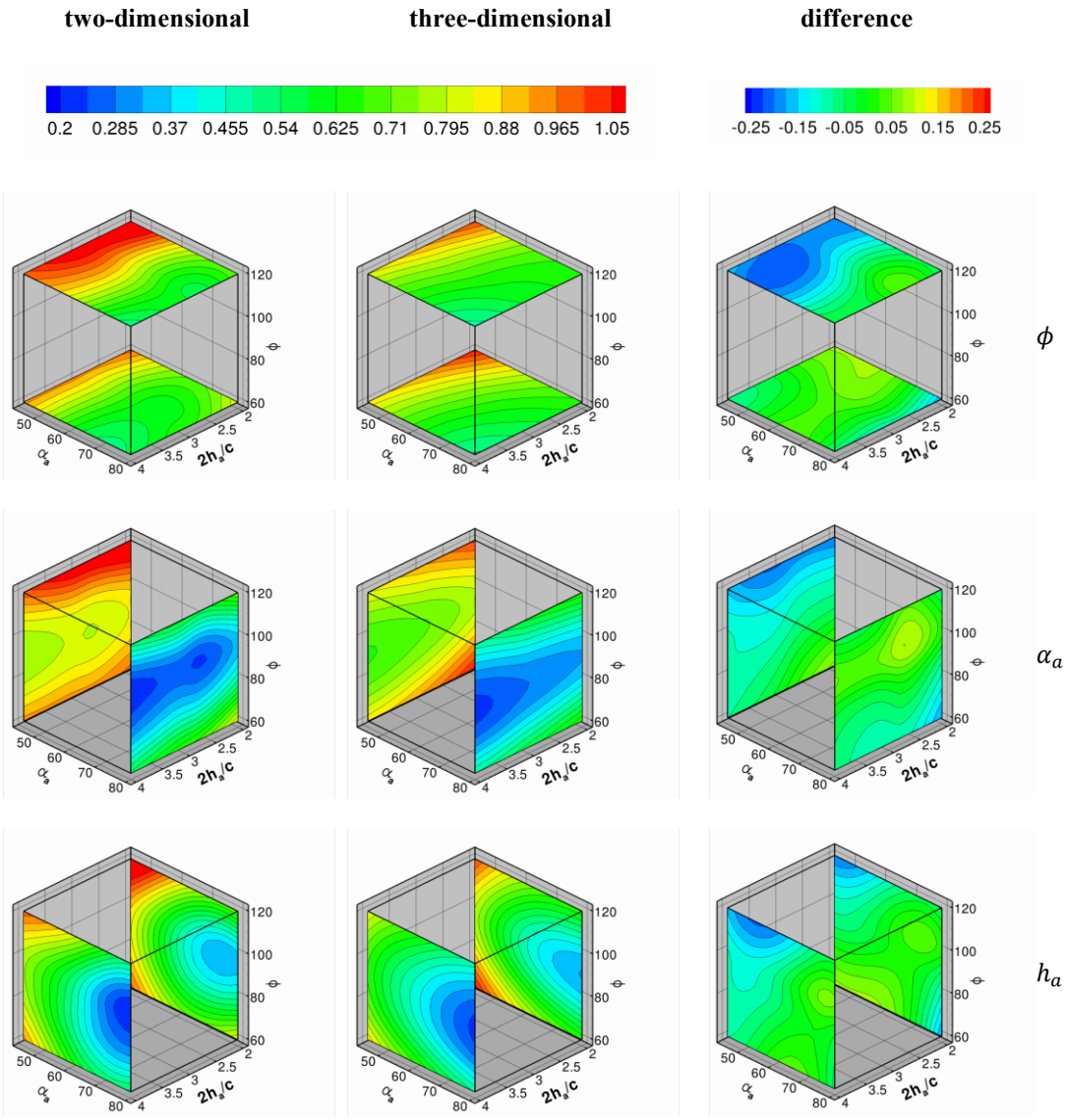

Figure 24. Surrogate modeling results for power required. Left- two-dimensional, Middle-three-dimensional, Right- three-dimensional minus two-dimensional time averaged power requirement approximations.

Not only are all the trends quite similar but the magnitudes also compare quite well (note that the broader range of the contours seen for the power required often yields less significant differences). This implies that certain three-dimensional flow features, not observable/possible in two-dimensional flows, that lift was sensitive to, do not play a significant role in determining the drag for these kinematic combinations. This is an interesting consequence which warrants further study. From the instantaneous force histories, see figure 14, the agreement in drag coefficients is close except at a combination of low plunging amplitudes with low angular amplitudes and low phase lags. Figure 25 measures the sensitivity of the power required to the kinematic variables. The hierarchy remains the same from 2D to 3D, unlike in lift.

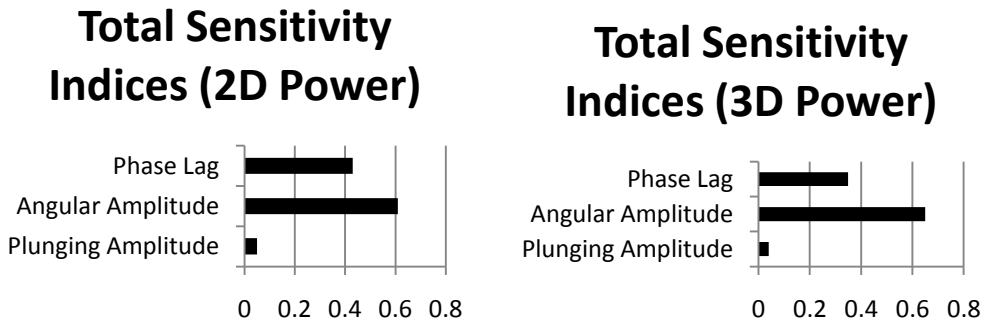

Figure 25. Global sensitivity analysis (GSA) of power for two-dimensional and three-dimensional hovering kinematics.

The physical reasoning behind the observed trends in the two-dimensional and three-dimensional cases is the same, in that the agreement is not

merely a consequence of integration. During normal hovering, $\phi = 90°$, the airfoil/wing is perpendicular to the direction of motion at the ends of translation but has little translational velocity. As the phase lag is perturbed in either direction the airfoil can have an appreciable velocity, while perpendicular to the direction of motion and whether the body is accelerating when perpendicular, as in delayed rotation cases, or decelerating, as in advanced rotation cases has a sizable impact on the instantaneous drag that is felt (see figure 14), and consequently the power required for the maneuver. Compared to the differences between surrogates for lift, the differences for power between two- and three-dimensional cases are smaller overall.

3.9 Pareto Front

In a multi-objective investigation, it is often the case that different goals are in competition regarding suitable selections of design variables. One tool used to evaluate the trade-offs between objective functions is called the Pareto front [Miettinen (1999)]. The Pareto front consists of non-dominated points and can be thought of as the set of best possibilities, as illustrated in figure 26. Non-dominated points can be thought of as points for which one could not improve all objective functions simultaneously. The current objectives are to maximize lift and minimize power requirement. Points on the Pareto front therefore involve those for which increases in lift are accompanied by increases in power, and vice versa. To pose all objectives as minimization expressions, any objective which is maximized, like lift, is multiplied by a negative sign. Note that the Pareto front

itself is comparable between two and three dimensions. The primary differences are the peak lift values attained in two-dimensional flow exceeding their three-dimensional counterparts, and the fact that the density of design variable combinations near the front is higher in the three dimensional case. The paths through the design space are plotted below their respective Pareto fronts in figure 26. Note: the jaggedness of the path is due to the resolution of the tested points and is seen because of the fine balance in objective functions for design variables in that region. It is seen that the high lift region follows the lower bound of the angular amplitude suggesting that future iterations should decrease the lower bound for higher lift solutions. Overall the design variable combinations on the optimal front are consistent qualitatively.

As shown in figure 15, and a representative case illustrated in figure 27, the highest time-averaged lift values are obtained by a combination of advanced rotation and low angular amplitude in two and three dimensions. The general trends present, i.e. when holding two of the input variables constant and varying the last one, remained largely the same. For power required, figure 24 shows that the synchronized rotation cases with high angular amplitude consume the least power for both two-dimensional as well as three-dimensional hovering. The combination of lower angle of attack during the mid-stroke when the translational velocity is at maximum and small translational velocities at the ends of the strokes when the flat plate is vertical minimizes the power. These trends not only

followed similar qualitative trends between two-dimensional and three dimensional cases, but also consistently quantitatively matched in magnitude.

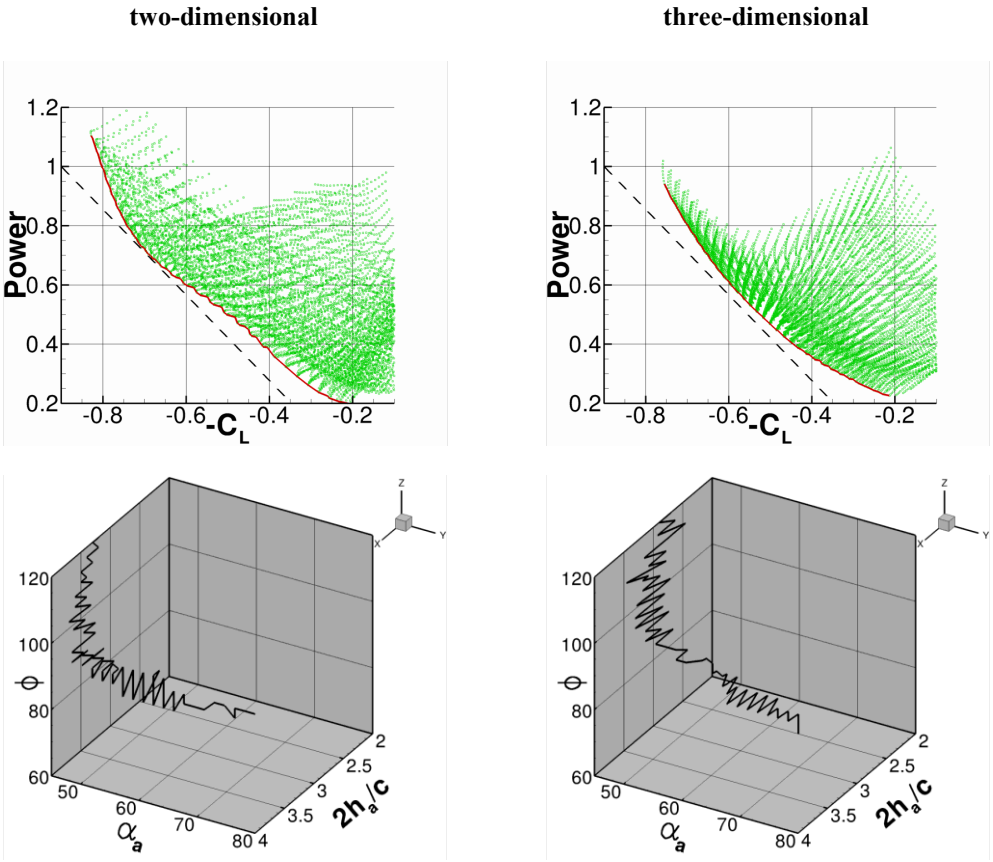

Figure 26. Pareto fronts illustrating the competing objectives of lift and power requirements in two-dimensions (left) and three-dimensions (right) and the design variable combinations which provide those fronts. The dashed line is for reference.

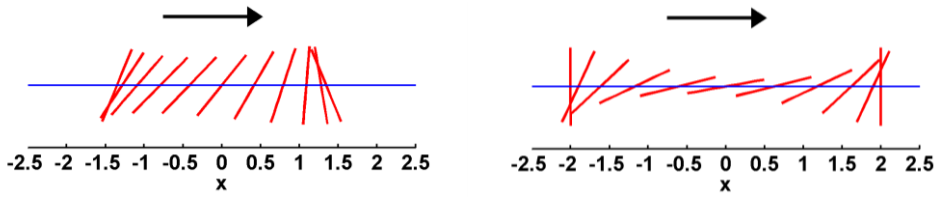

Figure 27. Representative high lift (left: $2h_a/c = 2.7$, $\alpha_a = 45°$, and $\phi = 120°$) and low power (right: $2h_a/c = 4.0$, $\alpha_a = 80°$, and $\phi = 90°$) kinematics.

Chapter 4 Effect of Gust and Freestream on Flapping Wing Aerodynamics

One of the main difficulties in realizing a functional MAV is its inherent sensitivity to the operating environment due to its size and weight. While the vehicle dynamics are going to be sensitive to the environmental perturbations, due to the fact that the flapping frequencies are an order of magnitude or two greater than the wind gusts, O(10) Hz to O(100) Hz versus wind at O(1) Hz, the aerodynamics associated with flapping wings can be pragmatically modeled by a constant freestream. In the current study, environmental sensitivity is looked at using different kinematic schemes, freestream strengths, and freestream orientations. The three kinematic patterns chosen were those of sections 3.3, 3.5, and 3.7. These patterns were chosen due to having pronounced LEVs (section 3.3), beneficial tip vortices (section 3.5), and negligible 2D vs 3D differences (section 3.7) respectively. The freestream strength was fixed at 20% of the maximum translational velocity of the wing. If one were comparing this to fruitflies, (Re O(100) and wingspeed ~3.1 m/s) the freestream would be approximately 0.6 m/s, a relatively light wind or mild disturbance. The directions of the freestream varied between heading down, right, or up.

4.1 Two Dimensional or Infinite Aspect Ratio Wings in a Gust

The 2D cases were much more sensitive to the freestream than their 3D counterparts. Instantaneous lift associated with all three kinematic patterns was very sensitive to the horizontal freestream and much less sensitive to the downward heading freestream. The downward freestream generally decreased lift, by suppressing vortex generation, while making the forward and backstrokes more symmetric as the vortical activity was washed away from the airfoil more quickly. Overall the general nature of the force history was kept intact. On the other hand the upward freestream had the opposite effect. Namely the vortex interactions were sustained for a longer period of time as the freestream held the wake closer to the airfoil and the increased angle of attack also served to accentuate the unsteady aerodynamics. This upward freestream may or may not have had a significant impact on the force history which was dependent on the kinematics. The horizontal freestream had the largest impact over the range of kinematic motions studied, sometimes more than doubling the lift felt for freestream strength of 20% of the maximum translational velocity, a relatively tame environmental situation leading to a significant change in hovering performance.

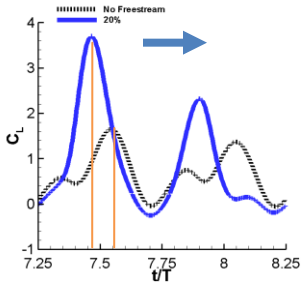

a) 2D C_L

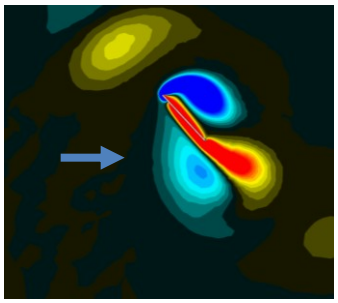

b) 20% freestream at t/T=8.45

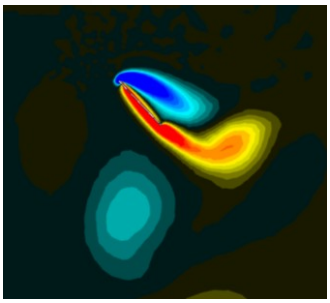

c) no freestream at t/T=8.55

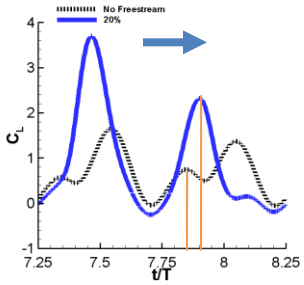

d) 2D C_L

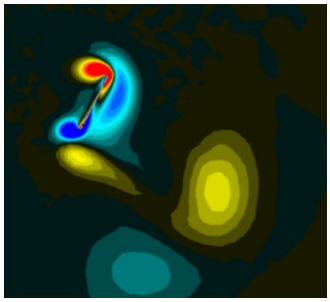

e) no freestream at t/T=7.85

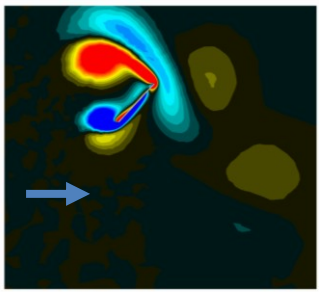

f) 20% freestream at t/T=7.9

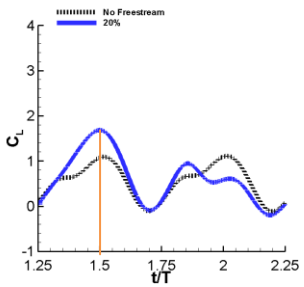

g) 3D C_L

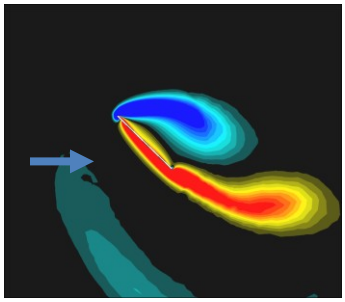

h) 3D Mid-span (z/c=0) t/T=1.5 20% freestream

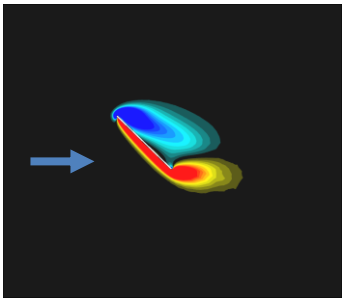

i) 3D Wing Tip (z/c=1.95) 20% no freestream

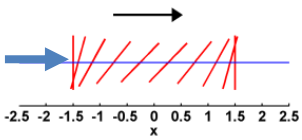

j) $2h_a/c = 3.0, \alpha_a = 45°, \phi = 90°$

Figure 28. Force history and vorticity contours illustrating the vortex formation and interactions during the LEV dominated portion of the stroke (a-c) or wake capture dominated portion of the stroke (d-f) at their respective maximal lift for a 20% strength headwind hover scenario with no freestream. The 3D LEV dominated portion of the stroke is highlighted with z-vorticity contours at two spanwise locations with a 20% freestream in g), h), and i.

Figure 28 (a-c) illustrates highlights the 2D force history and flowfields at maximal lift for the kinematics expressed in Fig. 21j. Immediately apparent is the large impact on the instantaneous as well as time-averaged lift. To clarify, the lift coefficients are still normalized by the maximum translational velocity, i.e. the normalization is independent of the freestream. Flowfields are plotted during the headwind portion of the stroke (backstroke), and show that the headwind case exhibits a more developed and stronger LEV as well as stronger vorticity shedding from the trailing edge. The increased vortical activity created by the headwind, and then interacting with the airfoil in a favorable manner explains qualitatively the increase in performance during the backstroke. But why then the lift peaks during the forward stroke when in the presence of a tailwind?

The rather significant peak in lift is somewhat unexpected, but as will be seen occurs despite the tailwind and not because of it. This peak occurs after stroke reversal as the airfoil interacts with the previously shed wake, or wake-capture dominated portion of the stroke cycle. The hover case temporarily drops off in lift, see Fig. 28d, whereas the 20% freestream case, now a tailwind, continues to increase in lift. Vorticity contours at their respective local maximums in lift, see Fig. 28e and Fig. 28f show a few striking differences, noticeably the strength and position of the previously shed vorticity. Due to the headwind during the backstroke, stronger vortices were created. Now on the return stroke, those vortices' strength, in addition to their position relative to the airfoil, significantly help promote vortex growth, see Fig. 23f. This interaction, resulting in a

temporary enhancement, eventually plays itself out and a decline in lift ensues in what used to be dominated by the LEV, but now amounts to slower relative translational velocity.

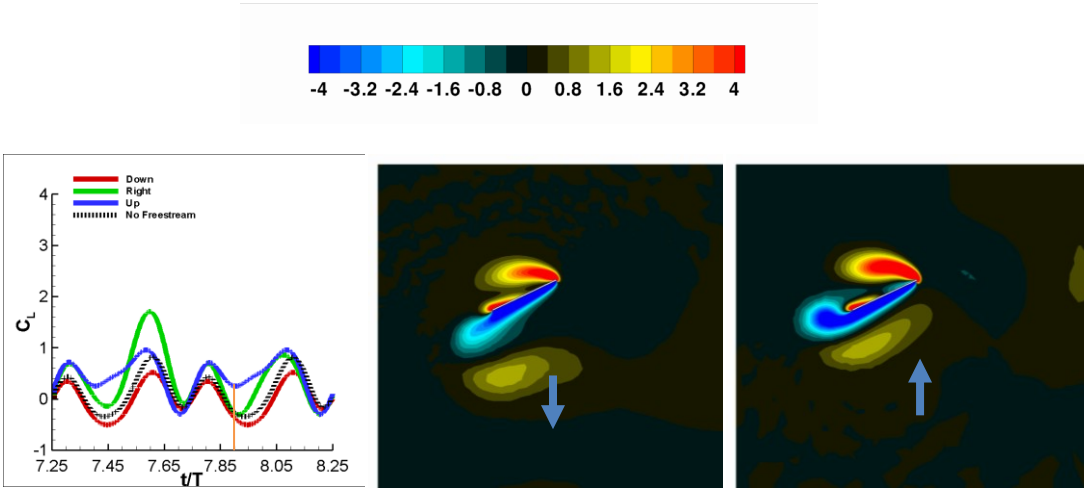

a) $2h_a/c = 3.0, \alpha_a = 80°, \phi = 90°$ **b)** 20% down freestream t/T=7.9 **c)** 20% up freestream; t/T=7.9

Figure 29. Force history (2D) and vorticity contours illustrating the vortex formation between stroke reversal and their respective maximums in lift for b) 20% downward freestream c) 20% upward freestream.

Looking at the 2D force histories again, see Fig. 29a, one will see that the response of a freestream not only depends on the kinematics but also its orientation. For some situations the qualitative nature of the flow doesn't change much over the course of the entire cycle nor are the forces too sensitive, see the vertical freestreams in Fig. 30a, or the downward freestream in Fig. 30c. On the other hand, the horizontal freestream has an appreciable impact for all of these kinematic patterns and specific points are mentioned above. The upward and downward freestreams don't necessarily elicit similar responses in opposite

directions, highlighted in figure 29. This in turn brings into question the relevance of using effective angle of attack in these situations as the nature of the force history may respond more noticeably to the upward freestream than the downward freestream. See figure 30 (a-c) where a 20% freestream imposed from different directions changes the qualitative behavior of the resulting force history significantly.

For all of the synchronized rotation cases (which have positive angles of attack at all times), a 20% downward freestream does indeed decrease the lift and follows from the suppressed vortical activity as the effective angle of attack is lowered. On the other hand some cases have a much more pronounced sensitivity to the upward freestream. Figure 29a illustrates again the force histories for a 20% freestream at various orientations relative to the hover case, as well as the vorticity flowfield, 30b and 30c, for the 20% upward and downward freestream cases at a time where the difference in force history between the two is pronounced. What is seen in Fig. 29b (20% downward freesteam) and Fig. 29c (20% upward freestream) is the increase in LEV and TEV formation as well as a more pronounced interaction with the wake as the upward freestream promotes the growth of the vortex structures and holds the wake in the vicinity for a longer period of time. The non-linear response in lift as the freestream lowers or raises the effective angle of attack is a product of these factors.

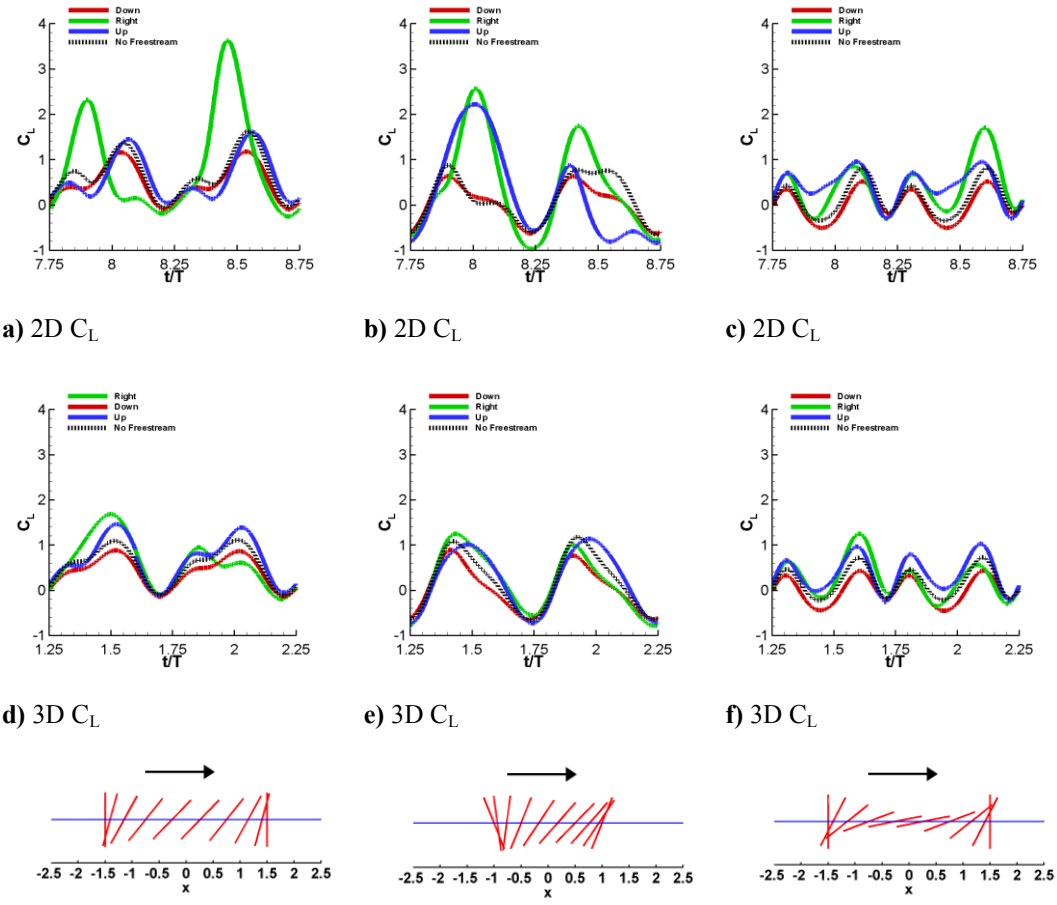

a) 2D C_L **b)** 2D C_L **c)** 2D C_L

d) 3D C_L **e)** 3D C_L **f)** 3D C_L

g) $2h_a/c = 3.0, \alpha_a = 45°$, and $\phi = 90°$ **h)** $2h_a/c = 2.0, \alpha_a = 45°$, and $\phi = 60°$ **i)** $2h_a/c = 3.0, \alpha_a = 80°$, and $\phi = 90°$

Figure 30. 2D (a-c) and 3D (d-f) CL in response to a freestream with a magnitude of 20% of the maximum plunging velocity heading in three distinct directions (down: red, right: green, and up: blue) for three hovering kinematics (g-i). The black dotted line is the reference hovering case.

4.2 Finite Aspect Ratio Wings in a Gust

The 3D cases on the other hand were much less sensitive to the freestream, see figure 30 (d-f). Note however that the scale for the force histories was chosen such that they could be directly compared with the 2D cases and the freestream could be quite influential. The impact was non-negligible for a 20% strength freestream, but overall the nature of the flow was very similar for most cases. The

downward freestream once again degraded lift, and the upward freestream enhanced it albeit to a lesser degree than in the 2D cases.

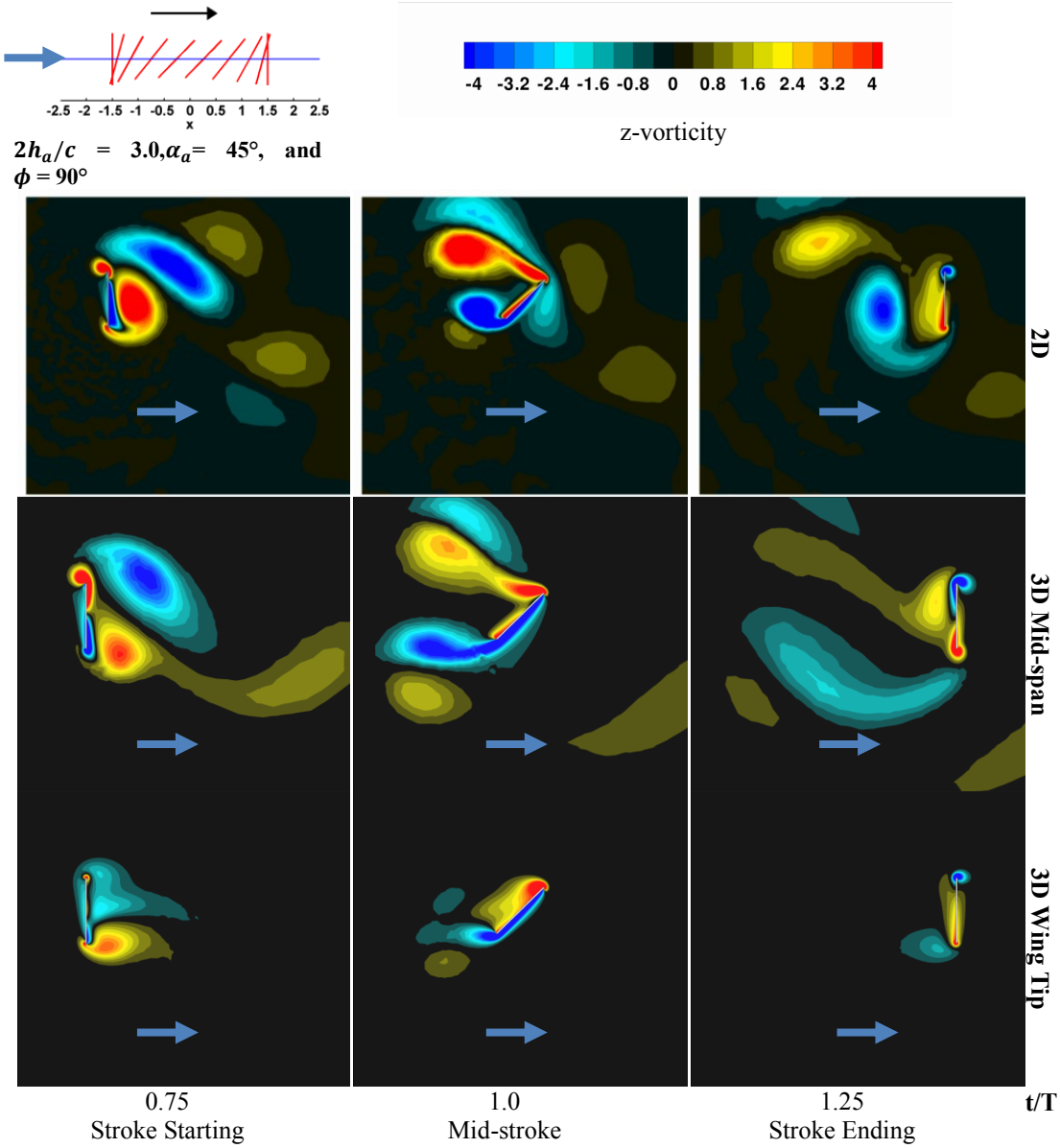

Figure 31. Vorticity contours during beginning, mid, and end-stroke for a 2D flat plate and at mid-span (z/c=0) and wingtip (z/c=1.95) for a 3D flatplate with AR=4 with a 20% freestream tailwind The 3D perspective shots show iso-Q surfaces colored by z-vorticity. The blue arrow denotes freestream direction.

Figure 31 highlights beginning, mid, and end stroke vorticity contours for a 20% freestream tailwind for 2D and at midspan and at the wing tips for 3D. The three-dimensional wing is unable to generate vortices of the same magnitude as the analogous 2D counterparts. This in turn directly impacts the wing's benefit from LEV interactions as well as subsequent interactions with the previously shed wake. The spanwise variation of vorticity exhibited shows a decrease in LEV generation from mid-span to tip, and while the tip vortices are prominent, they do not make up for the weakened LEV formation and wake interaction as experienced in 2D. Figure 28 illustrates the vorticity flowfields during maximal lift, during the headwind, resulting in a 2D lift, figure 28a, almost twice as large as its 3D counterpart, figure 28g.

This discrepancy in sensitivity to freestream between 2D and 3D shows up across the range of kinematic motions. A limited subset of kinematic motions showed very similar force histories in the time averaged sense as well as instantaneously, see section 3.7, when not under the influence of an external freestream. Kinematics in this region of the design space shared low angles of attack across much of the flapping cycle and synchronized rotation, limiting the high angular velocities and angles of attack to the end of the stroke where translational velocity was minimized. This in turn tended to limit vortex size, strength, formation, and influence. As the freestream is introduced, see figure 30c and figure 30f for 2D and 3D force histories in the presence of a 20% freestream, the response is not uniform across the span of the finite wing. The downward

freestream (20% strength) tends to suppress the vortex dynamics and as such the 2D and 3D force histories remain quite similar. The horizontal freestream, most notably during the headwind, and the upward freestream, on the other hand show differences due to the 3D nature of the flow; the reader is referred to Trizila *et al.* (2010) which includes further complementary flowfield examinations not described here. In the absence of a prominent freestream we saw that the 3D effects could accentuate the 2D lift by creating a low pressure zone at the tip and by anchoring an LEV that would otherwise detach earlier from the wing. An interesting question, only partially addressed in the current work due to simulation resources, is to what extent the interplay between kinematic motions and the freestream strength and orientation can be manipulated.

4.3 Surrogate Trends

As has been shown, one useful approach in illustrating a global behavior is the creation of the appropriate surrogate models over a wider swath of the design space. Figure 32 illustrates the time averaged lift as a function of kinematic parameters in the response to a 20% horizontal freestream. Certain trends persist from the hover case with no freestream to the 20% horizontal freestream. Namely the highest time averaged lift values were achieved with kinematics experiencing advanced rotation, $\phi > 90^{\circ}$, at generally high angles of attack, $\alpha_a < 45^{\circ}$. This region depended on dominant vortex interactions and positive angles of attack to start the stroke and these two ideas were accentuated in the presence of a headwind. Similarly, low lift values were found in both scenarios during delayed rotation, $\phi <$

90º, at low angles of attack, $\alpha_a > 45º$. Once again the negative angles of attack and orientation of the wing upon the wake interaction, due to delayed rotation, served in a detrimental manner.

There are significant differences however. Figure 32b and 32d show the difference between the freestream condition and hover for 2D and 3D respectively. As can be seen from the magnitude of the scales, the freestream has a much larger impact on the 2D simulations. Most kinematic combinations in the range studied see an increase in time-averaged lift due to the 20% horizontal freestream; the exceptions are confined to a small region of simultaneous delayed rotation ($\phi<90º$), low AoA ($\alpha_a > 45º$), and shorter plunging amplitudes. Furthermore the biggest impact in the time-averaged 2D and 3D lift is felt for advanced rotations (($\phi<90º$) though the maximal impacts are at higher AoA in 2D and somewhat lower AoA in 3D. Looking at figure 27e we see that the 2D kinematic combinations outperform their analogous 3D counterparts with respect to time-averaged lift. With reference to the immediately preceding sections it was seen that there was generally weaker vortex activity in 3D. This had the effect of weaker delayed stall, but also weaker subsequent wake captures. The 3D cases have a harder time overcoming the losses seen during the tailwind portion of the stroke.

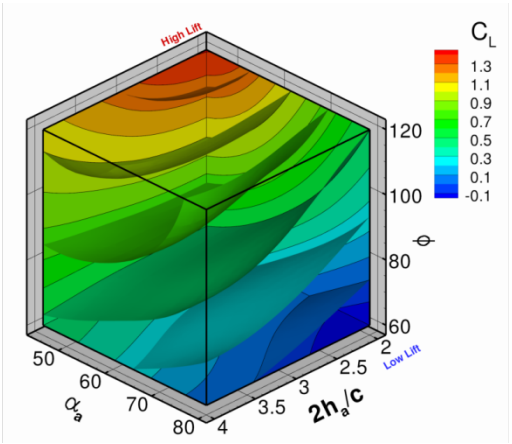

a) 2D lift: 20% horizontal freestream

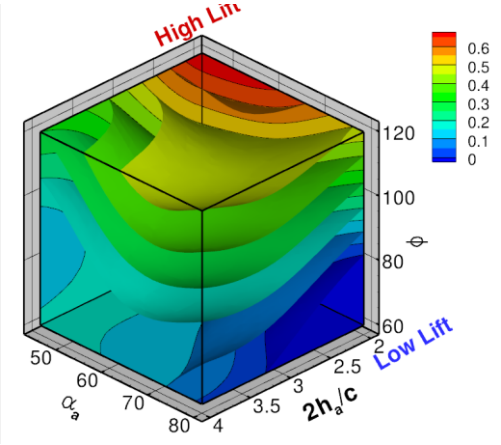

b) 2D lift: 20% freestream - hover

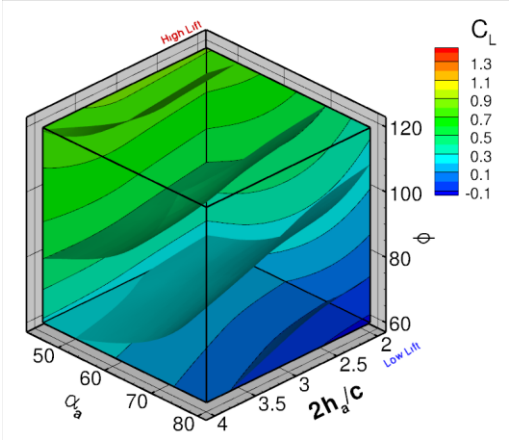

c) 3D lift: 20% horizontal freestream

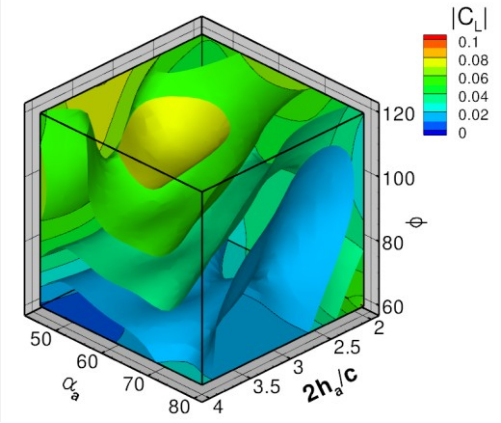

d) 3D lift: 20% freestream - hover

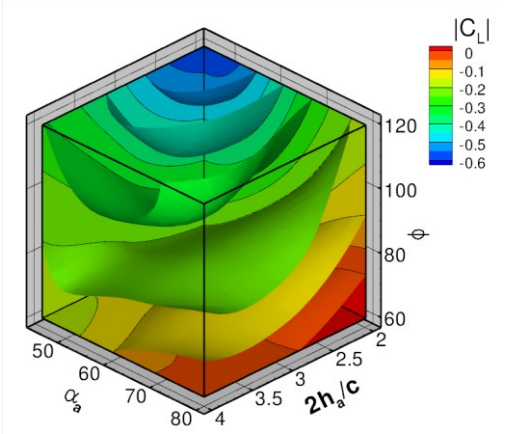

e) Freestream lift: 3D-2D

Figure 32. Surrogate models illustrating the trends in lift in the presence of a 20% horizontal freestream [a) 2D, c) 3D], the differences between freestream and hover [b) 2D, d) 3D], and the difference between 3D and 2D [e].

4.4 On the Applicability of Effective Angle of Attack in Reduced Order Models

To conclude this section, a caution on the use of effective angle of attack, and therefore quasi-steady theories, in the context of hovering flapping wing flight will be illustrated. This is not meant to imply quasi-steady theories are not useful, but rather that the applicability of such a model can be limited and that the context and assumptions of the model should be revisited before applying them in an arbitrary hovering context, i.e. deviating from the kinematic motions expressed in the training of the quasi-steady model can invalidate its usefulness in a seemingly related case.

Figure 33 illustrates the kinematic patterns highlighted in this section under the influence of freestream strengths of 5%, 10%, and 20% in the down, right, and upward directions. The take away message is that within a certain range, an arbitrary value of lift coefficient can be attained for any effective angle of attack. Figure 33 shows, for example that at an effective angle of attack of 45^{o} can yield lift coefficients from approximately -1 to +2.5. The transient and time history effects are not negligible in this context (refer to 1.2.8 for documented successes and difficulties). While some of the quasi-steady models have met success or have been validated in certain circumstances their more general applicability may not be justified.

In the context of hovering, Sane and Dickinson (2002) showed reasonable agreement away from the wake-capture region. For the kinematics in the present study, the rotation of the wing is not as confined to the ends of the stroke, and may have appreciable translational velocity, and their methods of separating the rotational and translating portions of the stroke is not as applicable even away from the wake-capture portion of the cycle. Cases with small to no wake-capture effects and for which the rotation is largely confined to when the translational velocity is minimal would appear to have potential use of quasi-steady theories over the course of an entire flapping cycle. The forward flight applicability is interesting in that some of the assumptions adopted along the way can be broken and yet the quasi-steady models would still appear to have applicability, namely a few cases by Kang *et al.* 2009a. It may be fortuitous cancellation of effects, or it may be that the effects are washed downstream with diminishing impact, and further examination to clarify the region applicability is warranted.

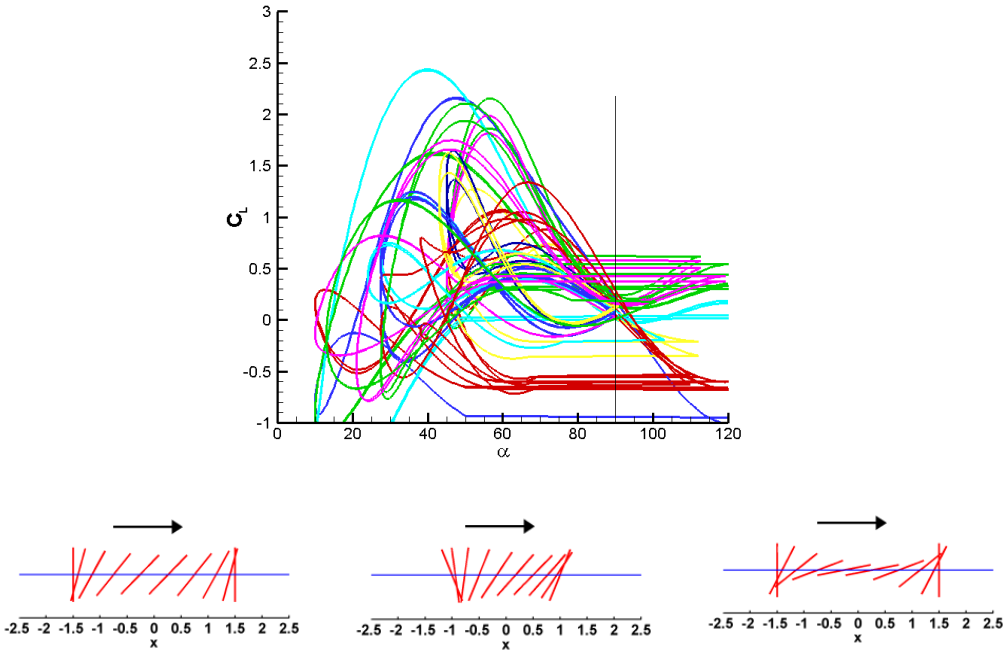

Figure 33. Illustration cautioning the use of effective angle of attack as measure of lift in the hovering context. The lift coefficients of the three kinematic patterns studied in this section have been plotted versus the effective angle of attack for freestream strengths of 5%, 10%, and 20% of the maximum translational velocities with orientations heading down, right, and up.

Chapter 5 Summary, Conclusions, and Recommendations for Future Work

In this study we examined the hovering kinematics of a two-dimensional and three-dimensional flat plate (AR=4) with the aid of surrogate models at a Reynolds number of 100. The analysis of the fluid physics highlighted well known phenomena such as the LEV, as well as identified novel roles for the tip vortices and sustained downward jet that were previously unexplored. The complementary uses of the Navier-Stokes and surrogate models led to the development of a tool that was helpful in the physical analysis of the fluid physics by identifying trends in aerodynamic performance as a function of wing motion, and the quality of the surrogate modeling methodology proved successful in providing computationally cheap and accurate approximations to the time-averaged forces. Different methodologies have been employed previously in the literature to try and achieve this goal in the context of hovering flight with mixed success and applicability. While the computational expense of the Navier-Stokes solutions were O(10-100) cpu hours for each combination of kinematic variables, this data could then be used to train the surrogate models which could predict performance in a fraction of a second and therefore potentially be used in real time calculations for control algorithms. Details are expanded below.

Hover:

Regarding the fluid physics and aerodynamic implications during hover, we observed:

(i) The role of the LEV and associated delayed stall plays a dominant role in the determination of lift in both two- and three-dimensional cases and this is in consensus with the literature (see section 1.1.4). Angle of attack, angular velocity, translational velocity, and translational acceleration all impact the formation and evolution of the LEV. For one of the delayed cases shown, the two-dimensional starting vortices detach causing a weaker LEV during mid-stroke. In the corresponding three-dimensional case, the tip vortices served to anchor the LEV and in the process increased the time-averaged lift. The surrogate models show that this is not a general recipe for higher three-dimensional lift though as most delayed rotation cases at high AoA exhibit higher two-dimensional lift. In general, the advanced rotation cases, especially those with low AoA, were able to benefit from the three-dimensional effects as the lift valley associated with strong downward rotation was much weaker in three dimensions.

(ii) The manifestation of the wake-capture mechanism in the three-dimensional case has been seen to change as the behavior of the shed vortices may differ between two- and three-dimensional cases. This is

illustrated by one case where the shed two-dimensional vortices would remain in the plane of the plunging motion. The three-dimensional counterparts are shed at angles such that they leave plane of the plunging wing and do not collide with the wing upon its return affecting the resulting force histories. This mechanism is also seen to change in relative importance to the LEV impact with changes in kinematics. When the LEV and wake-capture pieces of the cycle were separate, the current sinusoidal pitch-plunge motions showed a larger impact on the force histories from the LEV. On the other hand, Sane and Dickinson (2001, 2002) illustrate similar kinematics about which there is also a flapping about a joint component, and for which the rotation times are localized around the end of the stroke, for which the wake-capture has a noticeably larger impact than the subsequent LEV.

(iii) In two-dimensional cases with higher angles of attack, i.e., lower pitching amplitudes, a persistent downward jet like flow feature was seen to form in the wake sustained by the influence of shed vortices. This was seen experimentally by Freymuth (1990) as well. The jet was absent in the two-dimensional cases with lowest angles of attack as there was also no large scale vortex shedding. In the low aspect ratio three-dimensional case at Re = 100, the presence and influence of an induced jet is not as clear cut. There are pockets of momentum encountered on return strokes, but there is no coherent reverse Karman vortex street reinforcing the jet due to the

more complex three-dimensional vortex interactions. The impact on the instantaneous force history can be significant as demonstrated in section 3.1.1.

(iv) There was significant variance in the spanwise distribution of forces in the three-dimensional cases. Cases which suppressed the LEV and tip vortices, those with the highest angular amplitudes and thus low angles of attack, and small velocity when vertical (e.g. near synchronized hovering) appeared to have a relatively constant response along the span. In contrast, three-dimensional cases with prominent tip vortices exhibited significant variations along the span which did not have a strong correlation to the instantaneous two-dimensional lift values experienced.

(v) At the present Reynolds number (100) the three-dimensional flow physics and tip effects can augment the lift by: a) the presence of a low pressure region near the tip, b) the anchoring of an otherwise shed vortex (in 2D) near the tip, and c) weakening the pocket of downward momentum encountered on a return stroke. A competing effect is the induced downwash of tip vortex and the reduced effective angle of attack along the span, serving to reduce lift.

(vi) The competition of effects between rapid pitching motions, their timing, and subsequent LEV generation would suggest that (non-sinusoidal) kinematics achieving better lift performance may be achieved by confining the downward rotation to the end of the stroke while balancing

the desire for high AoA and increasing AoA during the stroke cycle to generate and sustain LEVs. Lift and drag will still compete as higher angles of attack will increase the drag and the generation of the vortices, but the trade-offs between the two can be modified.

Environmental Sensitivity:

As flapping wing frequencies are typically an order of magnitude or two faster than that of environmental perturbations, gusts can be modeled as a constant freestream for many practical applications.

(i) The sensitivity to the gust for selected kinematic parameters was largely determined by how much influence it had on the vortex dynamics. Headwinds with a modest 20% strength could significantly enhance the LEV generation and this in turn provided stronger wake interactions on the return stroke. For most kinematic motions, within the ranges studied, a 20% horizontal freestream increased the 2D lift despite half of the stroke experiencing a tailwind.

(ii) The 3D cases, while still affected appreciably, were noticeably less sensitive to gusts than their 2D counterparts due to the weakened vortex dynamics generally occurring in 3D.

(iii) The impact of a gust was tied to its strength, orientation, and what kinematics it encountered. Those flows affected by the gust saw the manifestation through its role in LEV, tip vortex, and wake generation and

interaction. Those kinematics with little of the aforementioned vortex dynamics saw the smallest sensitivity to the gust.

(iv) By changing the effective angle of attack on select kinematic motions with various freestream orientations and strengths, different values at the same effective angle of attacks were obtained. Hence a cautionary note on the application of quasi-steady models in the hovering context is warranted.

Surrogate Modelling:

Often as case studies in the literature are performed, or independent variables varied in a parametric study, it can become difficult to place the findings in the proper context thus making it difficult to glean the relevant information and compare with findings of other researchers. The surrogate process more readily illuminates the global perspective of variables' impact as well as the limitations of the findings, making identification of the applicability much more apparent. The surrogate modeling techniques provided a useful method for approximating otherwise computationally expensive simulations without sacrificing fidelity. Meanwhile they proved an efficient method for analyzing trends seen throughout the design space and possible points of interest. Coupled with instantaneous force histories and flow field measurements they can provide insight to the complex interplay of the physical mechanisms involved. The surrogate modeling techniques further revealed that:

(i) The weighted average surrogate agreed well at the independent test points. While the number of independent test points was limited, the error was often less than a few percent. The maximum error, based on time-averaged lift values, that was found was less than 15%. The agreement shows promise for using surrogates, namely weighted average surrogates, as a reduced order model for complex engineering design in the MAV context.

(ii) The hierarchy of variable sensitivity in the time averaged lift changed between two-dimensional and three-dimensional hover. In two-dimensions the importance was 1) angular amplitude 2) phase lag and 3) plunging amplitude. In three-dimensions the hierarchy switches to 1) phase lag 2) angular amplitude and 3) plunging amplitude. This is in large part from the tip vortices in three-dimensional simulations not suffering as large a penalty from the lift valley that would occur between wake-capture and delayed stall. This difference in two-dimensions and three-dimensions is partially attributed to the reduced influence of the jet interaction in three-dimensional simulations.

(iii) Interestingly, the approximation to the power required remained largely the same between two-dimensional and three-dimensional design spaces. This implies that the unsteady effects which influence the drag can in some contexts be reduced down to their two-dimensional counterparts. Note that the pressure force, and not the viscous force, was still the dominant component of the drag felt.

(iv) Regions for which 2D kinematics outperformed 3D in hover and vice-versa were identified. Furthermore the density of points near the Pareto front was higher in three dimensions implying more design variable combinations that are close to optimal in terms of power and lift trade-offs. In the study of Sane and Dickinson (2001), consistent conclusions are reached for obtaining optimal lift, e.g., keep fairly high angles of attack for as much of the stroke as possible. There are differences though in the sensitivity to plunging amplitude, which was small in the current study, but was relevant in the flapping about a joint method employed in their study.

Further Work:

A few closely related topics which would prove valuable in the understanding of flapping wing flight:

(i) How can the shape of the wing be constructed to elicit favorable fluid dynamics? There has been some effort to look at corrugated cross-sections (often cited as motivated by dragonflies) and a small study in the appendix on ellipse versus flatplate. Perhaps more importantly, in light of the findings in the current studies, how can the wing planform be manipulated to increase performance? It was seen that certain combinations of kinematic parameters could utilize the 3D effects, namely the tip vortices. For instance could the trailing edge be tapered as to elicit a vortex which would not only create a low pressure region, but not interfere with LEV

development? The impact of AR would fall into this category. It was shown that due to the competition of influences the tip vortices had, they could be used beneficially. The tip effects would likely become stronger as the AR decreases. Can lower aspect ratio wings, which would likely be easier to maneuver considering the moment of inertia, utilize the 3D effects more efficiently? On the other hand the higher aspect ratio wings are likely to have a more pronounced LEV which was seen to be the dominant flow feature in the current context.

(ii) The kinematics in the current hovering studies were confined to sinusoidal pitching and plunging motions. Due to the approach, however, insight was gained on what fluid dynamics caused the observed performance. In this fashion the conclusions can be generalized somewhat if put in the context of the dominant unsteady mechanisms that were generated or suppressed. One aspect not addressed is how the centripetal accelerations introduced by pivoting about a point, like a bird flapping about its shoulder joint, effect these unsteady mechanisms. The literature has isolated studies of a few kinematic patterns but it was not seen to have expressed the knowledge of what should be desired/avoided when introducing this degree of freedom. Particularly how is the LEV generation and growth impacted? What is the role of the resulting tip vortices? The eventual question is how does one optimally move the wing to meet a certain

requirement. The intermediate question involves understanding of how to utilize beneficial unsteady mechanisms or suppress detrimental ones.

(iii) An emphasis of the current study is how the vortex dynamics are impacted by the kinematic motions that created them. Answering these questions first necessitates precisely quantifying a vortex which can be more nuanced as a quantity such as vorticity doesn't offer a way to differentiate between rotation and sheer (see 1.1.8). One natural extension is to systematically examine how the Reynolds number affects the aerodynamic performance which is again dependent on the kinematic motions. A different but related question involves the role of turbulence and what role it plays at the higher Reynolds numbers which is again a function of the kinematics, i.e. isolated studies of a single motion or small subset of kinematic motions are not equipped to generalize the conclusions past the specific constraints of the study.

(iv) Alluded to in the literature review was the influence that aeroelasticity of the wing has in determining the fluid physics and aerodynamic forces. Examples of flexible structures outperforming their rigid counterparts were given, as were examples where too much flexibility decreased performance. The idea that flexibility can provide a boost in performance, e.g. by increasing force production or decreasing power consumption, has been established. The questions here revolve around how to make use of this idea. How does one introduce flexibility into the wing (and to what

degree) such that the unsteady mechanisms are controlled, e.g. keeping the flow attached, generating stronger LEVs, shedding vortices at the time and orientation of the designer's choosing, etc.?

Appendix

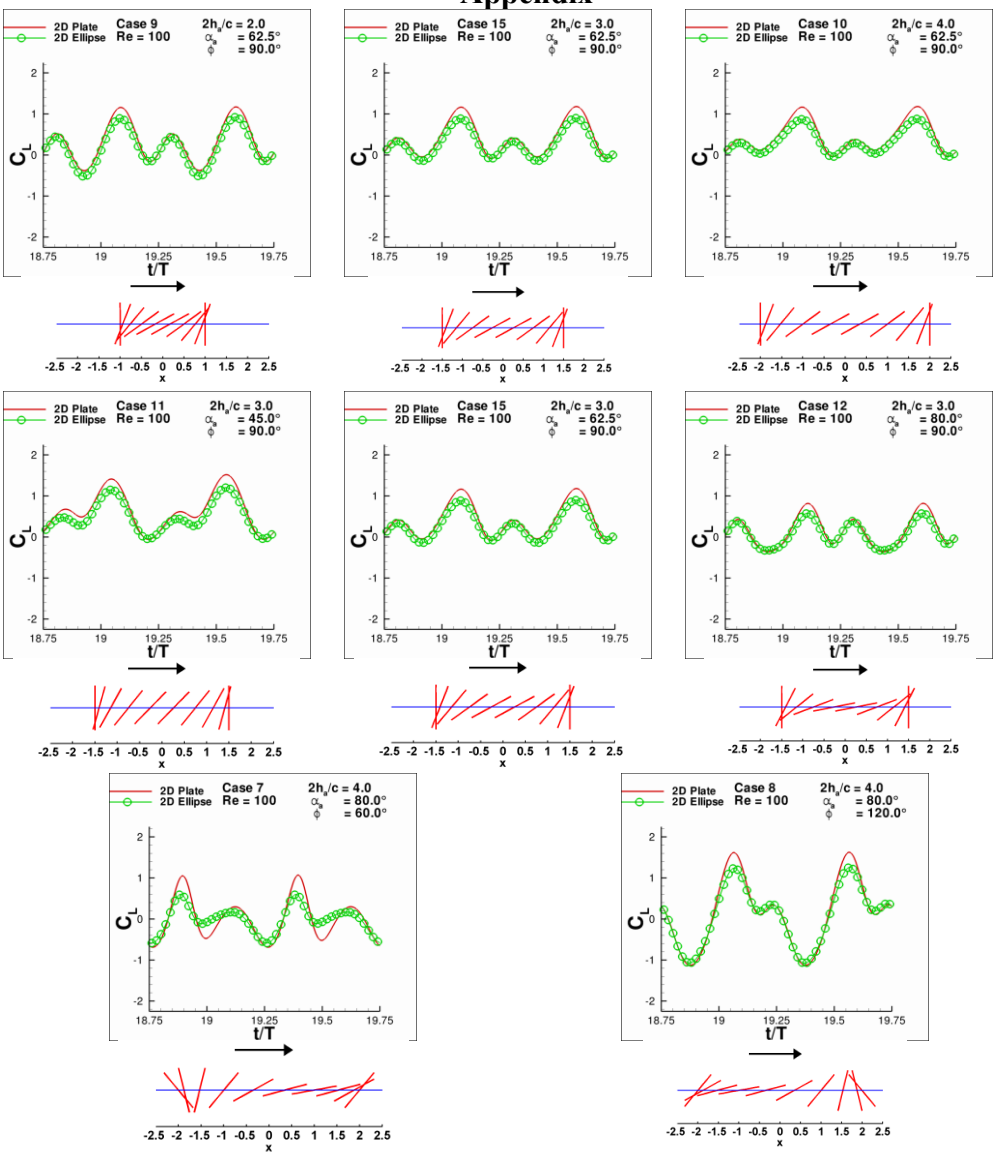

(a)

(b)

(c)

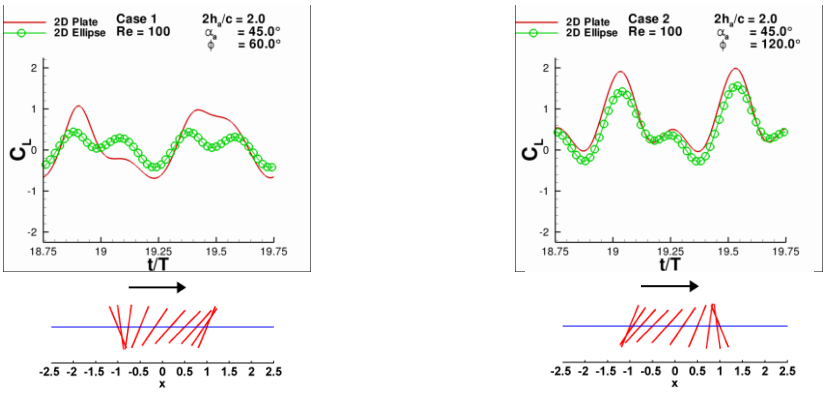

(d)

FIGURE 34. Time histories of the lift and drag coefficients between a two-dimensional ellipse of 15% thickness and two-dimensional flatplate for selected cases (a) as $2h_a/c$ is increases from 2.0 (left) to 4.0 (right) holding α_a= 62.5° and ϕ=90° (b) as α_a is increased from 45° (left) to 80° (right) while holding $2h_a/c$ =3.0 and ϕ=90° (c) examining delayed rotation ϕ=60° (left) and andvanced rotation ϕ=120° (right) while holding $2h_a/c$ =4.0 α_a= 80° (d) examining delayed rotation ϕ=60° (left) and andvanced rotation ϕ=120° (right) while holding $2h_a/c$ =2.0 α_a= 45°.

Bibliography

- Agrawal A, Agrawal SK. 2009 Design of bio-inspired flexible wings for flapping wing micro-sized air vehicle applications. *Adv Robot* **23**, 979-1002.

- Altshuler DL, Princevac M, Pan H, Lozano J. 2009 Wake patterns of the wings and tail of hovering hummingbirds. *Exp Fluids* **46**, 835-846.

- Altshuler DL, Dickson WB, Vance JT, Roberts SP, Dickinson MH. 2005 Short-amplitude high-frequency wing strokes determine the aerodynamics of honeybee flight. *Proc Natl Acad Sci* **102**, No. 50, 18213-18218.

- Althsuler DL, Dudley R, Ellington CP. 2004 Aerodynamic forces of revolving hummingbird wings and wing models. *J Zool Lond* **264**, 327-332.

- Anderson JD. 2006 *Fundamentals of aerodynamics*. 4th ed. New York McGraw Hill Higher Education.

- Anderson JM, Streitlin K, Barrett DS, Triantafyllou MS. 1998 Oscillating foils of high propulsive efficiency. *J Fluid Mech* **360**, 41-72.

- Ansari SA, Knowles K, Zbikowski R. 2008 Insectlike flapping wings in the hover part 2 effect of wing geometry. *J Aircraft* **45**, No. 6, 1976-1990.
- Ansari, S.A., Zbikowski, R. & Knowles, K. 2006 Aerodynamic Modeling of Insect-like Flapping Flight for Micro Air Vehicles. *Progress in Aerospace Sciences* **42**, 129-172.
- Aono H, Chimakurthi SK, Wu P, Sallstrom E, Stanford BK, Cesnik CES, et al. 2010 A computational and experimental study of flexible flapping wing aerodynamics. AIAA-Paper 2010-554.
- Aono H, Shyy W, Liu H. 2009 Near wake vortex dynamics of a hovering hawkmoth. *Acta Mech Sin* **25**, 23-36.
- Baik YS, Raush J, Bernal L, Shyy W, Ol M. 2010 Experimental Study of Governing Parameters in Pitching and Plunging Airfoil at Low Reynolds Number. 48th AIAA Aerospace Sciences Meeting Including the New Horizons Forum and Aerospace Exposition, AIAA 2010-388.
- Baik YS, Rausch JM, Bernal LP, Ol MV. 2009 Experimental investigation of pitching and plunging airfoils at Reynolds number between 1×104 and 6×104. 39th AIAA Fluid Dynamics Conference, AIAA 2009-4030.
- Birch JM, Dickson WB, Dickinson MH. 2004 Force production and flow structure of the leading edge vortex on flapping wings. *J Exp Biol* **207,** 1063-1072.

- Birch JM, Dickinson MH. 2003 The influence of wing-wake interactions on the production of aerodynamic forces in flapping flight. *J Exp Biol*, 2257-2272.

- Birch JM, Dickinson MH. 2001 Spanwise flow and the attachment of the leading-edge vortex on insect wings. *Nature* **412**, 729-733.

- Blazek, J. 2001 *Computational Fluid Dynamics: Principles and Applications*. Elsevier.

- Bohl DG, Koochesfahani MM. 2009 MTV measurements of the vortical field in the wake of an airfoil oscillating at high reduced frequency. *J Fluid Mech* **620**, 63-88.

- Bomphrey RJ, Taylor GK, Thomas ALR. 2009 Smoke visualization of free-flying bumblebees indicates independent leading-edge vortices on each wing pair. *Exp Fluids* **46**, 811-821.

- Bomphrey RJ. 2006 Insects in flight direct visualization and flow measurements. *Bioinsp Biomim* **1**, 1-9.

- Bomphrey RJ, Lawson NJ, Harding NJ, Taylor GK, Thomas ALR. 2005 The aerodynamic of Manduca sexta digital particle image velocimetry analysis of the leading-edge vortex. *J Exp Biol* **208**, 1079-1094.

- Bos FM, Lentik D, van Oudheusden BW, Bijl H. 2008 Influence of wing kinematics on aerodynamic performance in hovering insect flight. *J Fluid Mech* **594**, 341-368.

- Brachenbury J. 1990 Wing movements in the bush cricket *Tettigonia viridissima* and the mantis *Ameles spallanziana* during natural leaping. *J Zoology Long* **220**, 593-602.

- Brodsky AK. 1991 Vortex formation in the tethered flight of the peacock butterfly *Inachis Io* L and some aspects of insect flight evolution. *J Exp Biol* **161,** 77-95.

- Broering TM, Lian Y. 2010 Numerical study of two flapping airfoils in tandem configuration. 48th AIAA Aerospace Sciences Meeting Including the New Horizons Forum and Aerospace Exposition, AIAA 2010-865.

- Buchholz JH, Smits AJ. 2008 The wake structure and thrust performance of a rigid low-aspect-ratio pitching panel. *J Fluid Mech* **603**, 331-365.

- Calderon DE, Wang Z, Gursul I. 2010 Lift enhancement of a rectangular wing undergoing a small amplitude plunging motion. 48th AIAA Aerospace Sciences Meeting Including the New Horizons Forum and Aerospace Exposition, AIAA 2010-386.

- Cheng, B. & Titterington, D.M. 1994 Neural Networks: a Review from a Statistical Perspective. *Statistical Science* **9**, 2-54.

- Cleaver DJ, Wang Z, Gursul I. 2010 Vortex mode bifurcation and lift force of a plunging airfoil at low Reynolds Numbers. 48th AIAA Aerospace Sciences Meeting Including the New Horizons Forum and Aerospace Exposition, AIAA 2010-390.

- Cloupeau M, Devilliers JF, Devezeaux D. 1979 Direct measurements of instantaneous lift in desert locust; comparison with Jensen's experiments on detached wings. *J Exp Biol* **80**, 1-15.

- Cooter RJ, Baker PS. 1977 Weis-Fogh clap and fling mechanisms in Locusta. *Nature* **269**, 53-54.

- Combes SA. 2002 Wing flexibility and design for animal flight. Ph.D. Dissertation, University of Washington, 2002.

- Combes SA & Daniel TL. 2003a Into thin air: contributions of aerodynamic and inertial-elastic forces to wing bending in the hawkmoth Manduca sexta. *J Exp Biol* **23**, 2999-3006.

- Combes SA & Daniel TL. 2003b Flexural stiffness in insect wings I. Scaling and the influenceof wing venation. *J Exp Biol* **206**, 2979-87.

- Combes SA & Daniel TL, 2003c Flexural stiffness in insect wings II. Spatial distribution and dynamic wing bending. *J Exp Biol* **206,** 2989-97.

- Dabiri JO. 2009 Optimal vortex formation as a unifying principle in biological propulsion. *Ann Rev Fluid Mech* **41**, No. 1, 17-33.

- Dalton S. 2006 *The miracle of flight*. London: Merrell.

- Daniel TL, Combes SA. 2002 Flexible wings and fins: bending by intertial or fluid-dynamic forces? *integr Comp Biol* **42**, 1044-9.

- Dickinson MH, Lehmann F-O, Sane SP. 1999 Wing rotation and the aerodynamic basis of insect flight. *Science* **284**, No. 5422, 1954-1960.

- Dickinson MH. 1994 The effects of wing rotation on unsteady aerodynamic performance at low Reynolds numbers. *JEB* **192**, 179-206.

- Dickson WB, Dickinson MH. 2004 The effect of advance ratio on the aerodynamics of revolving wings. *J Exp Biol* **207**, 4269-4281.

- Dong H, Liang Z. 2010 Effects of ipsilateral wing-wing interactions on aerodynamic performance of flapping wings. Proceedings of 48th AIAA Aerospace Sciences Meeting Including the New Horizons Forum and Aerospace Exposition, AIAA 2010-71.

- Drzewiecki S. 1920 *Theorie generale de l'helice.*

- Du G & Sun M. 2008 Effects of unsteady deformation of flapping wing on its aerodynamic forces. *Appl Math Mech* **29**, No. 6, 196-204.

- Dudley R, Ellington CP. 1990 Mechanics of Forward Flight in Bumblebees II. Quasi-Steady Lift and Power Requirements. *J Exp Biol* **148**, 53-88.

- Ellington, C.P 1999 Novel Aerodynamics of Insect Flight: Applications to Micro-Air Vehicles. *Jornal of Experimental Biology* **202**, 3439-3448.

- Ellington CP, van den Berg C, Willmott AP, Thomas ALR. 1996 Leading-edge vortices in insect flight. *Nature* **384**, 626-630.

- Ellingtong CP. 1984 The aerodynamics of hovering insect flight. I. The quasi-steady analysis. *Phil Trans R Soc Lond B* **305**, 1-15.

- Ellington CP. 1984 The aerodynamics of hovering insect flight. IV. Aerodynamic mechanics. *Phil Trans R Soc Lond B* **305**, 113.

- Ennos AR. 1989 Inertial and aerodynamic torques on the wings of Diptera in flight. *J Exp Biol* **142**, 87-95.

- Ennos AR. 1988a The importance of torsion in the design of insect wings. *J. Exp Biol* **140**, 137-160.

- Ennos AR. 1988b The inertial cause of the wing rotation in Diptera. *J Exp Biol* **140**, 161-169.

- Ennos AR. 1987 A comparative study of the flight mechanism of Diptera. *J Exp Biol* **127**, 355-372.

- Fearing R.S., Chiang, K.H., Dickinson M., Pick, D.L, Sitti, M. & Yan, J. 2000 Wing Transmission for a Micromechanical Flying Insect. *IEEE International Conference on Robotics and Automation,* 1509-1515.

- Freymuth P. 1990 Thurst generation by an airfoil in hovermodes. *Experiments in Fluids* **9**, 17-24.

- Fry SN, Sayaman R, Dickinson MH. 2005 The aerodynamics of hovering flight in Drosophila. *J Exp Biol* **208**, 2303-2318.

- Fry SN, Sayaman R, Dickinson MH. 2003 The aerodynamics of free-flight Maneuvers in Drosophila. *J. Exp. Biol.* **300**, 495-498.

- Garland K, Ol M, Bernal L, Kast S. 2010 Experiments on Free-to-Pivot Hover Motions of a Flat Plate. AIAA-Paper 2010-4456.

- Gharib M, Rambod E, Shariff K. 1998 A universal time scale for vortex ring formation. *J Fluid Mech* **360**, 121-140.

- Godoy-Diana R, Marias C, Aider J-L, Wesfried JE. 2009 A model for the symmetry breaking of the reverse Benard-von Karman vortex street produced by a flapping foil. *J Fluid Mech* **622**, 23-32.

- Godoy-Diana R, Aider J-L, Wesfried JE. 2008 Transitions in the wake of a flapping foil. *Phys Rev E* **77**, 016308-1-016308-5.

- Goel, T., Haftka, R.T., Shyy, W. & Queipo, N.V. 2007 Ensemble of Surrogates. *Structural and Multidisciplinary Optimization* **33**, No. 3.

- Gogulapati A, Friedmann P, Kheng E, Shyy W. 2010 Approximate Aeroelastic Modeling of Flapping Wings: Comparisons with CFD and Experimental Data. AIAA-Paper 2010-2707.

- Gogulapati A, Friedmann P, Shyy . 2008 Nonlinear Aeroelastic Effects in Flapping Wing Micro Air Vehicles AIAA-Paper 2008-1817

- Green MA, Smith AJ. 2008 Effects of three-dimensionality on thrust production by a pitching panel. *J Fluid Mech* **615**, 211-220.

- Green MA, Rowley CW, Haller G. 2007 Detection of Lagrangian coherent structures in three-dimensional turbulence. *J Fluid Mech.* **572**, 111-120.

- Hamamoto M, Ohta Y, Hara K, Hisada T. 2007 Application of fluid-structure interaction analysis to flapping flight of insects with deformable wings. *Adv Robot* **21**, 1-21.

- Heathcote S, Martin D, Gursul I. 2004 Flexible flapping airfoil propulsion at zero freestream velocity. *AIAA J* **42**, No. 11, 2196-204.

- Hedenström A, Muijres FT, von Busse R, Johansson LC, Winter Y, Spedding GR. 2009 High-speed stereo PIV measurement of wakes of two bat species flying freely in a wind tunnel. *Exp Fluids* **46**, 923-932.

- Hedenström A, Johansson LC, Wolf M, von Busse R, Winter Y, Spedding GR. 2007 Bat flight generates complex aerodynamic tracks. *Science* **316**, 894-897.

- Hedrick TL. 2008 Software techniques for two- and three-dimensional kinematic measurements of biological and biomimetic systems. Bioinsp Biomim **3**, 1-6.

- Ho, S., Nassef, H., Pornsin-Sirirak, N., Tai, Y.C. & Ho, C.M. 2003 Unsteady Aerodynamics and Flow Control for Flapping Wing Flyers. *Progress in Aerospace Sciences* **39**, No. 8, 635-681.

- Hong YS, Altman A. 2008 Lift from spanwise flow in simple flapping wings. *J Aircraft* **45**, No. 4, 1206-1216.

- Hong YS, Altman A. 2007 Streamwise vorticity in simple mechanical flapping wings. *J Aircraft* **44** , No. 5, 1588-1597.

- Hover FS, Haugsdal Ø. Triantafyllou MS. 2004 Effect of angle of attack profiles in flapping foil propulsion. *J Fluid Struct* **19**, 37-47.

- Hsieh CT, Chang CC, Chu CC. 2009 Revisiting the aerodynamics of hovering flight using simple models. *J Fluid Mech* **623**, 121-148.

- Hubel TY, Hristov NI, Swart SM, Breuer KS. 2009 Time-resolved wake structure and kinematics of bat flight. *Exp Fluids* **46**, 933-943.

- Hui H, Kumar AG, Abate G, Albertani R. 2009 An experimental study of flexible membrane wings in flapping flight AIAA-Paper 2009-876

- Hunt, J.C.R., Wray, A.A. & Moin, P. 1988 Eddies, Streams, and Convergence Zones in Turbulent Flows. *Report CTR-S88* Center for Turbulence Research.

- Isaac KM, Rolwes J, Colozza A. 2008 Aerodynamic of a flapping and pitching wing using simulations and experiments. *AIAA J* **46**, No. 6, 1505-1515.

- Ishihara D, Horie T, Denda M. 2009 A two-dimensional computational study on the fluid-structure interaction cause of wing pitch changes in dipteran flapping flight. *J Exp Biol* **212,** 1-10.

- Jardin T, David L, Farcy 2009 A. Characterization of vortical structures and loads based on time-resolved PIV for asymmetric hovering flapping flight. *Exp Fluids* **46**, 847-857.

- Jensen M. 1956 Biology and physics of locust flight. III. The aerodynamisof locust flight *Phil. Trans. R. Soc. Lond. B* **239**, 511-552.

- Jones AR, Babinsky H. 2010 Three-dimensional effects of a waving wing. 48th AIAA Aerospace Sciences Meeting Including the New Horizons Forum and Aerospace Exposition, AIAA 2010-551.

- Kamakoti, R., Thakur, S., Wright, J., and Shyy, W. 2006 Validation of a new parallel all-speed CFD code in a rule-based framework for multidisciplinary applications. AIAA 2006-3063.

- Kang C, Baik Y, Bernal L, Ol MV, Shyy W. 2009a Fluid Dynamics of Pitching and Plunging Airfoils of Reynolds Number between $1x10^4$ and $6x10^4$. AIAA-Paper 2009-536

- Kang C, Aono H, Trizila P, Baik YS, Rausch JM, Bernal LP, Ol MV, Shyy W. 2009b Modeling of pitching and plunging airfoils at Reynolds number between 1×104 and 6×104. Proceeding of 39th AIAA Fluid Dynamics Conference, AIAA 2009-4100.

- Katz J, Plotkin A. 2001 *Low-speed aerodynamics*. 2nd ed. New York. Cambridge University Press.

- Kim D-K, Han J-H, Kwon K-J. 2009 Wind tunnel tests for a flapping wing model with a changeable camber using macro-fiber composite actuators. *Smart Mater Struct* **18**, 024008-1-8.

- Kim W-K, Ko JH, Park HC, Byun D. 2009 Effects of corrugation of the dragonfly wing on gliding performance. *J Theor Biol* **260**, 523-530.

- Kurtulus DF, David L, Farcy A, Alemdaroglu N. 2008 Aerodynamic characteristics of flapping motion in hover. *Exp Fluids* **44**, 23-36.

- Lai JCS, Platzer MF. 1999 Jet characteristics of a plunging airfoil. *AIAA J* **37**, No. 12, 1529-1537.

- Lee J-S, Kim J-H, Kim C. 2008 Numerical study on the unsteady-force-generation mechanism of insect flapping motion. *AIAA J* **46**, No. 7, 1835-1848.

- Lehmann F-O. 2009 Wing-wake interaction reduces power consumption in insect tandem wings. *Exp Fluids* **46**, 765-775.

- Lehmann F-O, Pick S. 2007 The aerodynamic benefit of wing-wing interaction depends on stroke trajectory in flapping insect wings. *J Exp Biol* **210**, 1362-1377.

- Lehmann F-O, Sane SP, Dickinson MH. 2005 The aerodynamic effects of wing-wing interaction in flapping insect wings. *J Exp Biol* **208**, 3075-3092.

- Lehmann FO. 2004 The mechanisms and lift enhancement in insect flight *Naturwisenschafen*.

- Lentink, D., Bradshaw, N. & Jongerius, S.R. 2007 Novel Micro Aircraft Inspired by Insect Flight. *Comparitive Biochemistry and Physiology A-Molecular & Integrative Physiology* **146**, No. 4, 133-134.

- Lentink D, Gerritsma M. 2003 Influence of airfoil shape of performance in insect flight. Proceeding of 33rd AIAA Fluid Dynamics Conference and Exhibit, AIAA 2003-3447.

- Lesoinne M, Farhat C. 1996 Geometric conservation laws for flow problems with moving boundaries and deformable meshes, and their impact on aeroelastic computations. *Comput Method Appl M* **134**, 71-90.

- Levy D-E, Seifert A. 2009 Simplified dragonfly airfoil aerodynamics at Reynolds numbers below 8000. *Phys Fluids* **21**, 071901-1-071901-17.

- Lewing GC, Haj-Hariri H. 2003 Modeling thrust generation of a two-dimensional heaving airfoil in a viscous flow. *J Fluid Mech* **492**, 339-362.

- Liang Z, Dong H, Wei M. 2010 Computational Analysis of Hovering Hummingbird Flight. 48th AIAA Aerospace Sciences Meeting Including the New Horizons Forum and Aerospace Exposition, AIAA 2010-555.

- Lipinski D, Mohseni K. 2009 Flow structures and fluid transport for the hydromedusae Sarsia tubules and Aequorea Victoria. *J Exp Biol* **212**, 2436-2447.

- Liu H, Aono H. 2009 Size effects on insect hovering aerodynamics: an integrated computational study. *Bioinsp Biomim* **4**, 1-13.

- Liu H. 2009 Integrated modeling of insect flight: from morphology, kinematics to aerodynamics *J. Comput Phys* **228**, No. 2, 439-59.
- Liu H. 2005 Simulation-based biological fluid dynamics in animal locomotion. *Appl Mech Rev* **58**, 269-282.
- Liu H. 2002 Computational biological fluid dynamics: digitizing and visualizing animal swimming and flying. **42**, No. 5, 1050-1059.
- Liu H, Kawachi K. 1997 A numerical study of insect flight. *J Comput Phys* **146**, No. 1, 124-156.
- Lu Y, Shen GX. 2008 Three-dimensional flow structure and evolution of the leading-edge vortices on a flapping wing. *J Exp Biol* **211**, 1221-1230.
- Lua KB, Lim TT, Yeo KS. 2008 Aerodynamic forces and flow fields of a two-dimensional hovering wing. *Exp Fluids* **45**, 1047-1065.
- Lu Y, Shen GX, Su WH. 2007 Flow visualization of dragonfly hovering via an electromechanical model. *AIAA J* **45**, No. 3, 615-623.
- Lua KB, Lim TT, Yeo KS, Oo GY. 2007 Wake-structure formation of a heaving two-dimensional elliptic airfoil. *AIAA J* **45**, No. 7, 1571-1583.
- Luke, E.A. & George, T. 2005 Loci: A Rule-Based Framework for Parallel Multi-Disciplinary Simulation Synthesis. *Journal of Functional Programming* **15**, No. 3, 477-502.

- Luo G, Sun M. 2005 The effects of corrugation and wing planform on the aerodynamic force production of sweeping model insect wings. *Acta Mech Sin* **21**, 531-541.

- Maybury WJ, Lehmann F-O. 2004 The fluid dynamics of flight control by kinematic phase lag variation between two robotic insect wings. *J Exp Biol* **207**, 4707-4726.

- Menter FR. 1993 Two equation eddy-viscosity turbulence models for engineering applications. *AIAA J* **32**, 269-289.

- Michelin S & Smith SGL. 2009 Resonance and propulsion performance of a heaving flexible wing. *Phys Fluids* **21**, 071902-1-15.

- Miettinen KM. 1999 *Nonlinear Multiobjective Optimization*, Kluwer Academic Publisher, Boston.

- Milano M, Gharib M. 2005 Uncovering the physics of flapping flat plates with artificial evolution. *J Fluid Mech* **534**, 403-409.

- Miller LA, Peskin CS. 2009 Flexible clap and fling in tiny insect flight. *J Exp Biol* **212**, 3076-90.

- Miller LA, Peskin CS. 2005 A computational fluid dynamics of 'clap and fling' in the smallest insects. *J Exp Biol* **208**, 195-212.

- Miller LA, Peskin CS. 2004 When vortices stick: an aerodynamic transition in tiny insect flight. *J Exp Biol* **207**, 3073-3088.

- Muijres FT, Johansson LC, Barfield R, Wolf M, Spedding GR, Hedenström 2008 A. Leading-edge vortex improves lift in slow-flying bats. *Science* **319**, 1250-1253.

- Mueller D, Bruck HA, Gupta SK. 2009 Measurement of thrust and lift forces associated with the drag of compliant flapping wing for micro air vehicles using a new test stand design. *Exp Mech*, 1-11.

- Mueller, T.J. & DeLaurier, J.D. 2003 Aerodynamics of Small Vehicles. *Annual Review of Fluid Mechanics* **35**, 89-111.

- Myers, R.H. & Montgomery, D.C. 2002 *Response Surface Methodology: Process and Product Optimization Using Designed Experiments.* Wiley.

- Nagai H, Isogai K, Fujimoto T, Hayase T. 2009 Experimental and numerical study of forward flight aerodynamics of insect flapping wing. *AIAA J* **47**, No. 3, 730-742.

- Norberg, U.M.L. 2002 Structure, Form, and Function of Flight in Engineering and the Living World. *Journal of Morphology* **252**, No. 1, 52-81.

- Ol et al. 2009a Unsteady aerodynamics for micro air vehicles. RTO AVT-149 report, 1-145.

- Ol MV, Bernal L, Kang C, Shyy W. 2009b Shallow and deep dynamic stall for flapping low Reynolds number airfoils. *Exp Fluids* **46**, 883-901.

- Osborne MFM. 1951 Aerodynamics of flapping flight with application to insects. . *Exp Biol* **28**, 221-245.

- Oyama A, Okabe Y, Shimoyama K, Fujii K. 2009 Aerodynamic multi-objective design exploration of a flapping airfoil using a Navier-Stokes solver. *J Aerospace Comput Inf Commun* **6**, 256-270.

- Pines, D. & Bohorquez, F. 2006 Challenges Facing Future Micro-Air-Vehicle Development. *Journal of Aircraft* **43**, No. 2, 290-305.

- Platzer M, Jones K, Young J, Lai J. 2008 Flapping wing aerodynamics: Progress and challenges. *AIAA J* **46**, No. 9, 2136-2149.

- Pick S, Lehmann F-O. Stereoscopic 2009 PIV on multiple color-coded light sheets and its application to axial flow in flapping robotic insect wings. *Exp Fluids* doi 10.1007/s00348-009-0687-5.

- Poelma C, Dickinson WB, Dickinson MH. 2006 Time-resolved reconstruction of the full velocity field around a dynamically-scaled flapping wing. *Exp Fluids* **41**, 213-225.

- Pornsin-Sirirak, T.N., Keenon, M., Lee, S.W., Tai, Y.C., Grasmeyer, J., Nassef, H. & Ho, C.M. 2000 MEMS Wing Technology for a Battery-Powered Ornithopter. *13th IEEE International Conference on Micro Electro Mechanical Systems*, 799-804.

- Queipo, N., Haftka, R.T., Shyy, W., Goel, T. Vaidyanathan, R. & Tucker, P.K. 2005 Surrogate-Based Analysis and Optimization. *Progress in Aerospace Sciences* **41**, 1-25.

- Radespiel R, Windte J, Scholz U. 2007 Numerical and experimental flow analysis of moving airfoils with laminar separation bubbles. *AIAA J* **45**, No. 6, 1346-1356.

- Ramasamy M, Leishmann JG. 2006 Phase-locked particle image velocimetry measurements of a flapping wing. *J Aircraft* **43**, No. 6, 1867-1875.

- Read DA, Hover FS, Triantafyllou MS. 2003 Forces on oscillating foils for propulsion and maneuvering. *J Fluid Struct* **17**, 163-183.

- Ringuette MJ, Milano M, Gharib M. 2007 Role of the tip vortex in the force generation of low-aspect-ratio normal flat plates. *J Fluid Mech* **581**, 453-468.

- Riskin DK, Willis DJ, Iriarte-Diaz J, Hedrick TL, Kostandov M, Chen J, Laidlaw DH, Breuer KS, Swartz SM. 2008 Quantifying the complexity of bat wing kinematics. *J Theor Biol* **254**, 604-615.

- Ristroph L, Berman GJ, Bergou AJ, Wang ZJ, Cohen I. 2009 Automated hull reconstruction motion tracking (HRWT) applied to sideways maneuvers of free-flying insects. *J Exp Biol* **212**, 1324-1335.

- Rival D, Prangemeier T, Tropea C. 2009 The influence of airfoil kinematics on the formation of leading-edge vortices in bio-inspired flight. *Exp Fluids* **46**, 823-833.

- Rozhdestvensky, K.V. & Ryzhov, V.A. 2003 Aerohydrodynamics of Flapping-Wing Propulsors. *Progress in Aerospace Sciences* **39**, 585-633.

- Sacks, J., Schiller, S.B. & Welch, W.J. 2008 Design for Computer Experiments. *Technometrics* **31**, No. 1, 41-47.

- Sane SP. 2003 The aerodynamics of insect flight. *J Exp Biol.*

- Sane SP, Dickinson MH. 2002 The aerodynamic effects of wing rotation and a revised quasi-steady model of flapping flight. *J Exp Biol* **205**, 1087-1096.

- Sane SP, Dickinson MH. 2001 The control of flight force by a flapping wing lift and drag production. *J Exp Biol* **204**, 2607-2626.

- Schouveiler L, Hover FS, Triantafyllou MS. 2005 Performance of flapping foil propulsion. *J Fluid Struct* **20**, 949-959.

- Shadden SC, Lekien F, and Marsden JE. 2005 Definition and properties of Lagrangian coherent structures from finite-time Lyapunov exponents in two-dimensional aperiodic flows. *Physica D* **212**, 271-304.

- Shkarayev S, Silin D, Abate G, Albertani R. Aerodynamics of cambered membrane flapping wing AIAA-Paper 2010-58.

- Shyy W., Aono H., Chimakurthi S.K., Trizila P., Kang C.-K., Cesnik C.E.S., & Liu H. 2010 Recent Progress in Flapping Wing Aerodynamics and Aeroelasticity. *Progress in Aerospace Sciences*.

- Shyy W, Trizila P, Kang C, Aono H. 2009 Can tip vortices enhance lift of a flapping wing? *AIAA J* **47**, No. 2, 289-293.

- Shyy, W., Lian, Y., Tang, J., Viieru, D. & Liu, H. 2008 *Aerodynamics of Low Reynolds Number Flyers.* Cambridge University Press.

- Shyy W, Liu H. 2007 Flapping wings and aerodynamics lift. The role of leading-edge vortices. *AIAA J* **45**, No. 12, 2817-2819.

- Shyy W, Udaykumar HS, Rao MM, Smith RW. 2006 *Computational fluid dynamics with moving boundaries*. New York. Dover Publications, Inc.

- Shyy, W., Papila, N., Vaidyanathan, R. & Tucker, P.K. 2001 Global Design Optimization for Aerodynamics and Rocket Propulsion Components. *Progress in Aerospace Sciences* **37**, 59-118.

- Shyy, W., Berg, M. & Ljungqvist, D. 1999 Flapping and Flexible Wings for Biological and Micro Air Vehicles. *Progress in Aerospace Sciences* **35**, 455-505.

- Shyy W. 1994 *Computational modeling for fluid flow and interface transport*. Amsterdam. Elsevier Science Publisher.

- Shyy, W. 1985 A Study of Finite Difference Approximations to Steady-State, Convection-Dominated Flow Problems. *Journal of Computational Physics* **57**, No. 3, 415-438.

- Smola, A.J. & Scholkopf, B. 2004 A Tutorial on Support Vector Regression. *Statistics and Computing* **14**, 199-222.

- Song D, Wang H, Zen L, Yin C. 2001 Measuring the camber deformation of a dragonfly wing using projected comb fringe. *Rev Sci Instrum* **72**, No. 5, 2450-2454.

- Spedding, G.R. & Lissaman, P.B.S. 1998 Technical Aspects of Microscale Flight Systems. *Journal of Avian Biology* **29**, No. 4, 458-468.

- Srygley RB, Thomas ALR. 2002 Unconventional lift-generating mechanisms in free-flying butterflies. *Nature* **420**, 660-664.

- Sun M, Yu X. 2006 Aerodynamic force generation in hovering flight in a tiny insect. *AIAA J* **44**, No. 7, 1532-1540.

- Sun M, Lan SL. 2004 A computational study of the aerodynamic forces and power requirements of dragonfly hovering. *J Exp Biol* **207**,1887-1901.

- Sun M, Yu X. 2003 Flows around two airfoils performing fling and subsequent translation and translation and subsequent clap. *Acta Mecha Sin*; **19**, No. 2, 103-117.

- Sun M, Tang J. 2002 Unsteady aerodynamic force generation by a model fruit fly wing in flapping motion. *J Exp Biol* **205**, 55-70.

- Sunada S, Takahashi H, Hattori T, Yasuda K, Kawachi K. 2002 Fluid-dynamic characteristics of a bristled wing. *J Exp Biol* **205**, 2737-2744.

- Taira K, Colonius T. 2009 Three-dimensional flows around low-aspect-ratio flat-plate wings at low Reynolds numbers. *J Fluid Mech* **623**, 187-207.

- Tang J, Viieru D, Shyy W. 2008 Effect of Reynolds number and flapping kinematics on hovering aerodynamics. *AIAA J* **46**, No. 4, 967-76.

- Tarascio M, Ramasamy M, Chopra I, Leishman JG. 2005 Flow visualization of MAV scaled insect based flapping wings in hover. *J Aircraft* **42**, No. 2, 355-360.

- Tezduyar TE, Behr M, Mittal S, Liou J. 1992 A new strategy for finite element computations involving moving boundaries and interfaces- The deforming-spatial-domain/space-time procedure II. Computation of free-liquid flows, and flows with drifting cylinders. *Comput Method Appl M* **94**, 353-371.

- Thakur,S.T. & Wright, J. 2005 Loci-STREAM: All-Speed CFD Solver for Arbitrary Polygonal Meshes in the Loci Framework. Streamline Numerics Inc., Gainesville, Florida (unpublished).

- Theodorsen T. 1935 General Theory of Aerodynamic Instability and the Mechanism of Flutter. *NACA Report 496.*

- Thomas ALR, Taylor GK, Srygley RB, Nudds RL, Bomphrey RJ. 2004 Dragonfly flight free-flight and tethered flow visualzations reveal a diverse array of unsteady lift-generating mechanisms, controlled primarily via angle of attack. *J Exp Biol* **207**, 4299-4323.

- Thomas, P.D. & Lombard, K. 1978 The Geometric Conservation Law – A Link between Finite-Difference and Finite-Volume Methods of Flow Computation on Moving Grids. *AIAA Paper* 1978-1208.

- Tian X, Iriate-Diaz J, Middleton K, Galvao R, Israeli E, Roemer A, Sullivan A, Song A, Swartz S, Breuer K. 2006 Direct measurements of the kinematics and dynamics of bat flight. *Bioinsp Biomim* **1**, S10-S18.

- Tobalske BW, Hearn JWD, Warrick DR. 2009 Aerodynamics of intermittent bounds in flying birds. *Exp Fluids* **46**, 963-973.

- Usherwood JR, Ellington CP. 2002 The aerodynamics of revolving wings I. Model hawkmoth wings. *J Exp Biol* **205**, 1547-1564.

- Trizila P, Kang C, Aono H.,Visbal MR, & Shyy W. 2010 Fluid Physics and Surrogate Modeling of Low Re Flapping Rigid Flat Plate. AIAA Paper 2008-5081.

- Trizila P, Kang C, Visbal MR, & Shyy W. 2008a A Surrogate Model Approach in 2D versus 3D Flapping Wing Aerodynamic Analysis. AIAA Paper 2008-5914.

- Trizila P, Kang C, Visbal MR & Shyy W. 2008b Unsteady Fluid Physics and Surrogate Modeling of Low Reynolds Number, Flapping Airfoils. AIAA Paper 2008-3821.

- Usherwood JR, Ellington CP. 2002 The aerodynamics of revolving wings II. Propeller force coefficients from mayfly to quail. *J Exp Biol* **205**, 1565-1576.

- van den Berg C, Ellington CP. 1997a The three-dimensional leading-edge vortex of a 'hovering' model hawkmoth. . *Phil. Trans R Soc Lond B* **352,** 329-340.

- van den Berg C, Ellington CP. 1997b The vortex wake of a 'hovering' model hawkmoth. *Phil. Trans R Soc Lond B* **352,** 317-328.

- Vanella M, Fitzgerald T, Preidikman S, Balaras E, Balachandran B. 2009 Influence of flexibility on the aerodynamic performance of a hovering wing. *J Exp Biol* **212**, 95-105.

- Vargas A, Mittal R, Don H. 2008 A computational study of the aerodynamic performance of a dragonfly wing section in gliding flight. *Bioinsp Biomim* **3**, (026004) 1-13.

- Viana, F.A.C., Haftka, R.T., Valder, S., Butkewitsch, S. & Leal, M. 2008 Ensemble of Surrogates: a Framework based on Minimization of the Mean Integrated Square Error. *AIAA Paper* 2008-1885.

- Videler JJ, Stamhuis EJ, Povel GDE. 2004 Leading-edge vortex lifts swifts. *Science* **306**, 1960-1962.

- Visbal MR, Gordiner RE, Galbraith MC. 2009 High-fidelity simulations of moving and flexible airfoils at low Reynolds numbers. *Exp Fluids* **46**, 903-922.

- Visbal, M.R. & Gaitonde, D.V. 1999 High-Order-Accurate Methods for Complex Unsteady Subsonic Flows. *AIAA Journal* **37**, No. 10, 1231-1239.

- Visbal, M.R. & Gaitonde, D.V. 2002 On the Use of Higher-Order Finite-Difference schemes on Curvilinear and Deforming Meshes. *Journal of Computational Physics* **181**, No. 1, 155-185.

- von Ellenrieder KD, Pothos S. 2008 PIV measurements of the asymmetric wake of a two dimensional heaving hydrofoil. *Exp Fluids* **44**, 733-745.

- von Ellenrieder KD, Parker K, Soria J. 2003 Flow structures behind a heaving and pitching finite-span wing. *J Fluid Mech* **490**, 129-138.

- Wakeling JM, Ellington CP. 1997 Dragonfly flight II. Velocities, accelerations and kinematics of flapping flight. *J Exp Biol* **200**, 557-582.

- Walker SM, Thomas ALR, Taylor GK. 2009 Deformable wing kinematics in free-flying hoverflies. *J R Soc Interface* doi 10. 1098/rsif.2009.0120

- Walker SM, Thomas ALR, Taylor GK. 2008 Deformable wing kinematics in the desert locust how and why do camber, twist and topography vary through the stroke? *J R Soc Interface* **6**, No. 38, 735-747.

- Wallance ID, Lawson NJ, Harvey AR, Jones JDC, Moore AJ. 2006 High-speed photogrammetry system for measuing the kinematics of insect wings. *Appl Opt* **45**,No. 7, 4165-4173.

- Wang H, Zeng L, Liu H, Yin C. 2003 Measuring wing kinematics, flight trajectory and body attitude during forward flight and turning maneuvers in dragonflies. *J Exp Biol* **206**, 745-757.

- Wang JK, Sun M. 2005 A computational study of the aerodynamic and forewing-hindwing interaction of a model dragonfly in forward flight. *J Exp Biol* **208**, 3785-3804.

- Wang ZJ, Russell D. 2007 Effect of forewing and hindwing interactions on aerodynamic forces and power in hovering dragonfly flight. *Phys Rev Lett* **99**,14801.1-14801.4.

- Wang ZJ. 2005 Dissecting Insect Flight, *Annual Review of Fluid Mechanics* **37**, 183-210.

- Wang ZJ. 2004 The role of drag in insect hovering. *J Exp Biol* **207**, 4147-4155.

- Wang ZJ, Birch MB, Dickinson MH. 2004 Unsteady forces and flows in low Reynolds number hovering flight two-dimensional computations vs robotic wing experiments. *J Exp Biol* **207**, 461-474.

- Wang ZJ. 2000a Two dimensional mechanism for insect hovering. *Phys Rev Lett* **85**, No. 10, 2216-2219

- Wang ZJ. 2000b Vortex shedding and frequency selection in flapping flight. *J Fluid Mech* **410**, 323-341.

- Warkentin J, DeLaurier J. 2007 Experimental aerodynamic study of tandem flapping membrane wings. *J Aircraft* **44**, No. 5, 1653-1661

- Warrick DR, Tobalske BW, Powers DR. 2009 Lift production in the hovering hummingbird. *Proc R Soc Lond B* **276**, No. 1674, 3747-3752.

- Warrick DR, Tobalske BW, Powers DR. 2005 Aerodynamics of the hovering hummingbird. *Nature* **435**, 1094-1097.

- Weis-Fogh, T. 1973 Quick Estimates of Flight Fitness in Hovering Animals, Including Novel Mechanisms for Lift Production. *Journal of Experimental Biology* **59**, 169-230.

- Weis-Fogh, T. 1972 Energentics of Flight in Hummingbirds and in Drosophila. *Journal of Experimental Biology* **56**, 79-104.

- Willmott AP, Ellington CP. 1997a The mechanics of flight in the hawkmoth Manduca sexta I. Kinematics of hovering and forward flight. *J Exp Biol* **200**, 2705-2722.

- Willmott AP, Ellington CP. 1997b The mechanics of flight in the hawkmoth Manduca sexta II. Aerodynamic consequences of kinematic and morphological variation. *J Exp Biol* **200**, 2723-2745.

- Willmott AP, Ellington CP, Thomas ALR. 1997 Flow visualization and unsteady aerodymamics in the flight of the hawkmoth, Manduca sexta. *Phil Trans R Soc Lond B* **352**, 303-316.

- Wilson MW, Peng J, Dabiri JO, and Eldredge JD. 2009 Lagrangian coherent structures in low Reynolds number swimming. *J Phys Condens Matter* **21**.

- Wu G, Zeng L. 2009 Measuring the kinematics of a free-flying hawkmoth (Macroglossum stellatarum) by a comb-fringe projected method. *Acta Mech Sin* doi 10.1007/s10409-009-0306-y.

- Yamamoto M, Isogai K. 2005 Measurement of unsteady fluid dynamic forces for a mechanical dragonfly model. *AIAA J* **43**, No. 12, 2475-2480.

- Yates GT. 1985 Optimum pitching axes in flapping wing propulsion. *J Theor Biol* **120**, 255-276.

- Young J, Lai JCS, 2008 Germain C. Simulation and parameter variation of flapping-wing motion based on dragonfly hovering. *AIAA J* **46**, No. 4, 918-924.

- Young J, Walker SM, Bomphrey RJ, Taylor GK, Thomas ALR. 2009 Details of insect wing design and deformation enhance aerodynamic function and flight efficiency. *Science* **325**, 1549-1552.

- Zeng L, Hao Q, Kawachi K. 2001 Measuring the body vector of a free flight bumblebee by the reflection beam method. *Meas Sci Technol* **12**, 1886-1890.

- Zeng L, Hao Q, Kawachi K. 2000 A scanning projected line method for measuring a beating bumblebee wing. *Opt Commun* **183**, 37-43.

- Zeng L, Matsumoto H, Kawachi K. 1996 A fringe shadow method for measuring flapping angle and torsional angle of a dragonfly wing. *Meas Sci Techno*l **7**, 776-781.

- Zhang J, Lu X-Y. 2009 Aerodynamic performance due to forewing and hindwing interaction in gliding dragonfly flight. *Phys Rev E* **80**, 017302.1-017302.4.

- Zhang G, Sun J, Chen D, Wang Y. 2008 Flapping motion measurement of honeybee bilateral wings using four virtual structured-light sensors. *Sens Actuators A* **148**, 19-27.

- Zheng L, Wang X, Khan A, Vallance RR, Mittal R. 2009 A combined experimental-numerical study of the role of wing flexibility in insect flight. 47th AIAA Aerospace Sciences Meeting Including The New Horizons Forum and Aerospace Exposition AIAA 2009-382.